HIGH ACCURACY THERMAL CHARACTERIZATION AND PROCESS IMPROVEMENT FOR 3D-PRINTED CONTINUOUS PITCH CARBON FIBERS

MOUAZ ALI

A THESIS SUBMITTED TO

THE FACULTY OF GRADUATE STUDIES

IN PARTIAL FULFILLMENT OF THE REQUIREMENTS

FOR THE DEGREE OF

MASTER OF APPLIED SCIENCE

GRADUATE PROGRAM IN MECHANICAL ENGINEERING

YORK UNIVERSITY

TORONTO, ONTARIO

APRIL 2026

Abstract

This thesis investigates the development of high-thermal conductivity polymer composites through the process improvement of Continuous Pitch-based Carbon Fiber (CPCF) 3D printing. While previous research has identified CPCF as a viable solution for enhancing the thermal performance of 3D-printed parts, significant discrepancies exist between experimental results and theoretical predictions using the parallel model for composites. This research identifies and addresses the factors contributing to these discrepancies. First, a new fiber characterization methodology was established, comparing traditional microscopy with pycnometry to accurately determine the cross-sectional area and volume fraction of K13D2U fiber tows within the composites. Second, a high-accuracy thermal conductivity measurement apparatus was designed, calibrated, and validated. Furthermore, process improvements were implemented in the coating and printing processes to mitigate fiber breakage and maintain tow integrity. The implementation of these optimized processes resulted in the fabrication of a full-scale 3D-printed composite sample. Measurements conducted using a newly developed macro thermal conductivity apparatus demonstrated a significant improvement in thermal performance compared to prior studies, achieving a thermal conductivity of 36.63 W/mK at a volume fraction of 6.42%. While some deviations from the ideal parallel model remain due to inherent discontinuities within the fiber tow, this study contributes a validated framework for the precise fabrication and characterization of high-performance CPCF composites, offering a path forward for thermal management applications in additive manufacturing.

Acknowledgements

This research was conducted under the supervision of Dr. Roger Kempers in the TF-Lab. I would like to sincerely thank Dr. Kempers for the opportunity to pursue this work, for fostering an exceptional research environment, and for his guidance and support throughout the course of this study.

I am also grateful to the former members of the TF-Lab, Dr. Ahmed Elkholy, Omar Khaled, and my close friend Sinan Olcun, for their technical support and guidance. Additionally, I would like to thank our current TF-Lab member Mohamed Hasan for his support and valued friendship.

I also extend my gratitude to Dr. Garrett Melenka and Dr. Thomas Cooper for their invaluable insight and academic guidance.

Lastly, I want to thank my family and friends for providing the motivation and emotional support that sustained me through the more challenging periods of this journey.

Table of Contents

List of Tables

List of Figures

Chapter 1 Introduction

1.1 Research Motivation

Thermal management remains a critical challenge despite advancements in heat exchangers, particularly as power densities continue to rise [1], [2]. Traditionally, copper and aluminum alloys have been the primary materials for machined heat exchangers due to their exceptional thermal conductivity. However, limitations inherent to machining processes hinder the creation of complex geometries, restricting design freedom. This limitation in achievable geometric complexity with machining has driven research towards additively manufactured (AM) metal heat exchangers, offering the ability to create intricate designs for optimized heat exchangers [3], [4], [5], [6]. Yet the high density of metals remains a concern for lightweight applications. Consequently, research is exploring composites, which offers the potential for both excellent thermal conductivity and reduced weight due to polymer densities [7], [8]. The ability to fabricate composites using AM could unlock both design freedom and enhanced performance.

Continuous Pitch-based Carbon Fibers (CPCF) are considered a frontrunner among materials for fabricating thermally conductive composites [9]. However, integrating CPCF into Additive Manufacturing (AM) processes remains a challenge due to their brittle nature. While a few commercially available printers offer continuous composite printing capability, most aren't designed for CPCF printing and have excessive costs and complexity. The limited accessibility to CPCF 3D printing restricts research and development of optimized heat exchanger designs for superior thermal performance and lightweight properties. Fused Filament Fabrication (FFF) printers, known for their affordability and widespread availability, present a potential solution. The open-source nature of FFF printers facilitates modifications enabling the printing of CPCF and thermoplastics.

Ibrahim et al. [9] fabricated a composite using a "handlay-up" technique. This involved sandwiching K13D2U CPCF layers between 3D-printed, rectangular PLA coupons and bonding them together with epoxy resin. K13D2U is a specific grade of CPCF produced by Mitsubishi Chemicals, tailored for high-thermal conductivity applications, with an advertised thermal conductivity of 800 W/mK [10]. The CPCF is composed of thousands of micrometer-sized fibers bunched together to create a CPCF tow. Ibrahim's initial work fabricated a composite that resulted in a measured effective thermal conductivity of 23.6 W/mK at 4.3 vol%, which was about 32% lower than the predicted value. Carrying forward from Ibrahim's findings, Olcun et al. modified a Prusa i3 MK2 to print with the K13D2U CPCF tows [11]. The CPCF tows were coated with PLA to add rigidity and were printed at a 45° angle from the bed to minimize fiber breakage. The highest effective thermal conductivity achieved was 37.1 W/mK at a fiber volume fraction of 9.5%, representing a significant milestone in CPCF printing. However, this value falls notably short of the predicted thermal conductivity by approximately 51%. Both Ibrahim and Olcun attributed the lower-than-predicted thermal conductivity primarily to fiber breakage. Olcun conducted investigations using single-tow thermal conductivity measurements, microscopy, micro-CT scanning, and thermal imaging. The investigations identified nozzle angle and internal friction as primary contributors of fiber breakage during extrusion. To address this, Olcun utilized a 6-axis robot arm to experiment with various printing angles and implemented a custom nozzle design to minimize fiber-to-nozzle interactions.

Though the investigations yielded some valuable insight into the process of CPCF printing, there are various concerns regarding the accuracy and reliability of the apparatus Olcun developed for measuring single fiber tow thermal conductivity. Accurate prediction of composite thermal conductivity using the parallel model relies on precise thermal conductivity values for both matrix and reinforcing materials. Olcun used manufacturer-specified fiber dimensions for thermal conductivity calculations, despite manufacturer's claim of potential inaccuracies in these values [10]. Additionally, while the coating process appeared to preserve fiber integrity based on thermal conductivity measurements, inconsistencies between measured and predicted values, along with discrepancies between coated and uncoated fiber thermal conductivities, suggest potential measurement errors or unanticipated factors influencing the results. To enhance reliability, multiple measurements of the same CPCF grade are recommended, along with a re-evaluation or redesign of the thermal conductivity apparatus.

Olcun identified printing speed and raster spacing as potential factors influencing fiber tow integrity. To investigate these parameters, fiber tows were printed at varying speeds and spacings. Proper e-step calibration is crucial for maintaining consistent filament extrusion in standard FFF processes, preventing over- or under-extrusion, especially at higher print speeds. This is particularly critical for coated fiber tows, where inconsistent extrusion can lead to fiber buckling, stretching, or breakage. While Olcun's research focused on print speed and raster spacing, the influence of extrusion parameters on fiber integrity warrants further investigation. Once all printing parameters are considered and optimized, fiber volume fraction must be carefully controlled to ensure there are no discrepancies between the printed fiber rasters within the composite compared to the intended amount. This allows for a more accurate comparison between the measured thermal conductivity of the CPCF composite and the estimated value using the parallel model. Additionally, composites might require careful post-processing to guarantee a consistent and uniform surface contact with the apparatus to achieve accurate thermal conductivity measurements.

While several issues have been highlighted from Olcun's experiments, there may be additional factors to consider for CPCF composite printing, requiring a thorough investigation. Despite the shortcomings, Olcun's results indicate CPCF as a viable and effective solution for enhancing composite thermal conductivity compared to most other discontinuous methods. Given that both Ibrahim's and Olcun's research utilized K13D2U fiber tow and produced promising results, it may currently be the most viable CPCF option. Once these issues and shortcomings are addressed, the findings can be used to develop a robust process capable of fabricating high-thermal conductivity CPCF composites.

1.2 Research Objectives

Based on the research conducted by Olcun using K13D2U tows, it was evident that the thermal conductivity of the printed composites did not align with the predictions of the parallel model. The primary hypothesis for this discrepancy was fiber breakage during the printing process, with the fiber pre-impregnation process showing no signs of breakage. Despite this, uncertainties remain regarding the accuracy of quantifying fiber breakage and other potential contributing factors. As such, the objectives of the current investigation are to:

1. Accurately characterize fiber geometry to establish a precise CPCF cross-sectional area and fiber volume fraction.
2. Develop a high-accuracy thermal conductivity measurement apparatus for CPCF.
3. Develop methods for mitigating fiber breakage during both the coating and printing processes.
4. Implement and demonstrate these process improvements by fabricating a full-scale 3D-printed composite sample and measuring its thermal conductivity to validate enhanced performance.

1.3 Thesis Outline

This thesis is structured into seven chapters, systematically detailing the research. Chapters 2 to 6 address the objectives of this research outlined in Section 1.2. Chapter 2 provides an extensive literature review on the thermal applications of polymer composites, examining both traditional and additive manufacturing methods for composite fabrication, as well as the inherent advantages and challenges of these processes. The chapter concludes with a summary of all the findings within the chapter along with the challenges faced in a previous research conduct by Olcun.

Chapter 3 begins by analyzing the type of CPCF best suited for achieving high thermal conductivity composites. The importance of accurate geometrical characterization is then discussed as a key prerequisite for obtaining reliable fiber thermal conductivity measurements. The chapter explores various methods for geometrical characterization of fibers to precisely determine their cross-sectional area. Due to the scale and bundled nature of the fibers, several challenges were encountered. Ultimately, three different methods were discussed and compared, with their respective results presented. The chapter concludes with a summary of all the findings.

Chapter 4 focusses on fiber thermal conductivity methodologies, addressing the major challenges in developing an accurate apparatus for measuring fiber thermal conductivity. An extensive literature review was first conducted on various existing methods, noting the gaps found in previous research, particularly that conducted by Olcun. The culmination of these findings were used to develop a new apparatus for accurate fiber thermal conductivity measurement. This section includes the design principle, FEM simulations, and a detailed description of the instrumentation utilized. Apparatus refinements, such as temperature sensor calibration, heat loss calibration, and radiative heat loss, were also investigated. The chapter concludes with an uncertainty analysis, demonstrating the accuracy of the apparatus, along with a results and discussion section where the apparatus was validated using materials with known thermal conductivities.

Chapter 5 assesses the fiber coating process developed by Olcun and detailed the results found. The chapter then went further into the design and development of a new coating process. The key dimensions and CAD models were shown in detail along with the process involved for coating the K13D2U fibers using PLA. The newly coated K13D2U fibers were then tested for thermal conductivity and the results along with comparison to Olcun's coated K13D2U fibers were discussed. Next, the 3D printing process from Olcun's setup was analyzed, taking all his findings into account for developing an improved extruder design for 3D printing with the newly coated K13D2U fibers. The design, challenges faced and shortcomings of the new extruder design were all discussed in the Extruder Design section. Lastly, the newly designed extruder was tested by printing K13D2U rasters and testing their thermal conductivity. Rasters from Olcun's 3D printing setup were also tested to compare their thermal conductivities. The results from this test were presented and discussed.

Chapter 6 takes all previous improvements implemented to the 3D printing process for K13D2U and addresses the final research objective by 3D printing a full-size K13D2U composite and measuring its thermal conductivity. The composite was printed with varying fiber volume fractions using the parallel model estimation for thermal conductivity. A thermal conductivity apparatus was developed for high accuracy thermal conductivity measurement of the composite. The design principle and instrumentation are detailed within the chapter. The K13D2U composite was carefully designed and manually fabricated with three different volume fractions to be tested against the parallel model. The measured thermal conductivity of the K13D2U composites and comparison to the parallel model are presented and discussed.

The thesis then ends with Chapter 7, which includes a summary and conclusion. Important research points, results and discussion from each chapter, analysis and challenges faced are all briefly addressed here. The chapter than concludes with an outlook on what can be expected to be the next steps for future research on the topic.

Chapter 2 Literature Review

Composites are made up of at least two or more materials that are combined to enhance a specific material property. They are classified based on the type of matrix and reinforcing material used. The material with the weaker properties being enhanced is typically said to be the matrix while the material/s used to enhance a matrix material property is called the reinforcing material. Common matrices used in composites are polymers, ceramic and metals [12], while fibers, particulates and even structured composites are used as the reinforcement [13]. Polymer composites offer superior performance compared to pure polymers due to their reinforced structure, incorporating materials like fibers and/or particles. This reinforcement enhances mechanical strength, durability, and specific material properties, making polymer composites an excellent choice for applications requiring advanced structural integrity and performance characteristics.

2.1 Thermal Applications of Polymer Composites

Pure polymers often lack sufficient thermal conductivity, limiting their use in scenarios requiring high heat transfer (insulation being a prime example) [14], [15]. This is where incorporating thermally conductive reinforcements into polymer composites becomes advantageous. These reinforcements facilitate higher heat transfer, making the resulting composites viable for thermal applications [7]. The increased thermal conductivity is especially beneficial in industries like electronics, automotive, and aerospace, where efficient heat exchange is critical for optimal performance and preventing overheating [16], [17]. Traditional heat exchangers often rely on metals due to their superior thermal and mechanical properties. However, metals are also among the densest materials, leading to weight limitations as heat exchanger sizes increase in various applications [18], [19]. Polymer composites offer a promising alternative. They can achieve a desired level of thermal enhancement through a variety of polymer and reinforcing material combinations [20]. The specific matrix and reinforcement can be chosen based on an application's needs, considering factors like mechanical strength, temperature resistance, and weight. Additionally, the volume fraction of the reinforcing material can be adjusted to achieve the optimal balance between weight and thermal conductivity.

2.2 Thermally Conductive Polymer Composites

Composites are engineered materials made up of a matrix and a reinforcing material. Depending on the reinforcement's geometry and arrangement within the composite, they are classified as either continuous or discontinuous/particulate [21]. To achieve exceptional thermal conductivity, a key strategy is incorporating reinforcements boasting significantly higher thermal conductivity than the matrix itself. Decades of research have focused on optimizing this matrix-reinforcement pairing, alongside developing fabrication techniques for composites with unparalleled thermal management capabilities. Both continuous and discontinuous composites have been explored in this pursuit.

2.2.1 Discontinuous Composites

Discontinuous composites are a class of reinforced materials where the reinforcing element exists as discrete particles or short fibers within a matrix. The effectiveness of these composites for thermal conductivity heavily relies on the characteristics of these discontinuous reinforcements, including their shape, size, and alignment (for fibers). Researchers have utilized various high thermal conductivity particulates like copper, aluminum, silver, diamond powder, graphite, carbon fibers, and aluminum nitride [22], [23], [24], [25]. However, achieving optimal thermal conductivity goes beyond material selection; uniform dispersion of these particulates within the matrix is equally crucial. Uneven dispersion can create gaps that disrupt the heat transfer pathway, ultimately hindering the composite's overall thermal conductivity. Additionally, more complex materials like carbon nanotubes (CNTs) and boron nitride nanotubes (BNNTs) have also been used due to their extremely highly thermal conductivities [26], [27].

The shape and size of the reinforcement significantly influence the heat transfer pathway within the composite. Spherical particles offer the least efficient path due to minimal contact area with the surrounding matrix. In contrast, elongated particles (rods) and plate-like structures can provide a more direct route for heat to travel, especially when aligned in the direction of heat flow. Larger particles can be difficult to disperse uniformly within the matrix, while extremely small particles might suffer from interfacial thermal resistance, hindering their effectiveness. For high-conductivity fibers like carbon fibers, CNTs, and BNNTs, alignment becomes a critical factor. Heat transfer in solids occurs through vibrations of atoms, called phonons. In misaligned fibers, phonons scatter more frequently as they travel through the composite, disrupting the heat flow and hindering thermal conductivity [28], [29]. By aligning the fibers, researchers can create a more direct pathway for phonons, reducing scattering and enhancing overall thermal conductivity. Achieving this alignment can be challenging, but various techniques are being explored, such as using external magnetic fields during fabrication or incorporating pre-aligned structures into the composite matrix [30].

2.2.2 Continuous Composites

While discontinuous composites offer a versatile approach to achieving thermal conductivity, continuous composites provide several advantages. These advantages stem from the uninterrupted network structure of the reinforcing element within the matrix. This network creates a more efficient pathway for heat transfer, leading to superior thermal conductivity compared to discontinuous composites. However, the uninterrupted network in continuous composites comes with a trade-off. This structure leads to a property known as anisotropy.

Anisotropy refers to the dependence of a material's properties on the direction of measurement. In continuous composites, the aligned reinforcement network can lead to superior thermal conductivity in the direction of alignment, but significantly lower conductivity in other directions. This can be a limitation in applications where heat needs to be dissipated in multiple directions. For example, a heat sink made from a continuous composite might be highly effective at channeling heat away from a source in one direction, but less effective at radiating heat outwards from its sides. However, the anisotropic nature of continuous composites can also be advantageous in certain situations. By strategically controlling the alignment of the reinforcement network, engineers can design materials that restrict heat flow to a single direction. This can be beneficial in applications such as thermal insulation, where the goal is to minimize heat transfer in all directions except for a specific one.

Carbon fibers, particularly those derived from petroleum pitch (PCF), are the preferred choice for reinforcement in continuous composites due to their inherently high thermal conductivity, exceeding 1000 W/mK [31]. This exceptional property stems from two key factors: the high aspect ratio (length-to-diameter ratio) of the fibers and their aligned structure. These features facilitate a more efficient pathway for heat to travel through the composite compared to randomly oriented or discontinuous fibers. Additionally, the strong covalent bonds within the carbon fiber structure further enhance its heat conduction capability. Polyacrylonitrile (PAN) carbon fibers are also employed for reinforcement, but their thermal conductivity is several orders of magnitude lower than that of PCF [32], [33]. PAN fibers offer advantages in terms of flexibility and cost due to the readily available synthetic precursor, polyacrylonitrile, and a less complex manufacturing process. However, PAN fibers exhibit a significantly higher tensile strength and toughness compared to PCF, while PCF possesses a higher modulus of elasticity, thermal conductivity, and electrical conductivity.

While carbon fibers (CF) reign supreme in continuous composite reinforcement due to their exceptional thermal conductivity, other options exist. Glass, aramid, basalt fibers, and metal wires offer alternative reinforcement strategies, each prioritizing specific properties such as high strength, thermal insulation, or impact resistance [34], [35], [36], [37]. Among these, copper wires present a unique proposition for thermal applications. Their affordability, ductility, and respectable thermal conductivity (around 400 W/mK) make them an attractive choice [29]. However, careful consideration of trade-offs is crucial. Copper's high density significantly increases the overall weight of the composite, posing a significant challenge in weight-sensitive applications like aerospace engineering. Additionally, achieving comparable thermal performance with copper necessitates a larger quantity of material compared to CF, ultimately leading to heavier composites. While CF necessitate intricate manufacturing techniques due to their inherent brittleness, their superior thermal conductivity enables the design of lightweight composites.

2.3 Additive Manufacturing

Conventional manufacturing techniques often limit the design of intricate heat transfer pathways that could optimize heat exchanger performance. Additive manufacturing (AM), also known as 3D printing, disrupts this paradigm by offering a revolutionary approach to fabricating composite heat exchangers. AM enables the creation of complex structures with precise control over design and material properties. This capability paves the way for a new generation of heat exchangers: lighter, more efficient, and potentially more cost-effective for mass production due to AM's inherent design flexibility and potential for material customization.

AM offers several techniques suitable for processing polymers, including Selective Laser Sintering (SLS), Digital Light Processing (DLP), and Fused Filament Fabrication (FFF) [38]. FFF is one of the most commercially used techniques for polymers due to its relative affordability and ease of use. In FFF, filament is extruded and melted by a heated nozzle before being deposited layer-by-layer onto a build platform. This allows for the creation of complex geometries with a high degree of design freedom. Commonly used FFF polymers include Acrylonitrile Butadiene Styrene (ABS), Polylactic acid (PLA), polyethylene terephthalate glycol (PETG), and nylon [39]. Each material offers unique properties relevant to thermal applications:

- ABS: Offers good strength and slight flexibility, making it suitable for some thermally demanding applications. However, its higher printing temperature (220°-240°C) and warping tendency can be drawbacks. Additionally, emits potentially harmful fumes when heated.

- PLA: An economical and eco-friendly choice, PLA offers lower printing temperatures (180°-220°C) compared to ABS. However, its limitations lie in brittleness and lower heat resistance, making it unsuitable for high-temperature thermal applications.

- PETG: PETG offers a balance between ABS and PLA. It exhibits improved mechanical strength and heat resistance compared to PLA, with typical printing temperatures ranging from 220°C to 250°C. Additionally, it boasts better warping resistance than ABS. However, it may not be ideal for very high-temperature applications.

- Nylon: Nylon stands out for its superior chemical resistance and the potential for FDA approval, making it attractive for specific thermal management applications requiring these properties. Printing temperatures for nylon can be higher, typically ranging from 240°C to 290°C. However, considerations include its higher cost and potential challenges during printing, necessitating careful optimization of printing parameters.

In addition to single-polymer FFF, additive manufacturing (AM) offers significant potential for fabricating polymer composites, which can be specifically tailored for thermal applications. AM techniques provide unique advantages for composite fabrication through multi-extruder setups. Unlike traditional methods, AM can enable controlled incorporation of thermally conductive reinforcements directly within the polymer matrix or during the printing process. This would allows for the creation of intricate heat exchanger designs with optimized heat transfer pathways, achieving specific thermal and mechanical properties through the selection of suitable polymer and reinforcement materials [40].

While ABS, PLA, and nylon are commonly used FFF materials, their limitations at elevated temperatures necessitate the exploration of alternatives. Polyetheretherketone (PEEK) stands out with a remarkable glass transition temperature of 143 °C [41], making it suitable for applications that would melt conventional FFF materials. However, the use of non-standard materials often introduces challenges. New printing parameters, such as extrusion temperature, bed temperature, and printing speed, require careful optimization to ensure successful printing, maintain dimensional accuracy, and achieve the desired properties. It is important to note that current FFF technology is primarily limited to thermoplastics.

2.3.1 Fused Filament Fabrication of Continuous Fiber Composites

The field of 3D printing with continuous fibers remains in its preliminary stages, reflected in the limited availability of compatible fiber FFF printers. Currently, Markforged stands out as a leading company in fiber printing, offering 3D printers capable of continuous fiber composite printing [42]. The Onyx Pro printer is restricted to fiberglass reinforcement, while the Mark Two boasts a wider range of compatible fibers, including carbon fiber, Kevlar, fiberglass, and HSHT fiberglass. However, the current limitation is that both printers are only compatible with continuous fibers supplied by Markforged, which are designed for high strength and have poor thermal conductivity. *Continuous Composites* offer a distinct approach with their CF3D printer, departing from conventional filament-based systems [43]. The CF3D printer employs an in-situ impregnation process, where dry continuous fibers are impregnated with a thermosetting resin during deposition by the print head (robot arm) along the designated extrusion path. This approach facilitates customization for user-specific applications. However, the CF3D printer is primarily targeted for industrial environments due to its complex system and higher cost, limiting commercial availability for broader use.

Despite the impressive capabilities of currently available continuous fiber 3D printers, their material limitations, excessive cost, and industrial-focused design hinder research applications, particularly rapid prototyping of heat exchangers. To accelerate the development of optimized composite heat exchanger designs, an accessible and cost-effective continuous fiber printing solution is essential. In response to this need, Olcun modified a commercially available, open-source Prusa i3 MK2 printer to print with CPCFs. A pre-coating process was developed to enhance fiber rigidity, involving PLA coating applied to CPCFs before extrusion through a dual-nozzle system. While this approach achieved a composite thermal conductivity of 37.1 W/mK at 9.5 vol%, it fell significantly short of the predicted value, highlighting the challenge of fiber breakage during the printing process. While Olcun's approach using a modified Prusa i3 MK2 printer represents a promising step forward, several limitations and challenges must be addressed to fully realize the potential of 3D printed continuous fiber composites.

2.4 Challenges in Continuous Fiber 3D Printing

In his research, Olcun used the parallel model to predict the effective thermal conductivity of the composite for a given fiber volume fraction, assuming perfectly aligned, continuous fibers with known geometric properties:

$$k_{eff} = v_f k_f + (1 - v_f) k_p \quad \textit{Equation 2-1}$$

where k_{eff} is the effective thermal conductivity of the composite, v_f is the fiber volume fraction, k_f is the fiber thermal conductivity and k_p is the polymer thermal conductivity. Under idealized conditions, the parallel model accurately predicts composite thermal conductivity, enabling precise control over its thermal design. However, Olcun's experimentally measured thermal conductivity values for the 3D-printed composites were 50-65% lower than those predicted using the parallel model. This significant discrepancy led Olcun to attribute the reduced thermal conductivity largely due to fiber breakage during the fiber coating and printing processes.

To investigate fiber breakage within the 3D printed composites, Olcun employed a multi-faceted approach involving microscopy, micro-CT scanning, and thermal imaging. Micro-CT analysis revealed fiber breakage predominantly on the top layer, likely caused by nozzle drag. While confirming fiber breakage, micro-CT scanning could not quantify the extent of the breakage. To address this, Olcun developed an apparatus to measure the thermal conductivity of both virgin and coated fibers. By comparing the two measurements, the impact of the coating process on fiber integrity could be quantified through the decrease in thermal conductivity. However, a detailed analysis of the apparatus in Section 4.1 highlights various limitations in its accuracy and reliability for measuring thermal conductivity at the fiber scale. Accurate characterization of fiber geometry, including cross-sectional area and shape, is also crucial for precise thermal conductivity measurements using various techniques. Olcun's approach fell short in both these aspects, necessitating the development of a more accurate and reliable measurement apparatus and a thorough characterization of fiber geometry to advance the understanding of CPCF composites. A detailed investigation into fiber geometry characterization is presented in Chapter 3 .

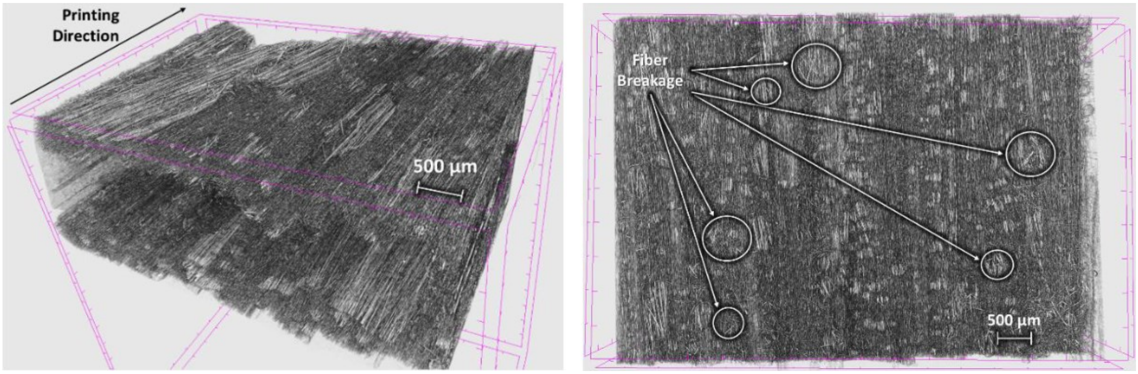

Figure 2-1: Olcun's MicroCT images of 3D printed K13D2U composite at a 9.5% volume fraction [11]

Olcun 3D-printed several fiber rasters at varying print speeds, subsequently removing the polymer matrix to enable microscopic analysis. A clear correlation between increased print speed and fiber breakage was observed through microscopic examination of the outer fiber layers. However, this analysis provides limited insight into the overall fiber damage within the composite. Infrared thermal imaging revealed a significant temperature drop (approximately 40°C) between the nozzle and deposition, with increased fiber breakage noted at approximately 60 mm along the 100 mm raster, suggesting a correlation between transient thermal effects and fiber damage. Olcun proposed that printing longer rasters could further elucidate the impact of extended printing on fiber quality.

Olcun observed overcrowding of fibers during full-size composite printing, prompting an investigation into the effects of raster spacing on fiber breakage. It was hypothesized that increasing raster spacing would mitigate fiber overcrowding and reduce breakage. To test this hypothesis, composites with varying fiber volume fractions were fabricated at both 1 mm and 1.5 mm raster spacings. A 10% decrease in fiber breakage was observed at the wider 1.5 mm spacing, as determined through thermal conductivity measurements. A critical factor to consider in these composite measurements is the introduction of holes for Resistance Temperature Detector (RTD) probe insertion during subsequent thermal conductivity testing. These holes create discontinuities within the fiber structure, potentially compromising the accuracy of the measured thermal conductivity when compared to the predicted value using the parallel model. Determining the extent to which these discontinuities affect the results is essential for reliable data interpretation. Olcun concluded that while printing parameters influence print quality, fiber breakage primarily originates from nozzle friction and angle. Modifying printer nozzle angle was deemed too challenging, thus this remains unexplored. Olcun's proposed use of a scanning electron microscope to visualize fiber breakage on printed PCF rasters was deemed insufficient for quantifying total fiber breakage. Thermal conductivity measurement remains the most viable method for assessing the impact of fiber damage on composite performance.

Table 2-1: List of various composite matrices and reinforcing materials and their measured thermal conductivity

Matrix Material	Reinforcing Material	Type of Composite	Loading	Thermal Conductivity (W/mK)	Reference
ABS	Carbon fiber	Discontinuous	1.7 vol%	0.22	[23]
ABS	Silver	Discontinuous	1.4 vol%	0.24	
ABS	Graphite	Discontinuous	4.3 vol%	0.37	
Polypropylene (PP)	Copper	Discontinuous	43 vol%	2.3	[24]
Polyphenylene sulphide (PPS)	BN	Discontinuous	60 wt%	5.2	[44]
Thermoplastic polyurethane (TPU)	Graphene	Discontinuous	45 wt%	12.25	[45]
Epoxy	Graphene / Copper	Discontinuous	40 wt% / 35 wt%	13.5	
Bismaleimide	CNT	Discontinuous	35 wt%	70	[26]
Cellulose nanofibers	Ag-BNNT	Discontinuous	25 wt%	20.89	[27]
ABS	Graphite	Discontinuous	21.7 wt%	17.6	[46]
PLA	Copper	Continuous	2.7 vol%	9.4	[47]
PLA/Epoxy	PCF	Continuous	4.3 vol%	23.6	[9]

PLA	PCF	Continuous	9.5 vol%	37.1	[11]

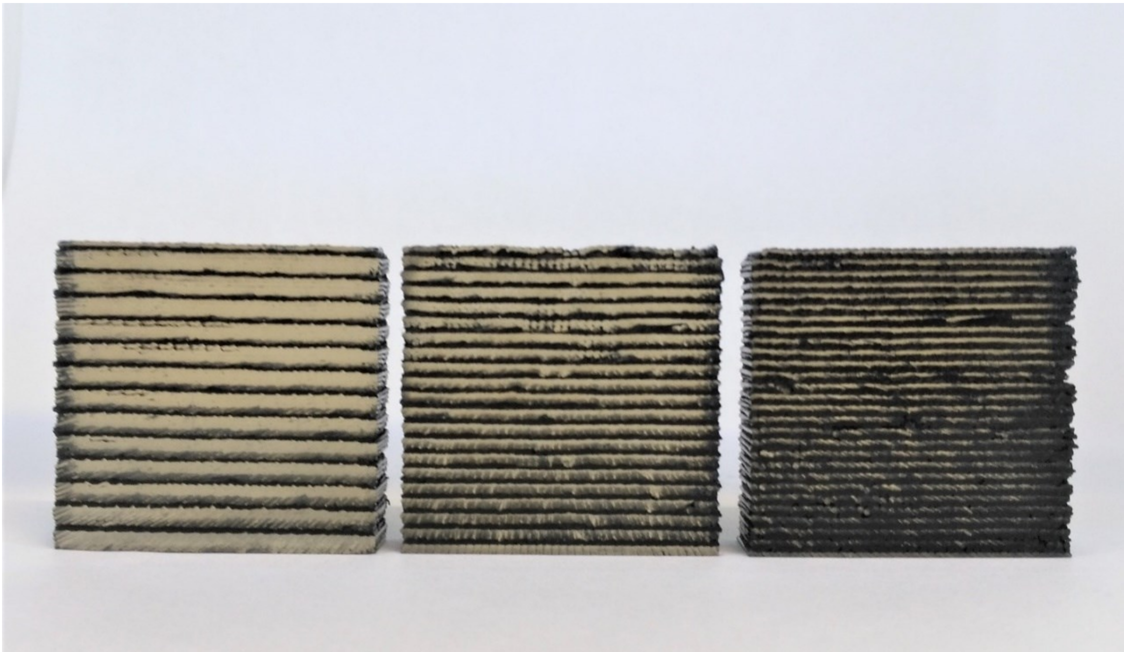

Figure 2-2: 3D-printed continuous pitch carbon fiber composite by Olcun [48]

2.5 Summary

Composites are highly versatile materials, offering enhanced mechanical, thermal, and electrical properties. In thermal management applications, where metals may be limited due to their inherent properties, composites can be tailored to achieve high thermal conductivity while maintaining desirable chemical and mechanical characteristics. While CF have traditionally been used to improve mechanical strength, relatively few studies have focused on their role in enhancing thermal conductivity. However, recent advancements have shown that incorporating PCF into polymer composites can significantly increase thermal conductivity. This improvement, however, is contingent on maintaining continuous PCF strands within the polymer matrix to form an interconnected network, ensuring an efficient pathway for heat transfer. However, CPCF is costly to manufacture and inherently brittle, making it difficult to fabricate complex structures.

AM offers a potential solution by enabling the use of open-source 3D printers modified to process CPCF composites with readily available thermoplastic matrices. Olcun's research made significant progress in this area, demonstrating that CPCF composites printed using a modified Prusa i3 exhibited considerably higher thermal conductivity per volume fraction than most existing composites. However, the measured values remained far below theoretical predictions based on the parallel thermal conductivity model, likely due to fiber breakage during printing. Olcun's apparatus provided initial insights into this issue, but the accuracy of his measurements remains uncertain due to estimations made regarding fiber geometry and the assumption that radiative effects are negligible. Given this uncertainty, several key research questions remain: (1) How can fiber breakage during the printing process be more accurately quantified, and what are the key factors influencing it? (2) How can thermal characterization methods be improved to reduce uncertainties related to fiber geometry and composite microstructure? (3) What modifications to the 3D printing process can minimize fiber breakage while maintaining printability and mechanical integrity? (4) Does the presence of polymer coating on CPCF affect its thermal conductivity, both as a standalone material and within a composite? (5) Is the significant disparity between theoretical thermal conductivity predictions and experimentally measured values in CPCF composites caused by additional, unaccounted-for factors? These questions also align with the broader research objectives: accurately characterizing fiber geometry, developing improved thermal characterization techniques, mitigating fiber breakage in the coating and printing processes, and implementing process improvements for a full-scale 3D-printed CPCF composite. The next chapter focuses on fiber analysis, laying the foundation for improved characterization methods and a more precise understanding of fiber geometry and its role in composite performance.

Chapter 3 Fiber Analysis

Since Olcun's research [11] relied on the manufacturer's listed fiber count and diameter without independent verification, the precision of his resultant thermal conductivity calculations remains uncertain. This chapter focuses on addressing this gap to ensure that all subsequent thermal conductivity measurements are both accurate and repeatable. To resolve this fundamental issue, the following sections address the first research objective: the accurate characterization of fiber geometry to establish a precise CPCF cross-sectional area and fiber volume fraction. By evaluating and comparing traditional microscopy with pycnometry, a robust characterization framework is established, providing the foundational data required for the thermal models presented in later chapters.

3.1 Continuous Pitch-Based Carbon Fiber Selection

Olcun procured several grades of CPCFs from Mitsubishi Chemicals, prioritizing high thermal conductivity and commercial availability. Among the offered fiber types, K13D2U stood out for its exceptional thermal conductivity, as shown in Table 3-1. Notably, K13D2U also boasts superior mechanical properties, including tensile modulus, strength, yield strength, and electrical resistivity, making it the best candidate for fabricating composites. Equation 6-3 shows that there is a proportional relationship between the effective thermal conductivity of the composite and the thermal conductivity of the fibers. Therefore, when fabricating composites with high thermal conductivity, selecting a CPCF with exceptionally high thermal conductivity would be the logical choice. Despite an extensive search, no other supplier was identified offering continuous carbon fibers with comparable thermal conductivity. Nippon Graphite Fiber Corporation [49] offers carbon fibers with higher thermal conductivity, but only in chopped or milled formats.

It's important to acknowledge that the specifications provided by Mitsubishi are estimations, intended for material selection. To ensure optimal performance and predictable characteristics in the final printed composites, conducting independent characterization of key parameters like cross-sectional area and thermal conductivity is crucial. Characterization of thermal conductivity will require precise measurement of the CPCF tow's cross-sectional area, as detailed in Chapter 4 . This will provide more reliable data when tailoring the composite's properties to specific application requirements.

Table 3-1: Mitsubishi Chemicals pitch carbon fibers and their properties [10]

Fiber type	Filament count	Tensile modulus (GPa)	Tensile strength (GPa)	Yield (mg/m)	Density (g/cm^3)	Thermal conductivity (W/mK)	Electrical Resistivity (μΩm)
K1352U	2,000	620	3.60	270	2.12	140	6.6
K1392U	2,000	760	3.70	270	2.15	210	5.0
K13C2U	2,000	900	3.80	275	2.20	620	1.9
K13D2U	2,000	935	3.70	365	2.20	800	1.5

3.2 Geometrical Characterization

Accurate thermal conductivity determination relies heavily on precise sample geometry, including cross-sectional area and length. Equation 4-7 illustrates the direct correlation between these parameters and the calculated thermal conductivity value. Discrepancies in cross-sectional area or length can significantly impact uncertainties. Due to the microscopic scale of individual fibers within a CPCF tow, direct measurement of cross-sectional area using traditional metrology techniques is challenging. Consequently, indirect methods such as optical microscopy, scanning electron microscopy (SEM), or pycnometry must be employed to estimate fiber diameter and count, enabling calculation of the overall tow cross-sectional area.

3.2.1 Optical Microscopy and Scanning Electron Microscopy Method

To determine the cross-sectional area of a CPCF tow, precise measurements of average fiber diameter and fiber count are essential. Given potential discrepancies between actual and manufacturer-specified fiber counts due to quality control and handling variations, direct measurement of these parameters is crucial. The following equation can be used to calculate the cross-sectional area of the CPCF tow:

$$A = N_{fibers}\,\pi\,{r_{fiber}}^2 \qquad \textit{Equation 3-1}$$

where N_{fibers} is the number of fibers in the CPCF tow and r_{fiber} is the average fiber radius.

Acquiring clear images of the CPCF cross-section is crucial when characterizing its geometry. With sharp and higher resolution images, the measurement uncertainty will be lower and accuracy higher. Due to manufacturing and shipping processes, the CPCF rolls come wound around a cardboard tube, with the CPCF tow being flat as seen in Figure 3-1. The fibers are loosely held together and are extremely brittle, causing them to fray and/or break without proper care. To determine the cross-sectional area of the CPCF tow, the fiber bundle was positioned such that its axis was aligned parallel to the microscope's optical axis, enabling precise measurement. A small section of CPCF tow was carefully excised using a sharp blade and mounted for SEM analysis, ensuring optimal alignment of the tow with the electron detector. The resulting images (Figure 3-2) reveal a variation in fiber orientation within the tow. While the SEM's tilting functionality aided in aligning fiber groups, accurately measuring the entire cross-section proved challenging due to fiber misalignment. Consequently, an alternative approach was adopted: measuring a representative sample of fiber diameters to estimate the average diameter and subsequently calculate an approximate cross-sectional area. However, a large variability in fiber diameter will impact the uncertainty of the calculated cross-sectional area.

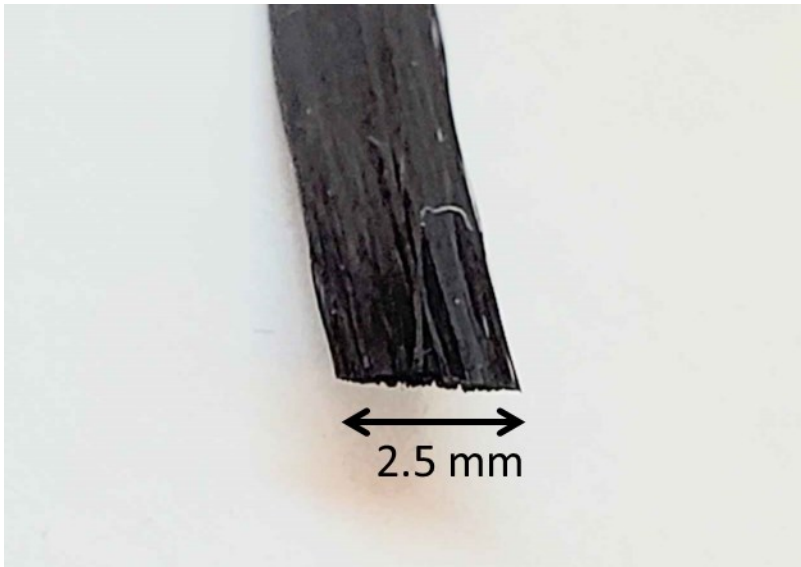

Figure 3-1: K13D2U fiber tow from Mitsubishi Chemicals

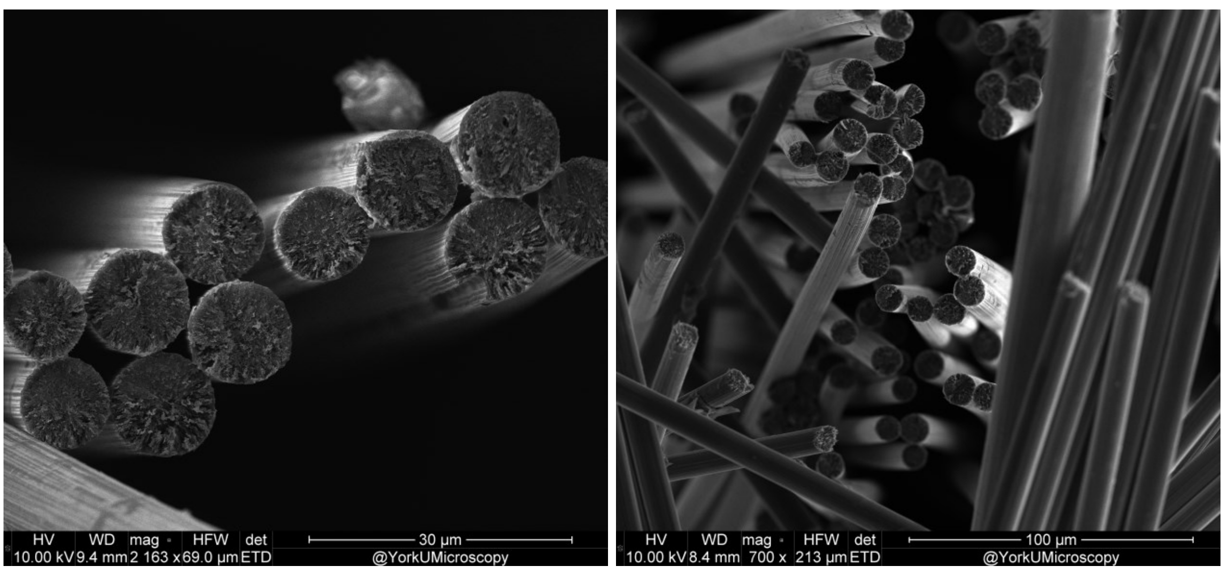

Figure 3-2: SEM images of K13D2U fibers

To accurately count the number of fibers within a CPCF tow, a method was developed to immobilize and visualize the fibers. Initially, curing fibers in epoxy resin proved ineffective due to fiber dispersion as seen in Figure 3-3. To counter this, a 44-gauge copper wire was used to bundle the fibers in the tow and maintain their alignment within a 3D-printed jig filled with epoxy resin as seen in Figure 3-4. After curing and surface preparation, optical microscopy was used to capture images of the CPCF tow cross-section for subsequent analysis using ImageJ software. Five measurements were taken from two separate rolls of K13D2U CPCF. While this limited sample size was due to the time-consuming nature of the image processing, the data revealed significant variance in fiber count, both within and between rolls.

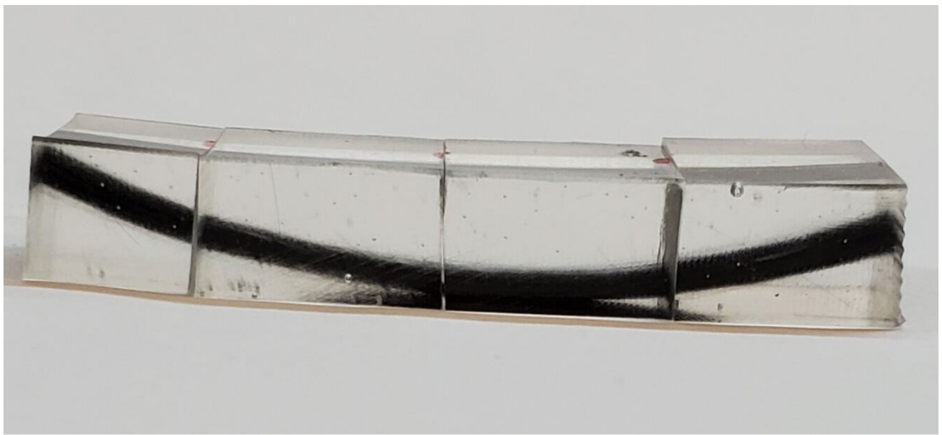

Figure 3-3: K13D2U tow embedded in epoxy resin

Figure 3-4: Copper-wire-coiled K13D2U tows embedded with epoxy resin in a 3D-printed jig

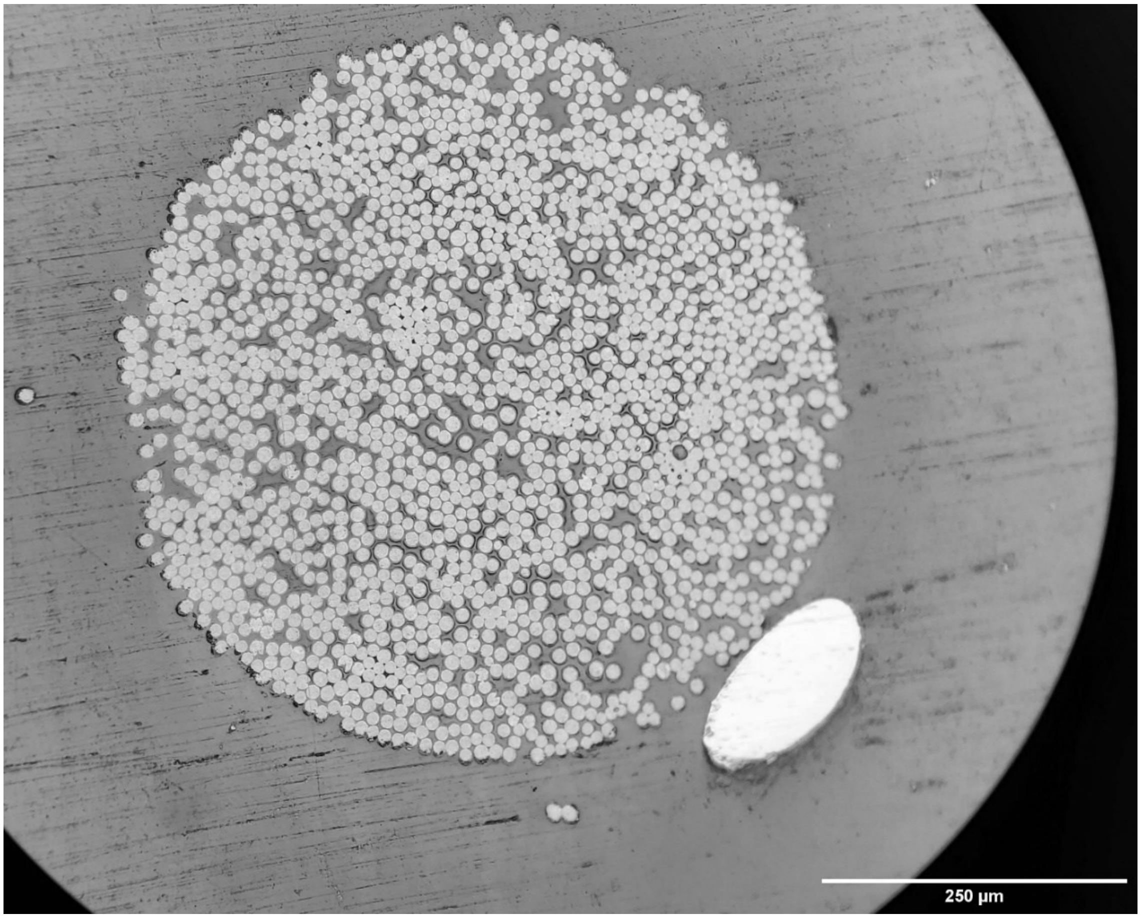

Figure 3-5: Optical microscope image of coiled K13D2U tow

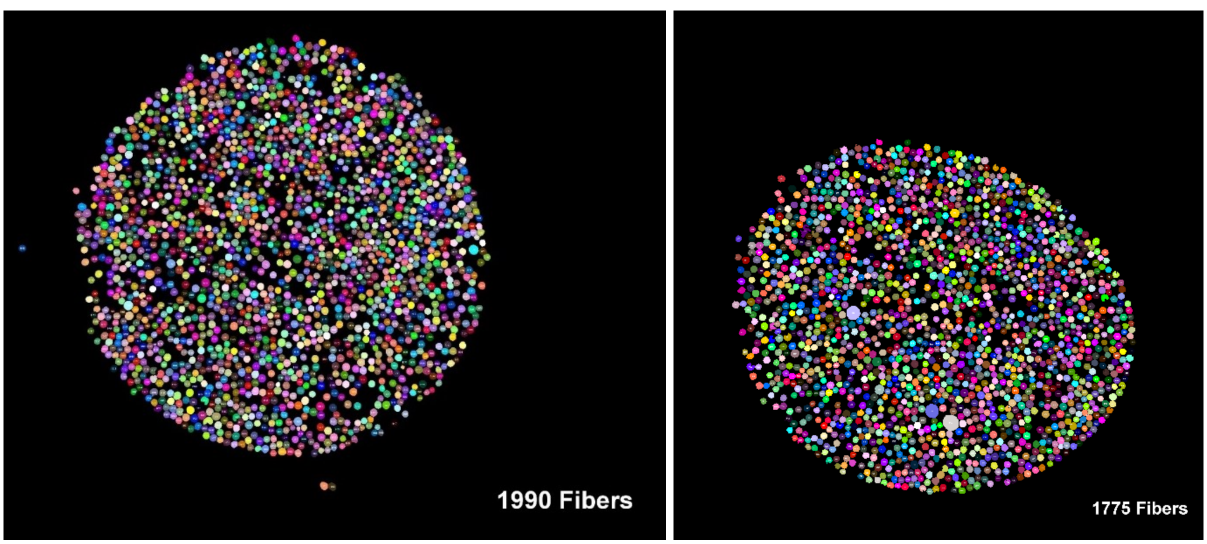

Figure 3-6: ImageJ analysis on the optical microscope image of K13D2U CPCF tow cross-section from two separate rolls

Table 3-2: ImageJ analysis on the average fiber diameter and fiber count for K13D2U tow

Sample population	142 fibers	
Minimum fiber diameter	9.032 μm	
Maximum fiber diameter	14.872 μm	
Mean fiber diameter	10.581 μm	
Standard deviation	0.9 μm	
	K13D2U Roll 1	K13D2U Roll 2
Fiber count	1990	1775
Tow cross-sectional area	1.74983E-7 m^2	1.56078E-7 m^2

Table 3-2 shows there is a 10.8% discrepancy in cross-sectional area between the two K13D2U rolls, emphasizing the need for accurate measurements of both fiber diameter and count. While average fiber diameter was calculated for one roll and applied to both, this approach proved time-consuming and prone to inaccuracies due to variations in fiber count between rolls. To obtain more reliable cross-sectional area estimates, future studies should prioritize accurate measurement of both fiber diameter and count for each individual tow.

3.2.2 Pycnometer Method

Pycnometry is a precise technique for determining the volume, and subsequently, the density of solid materials. It involves utilizing a specialized instrument, a pycnometer, which houses a sample chamber of known volume. By introducing a known gas, and measuring the pressure change, the volume of the sample can be calculated. This, in conjunction with the sample's mass, allows for accurate density determination. Pycnometry is particularly valuable for materials with complex geometries or porous structures, as it can precisely measure their true volume, excluding any internal voids. In the case of CPCFs, pycnometry proves to be effective given the micro scale of the fibers. With the density known, a measured length of

CPCF can be excised and weighed to calculate its cross-sectional area using the following equation:

$$\rho = \frac{m}{V} = \frac{m}{LA} \quad \text{Equation 3-2}$$

where ρ is the density, m is the mass, V is the volume, L is the length and A is the cross-sectional area.

To determine the density of K13D2U, a sample was submitted to Micromeritics for pycnometry analysis. The CPCF tow was chopped into fine pieces to maximize sample volume within the pycnometer chamber. The results sent by Micromeritics are shown in Table 3-3. The measured density was found to be lower than what was specified by Mitsubishi Chemicals, though the difference is only 1.5%. To ensure repeatability in cross-sectional area calculation using density, several lengths of CPCF were excised and weighed as shown in

Table 3-4. The calculated cross-sectional area for all four lengths of CPCF tows were almost the same, showing high repeatability.

Table 3-3: K13D2U density measurements from Micromeritics

Parameter	**Value**	**Standard Deviation**
Volume	0.1360 cm^3	0.0001 cm^3
Density	2.1682 g/cm^3	0.001 g/cm^3

Table 3-4: K13D2U cross-sectional area calculation

Length (cm)	40	30	20	10
Mass (g)	0.1542	0.1161	0.0774	0.0387
Cross-sectional Area (m^2)	1.7780E-07	1.78489E-07	1.78489E-07	1.78489E-07
Uncertainty	0.27 %	0.34 %	0.48 %	0.93 %

Table 3-5: Manufacturer Specifications for K13D2U

Density (g/cm^3)	2.2
Fiber diameter (μm)	11
Number of fibers	2000
Calculated tow cross-sectional area (m^2)	1.90066E-7

Table 3-6: Pycnometry method uncertainties

Parameter	**Uncertainty**
Length	5.00E-04 m
Mass	3.00E-04 g
Density	3000 g/m^3

The cross-sectional area of the K13D2U tow, calculated based on manufacturer-specified dimensions, was found to be 6.5% higher than the value determined through pycnometry. This indicates good agreement between the two methods, with the additional advantage that the pycnometry approach provides quantifiable uncertainties. The density of K13D2U is assumed to remain consistent across rolls, as it consists of over 99% carbon. Therefore, the density measurement from a single roll of K13D2U is used as a reference for subsequent calculations.

3.3 Summary

Three methods were compared for accurate cross-sectional area measurement of K13D2U tows. SEM proved effective for measuring fiber filament diameter but struggled to accurately count filaments within a tow due to image quality limitations. Optical microscopy, while requiring less post-processing, still necessitated extensive effort for filament counting. A combined approach, utilizing both SEM and optical microscopy, enabled the measurement of average filament diameter and filament count. However, this method remained time-consuming and required a large sample population to assess measurement uncertainty. In contrast, pycnometry, a technique for determining density, offered a more accurate, repeatable, and time-efficient method for calculating CPCF tow cross-sectional area. By measuring the density of a known length of K13D2U tow, the cross-sectional area could be calculated with greater precision. This approach eliminated the need for direct filament counting and provided a more reliable estimate of the fiber tow's geometry. One thing to note however, is that SEM imaging revealed a thin layer of coating on individual fibers. The manufacturer has no specific information on the sizing of this coating except that it is a polymer. This could affect thermal conductivity measurements since polymers have a very low thermal conductivity, leadings to added contact resistance.

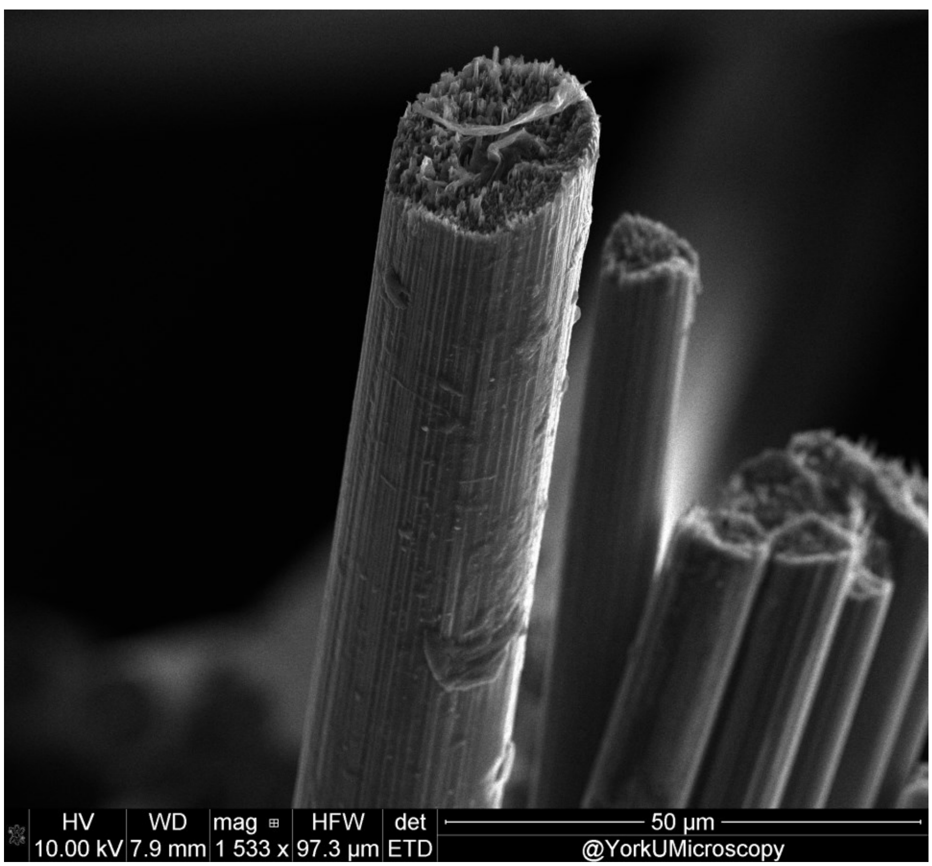

Figure 3-7: Side view of a single K13D2U fiber showing sizing in SEM

Pycnometry enabled accurate geometrical characterization of K13D2U, surpassing the methods employed by Olcun. Previous research, including Olcun's, relied on manufacturer-specified fiber count and diameter, which were found to be inaccurate. While Olcun's study referenced Naito et al.'s research for filament diameter uncertainty (0.5 μm), the accuracy of this value was questionable, as Naito et al. may have limited their measurements to a small sample of filaments [50]. SEM analysis in the present study revealed significant variation in filament diameters within the K13D2U tow, emphasizing the need for comprehensive diameter measurements to accurately characterize the material. Compared to the methods based on individual fiber measurements, pycnometry offers a more reliable and accurate approach for determining the overall geometry and density of CPCF tows.

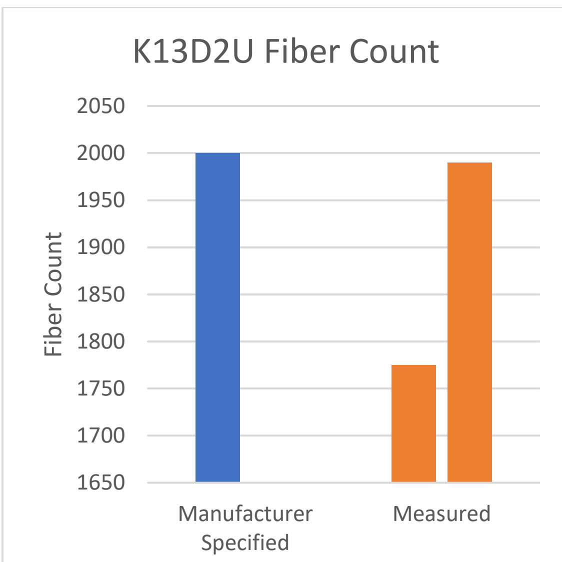

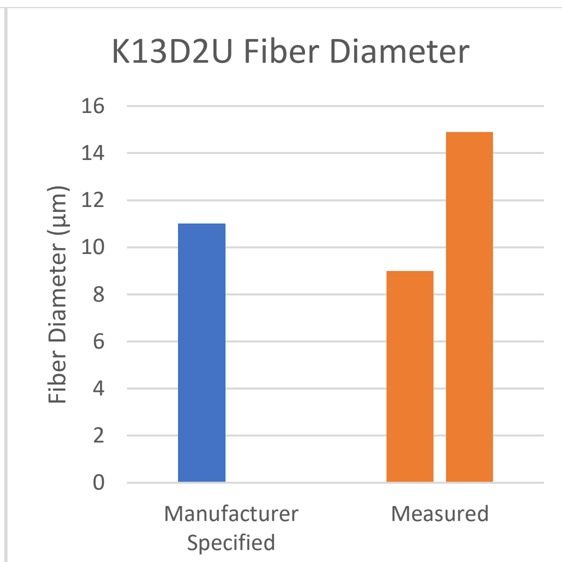

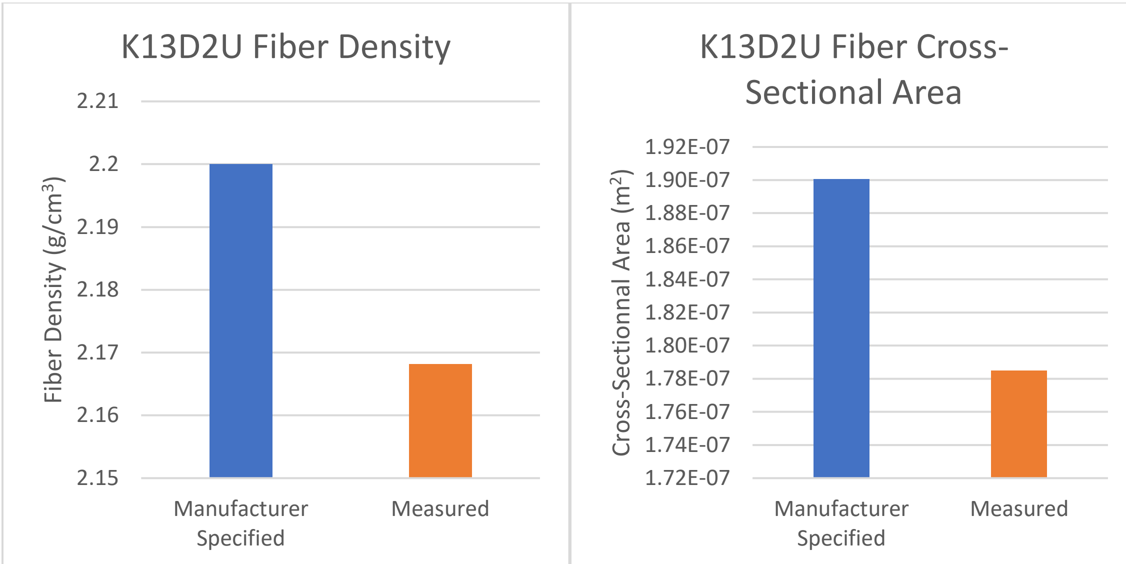

Figure 3-8: Bar graph comparing measured and manufacturer specified data for K13D2U

Chapter 4 Pitch Carbon Fiber Tow Thermal Characterization

This chapter addresses the second research objective: the development of a high-accuracy thermal conductivity measurement apparatus specifically for CPCF. A thorough literature review was conducted to evaluate existing methodologies and identify the requirements for an apparatus capable of accurately measuring CPCF tow thermal conductivity. The following sections detail the design and development process, including the specific calibration procedures and heat loss compensations required to ensure high measurement precision. The chapter concludes with a series of validation tests using known materials, followed by the measured thermal conductivity results for the K13D2U CPCF tow.

4.1 Literature Review

Advancements in CPCF 3D printing is dependent upon accurate thermal conductivity characterization. Olcun's research highlighted the brittleness of K13D2U filaments as a primary challenge, leading to breakage during both coating and 3D printing processes. As discussed in Section 2.4, Olcun's investigation into CPCF filament breakage highlighted the effectiveness of thermal conductivity measurements for assessing CPCF tow integrity. To advance CPCF 3D printing, developing an apparatus capable of measuring uncoated CPCF tow thermal conductivity is crucial, establishing a baseline for comparison with coated CPCF tows and full-size composites, facilitating systematic improvements in the coating process and composite design.

4.1.1 Previous Research

The thermal characterization apparatus developed by Olcun [11], underwent rigorous testing to assess its fidelity. The apparatus takes inspiration from one developed by Piraux et al. for measuring the thermal conductivity of a bundle of fibers. However, key aspects of the apparatus such as guard heating of the sample heater and temperature sensor wires were neglected. The apparatus operates on the principles of steady-state Fourier's law for conduction. In this setup, one end of the sample is heated with a known power input, while the opposite end is maintained at a constant temperature. This arrangement creates a one-dimensional, steady-state temperature gradient across the sample. Figure 4-2 presents the thermal network diagram developed by Olcun, which visually represents the heat flow through the apparatus and the sample. Temperature measurements are taken using thermistors placed at two points along the sample, separated by a distance L. In the diagram, Q_{input} represents the heat applied to the sample, while a chiller maintains the opposite end at temperature T_c. After analyzing the thermal network diagram, several unknown contact resistances are observed at the interfaces between the sample, heater, and other components. These resistances arise due to surface roughness at contact points, creating microscopic gaps that hinder heat transfer.

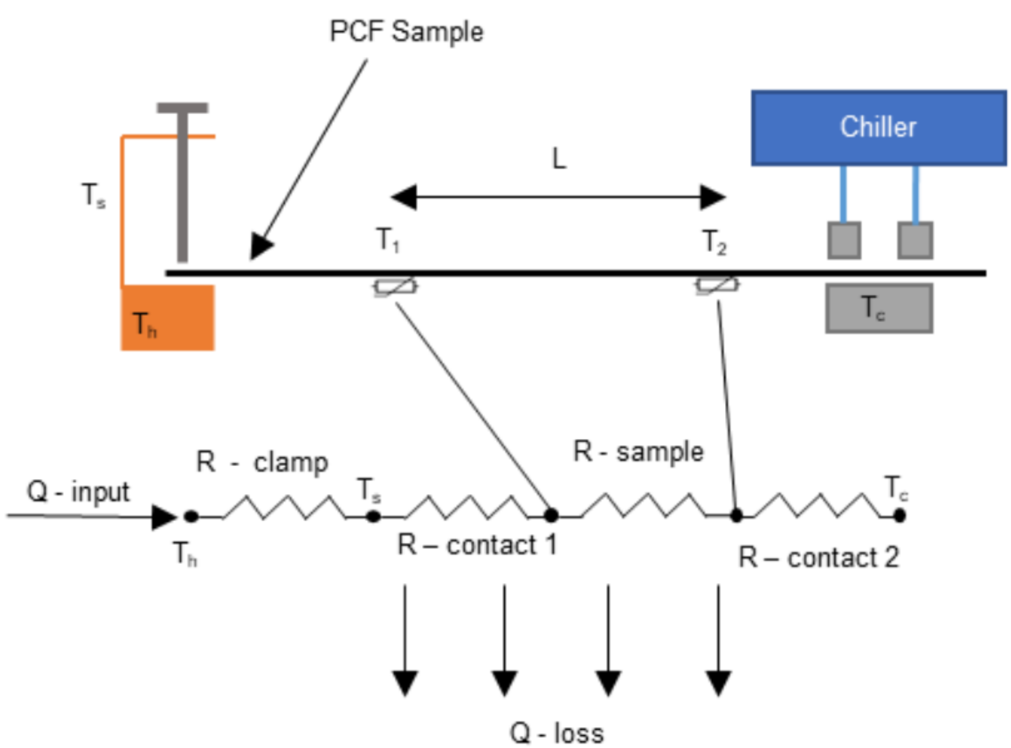

Figure 4-1: Apparatus thermal network diagram by Olcun

In addition, temperature measurements are influenced by external heat gains and losses due to convection and radiation from the surroundings. Convection plays a significant role in heat transfer to or from the sample's surface, where the movement of surrounding air can either dissipate or introduce heat. This can skew temperature readings, especially in atmospheric conditions where air density and flow are significant. To mitigate these unwanted effects, Olcun implemented a bell jar enclosure combined with a vacuum pump, enabling experiments to be conducted in a rough vacuum environment. The reduction of air density limits convection, as fewer air molecules are available to carry heat through movement. There are several levels of vacuum: low (rough) vacuum, medium vacuum, high vacuum, ultra-high vacuum and extremely high vacuum [51], each corresponding to a specific pressure range and the number of gas molecules per cubic meter. As the number of gas molecules decreases, the frequency of collisions between them also diminishes. Since the transfer of energy (in the form of heat) relies on both molecular collisions and convective movement, a vacuum with minimal gas molecules significantly reduces heat transfer by both conduction and convection by air.

With a rough vacuum established, Olcun conducted a heat loss calibration to account for the residual convection present within the bell jar. As described by Olcun, this calibration involved suspending the copper clamp in the vacuum, applying power to the thermistor (which acted as a heater), and then measuring both the surface temperature of the copper clamp and the surrounding ambient temperature. The power lost from the heater was calculated based on the temperature difference between the copper clamp's surface and the surrounding ambient temperature, leading to the formulation of Equation 4-1. This equation was then used to estimate the heat entering the sample as a function of the temperature difference between the copper clamp surface and the surrounding environment.

$$Q_{loss} = 0.0006129(T_{surface} - T_{\infty})$$

Equation 4-1

where Q_{loss} is the heat lost from the heater, $T_{surface}$ is the surface temperature of the heater and T_{∞} is the surrounding temperature

Although this calibration was aimed to address convective losses, the effects of radiation on the copper clamp and the thermistors were not accounted for. Given that the enclosure is a bell jar, the high emissivity of glass allows significant radiative heat transfer from the surroundings to the bell jar, and subsequently from the bell jar to components within it, especially in a vacuum environment. In later experiments, it was observed that the thermistor readings were influenced by the heater when positioned within its line of sight. This effect is likely due to the glass bead composition of the thermistor sensor, which makes it sensitive to radiative heat transfer. As a result, the calibration performed by Olcun is likely compromised, as the temperature measurements from the thermistors were likely less than accurate.

Further tests were necessary to validate all other aspects of Olcun's apparatus. However, the apparatus suffered a critical failure when a severe leak caused the enclosure and vacuum pump to be flooded with water from the chiller, resulting in irreversible damage. The leak was traced to a design flaw in the choice of fittings used in the cold block inside the enclosure. Moreover, the fittings selected for routing water tubes into the enclosure were rated for pressure, not vacuum, requiring a long time to reach a reasonable vacuum. Thus, a new and improved apparatus was required for conducting experiments to measure CPCF thermal conductivity.

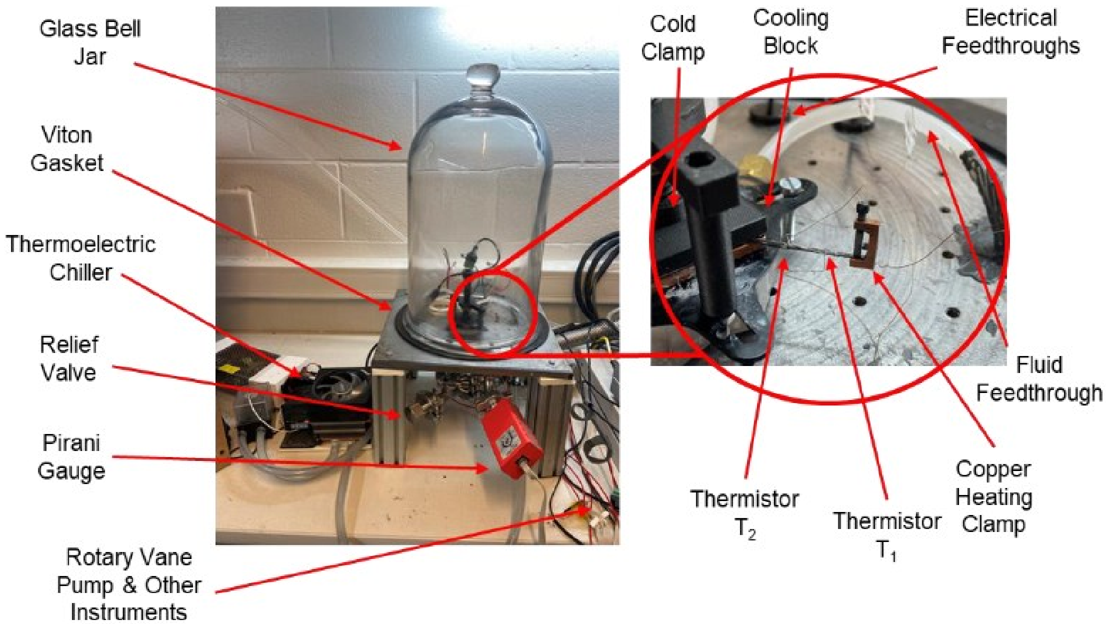

Figure 4-2: Thermal characterization apparatus by Olcun[11]

4.1.2 Thermal Characterization Techniques

For the development of a new apparatus, an extensive literature review was conducted to identify existing designs capable of measuring the thermal conductivity of CPCF tow. The review also explored the potential for modifying Olcun's apparatus or other established designs to meet the specific requirements for CPCF tow thermal conductivity measurement. Thermal conductivity measurement techniques are broadly classified into two categories: steady-state and transient methods, each offering several techniques with distinct advantages and limitations that must be carefully considered when designing an apparatus for accurate CPCF measurements. Steady-state methods involve applying continuous heat to the sample until a stable, equilibrium temperature distribution is reached, after which Fourier's law of heat conduction is typically used to calculate the sample's thermal conductivity. Common steady-state techniques include the guarded hot plate (GHP), heat flow meter (HFM), and comparative methods, often used in combination or with variations to suit specific experimental needs [52],

[53], [54]. Steady-state techniques are often considered the most accurate for directly measuring the thermal conductivity of a wide range of solid materials, including both insulators and conductors. However, achieving a steady state can be time-consuming, resulting in long measurement times. Additionally, these methods typically require relatively large, uniform samples due to the one-dimensional heat flow assumption inherent in the apparatus design. Furthermore, contact resistance at the interfaces between the sample and the measurement apparatus often leads to inaccuracies in the measurements. For CPCF tows, this presents additional challenges, as each tow consists of approximately 2,000 bundled fibers. The small gaps between individual fibers contribute to increased contact resistance, making it difficult to obtain accurate thermal conductivity measurements.

Conversely, transient methods typically measure thermal conductivity indirectly by tracking time-dependent temperature changes in response to a heat pulse or disturbance applied to the sample. The resulting data is then analyzed using complex mathematical models tailored to the specific apparatus. Common transient techniques include the transient hot wire, transient line-source (TLS), transient plane-source (TPS) or hot disk, laser flash analysis (LFA), and 3-omega methods [55], [56], [57]. While TPS and hot wire methods directly calculate thermal conductivity from the observed heat flow, most other techniques primarily measure thermal diffusivity, requiring additional material properties such as density and specific heat capacity to compute thermal conductivity. Transient methods are much faster than steady-state methods since thermal equilibrium is not required. Sample sizes can also be very small along with accommodating solids, liquids, powders and even gasses, being able to measure both isotropic and anisotropic materials. Due to rapid temperature changes, contact resistance is often insignificant. However, given the numerous complex mathematical models involved, transient methods can often be challenging when interpreting the data compared to steady-state methods. The instrumentation involved is generally expensive and complex, especially when additional material properties need to be measured to calculate thermal conductivity.

Both steady-state and transient techniques are well-documented in the literature for measuring the thermal conductivity of metal wires and fibers. Choi et al. developed a non-contact method specifically for measuring the thermal conductivity of PAN carbon fiber [32]. In their method, electrical heat is applied directly to a PAN carbon fiber tow of specified length, and the resulting temperature difference is recorded using thermal imaging. The cross-sectional area of the tow is calculated, and Fourier's law of conduction is applied to determine thermal conductivity, achieving results with approximately 1% deviation. Zhang et al. utilized the steady-state short-hot-wire method to measure the thermal conductivity of a single carbon fiber. Here, the fiber acts as a pin fin attached to a heated wire to enable one-dimensional heat conduction, with the method capable of measuring thermal conductivities up to 1000 W/mK [58]. However, Moon et al. highlighted limitations of the short-hot-wire method, particularly due to thermal contact resistance between the sample and the wire, as well as uncertainties in geometric measurements [59]. To address these challenges, Moon et al. developed the steady-state DC Thermal Bridge Method (DCTBM), capable of measuring both conductive and non-conductive fibers. Conductive fibers act as both heater and thermometer, while non-conductive fibers are coated with a metallic layer to enable measurement. In this setup, a single fiber is suspended between two copper sheet electrodes bonded to an alumina substrate, and a one-dimensional heat conduction model is applied. Convective losses are reduced by conducting tests in a vacuum chamber at 1.3×10^{-6} mbar. The error introduced by the metallic coating was negligible for fibers with thermal conductivities >2 W/mK and remained under 10% for conductivities >0.2 W/mK. Although the versatility of the DCTBM allows it to measure both highly conductive PCF and low conductivity PLA-coated fibers, its design is limited to single-fiber measurement. In an experiment using the 3ω method, Mishra et. Al. also measured longitudinal thermal conductivity of single carbon fibers, and the effect of thermal contact resistance between the fiber and electrodes by plotting a [60]. The fiber thermal resistance was measured at different lengths and a thermal resistance versus length plot was then used to estimate the thermal contact resistance. The results show that thermal contact resistance has a minute influence on the measured thermal conductivity. Other methods such as the Angstrom and laser flash [61], [62] measure thermal diffusivity of fiber bundles and rely on the mathematical relation between material heat capacity, density and thermal conductivity. This approach requires additional resources to determine fiber tow thermal conductivity and introduces uncertainties from the measurements of both thermal diffusivity and heat capacity. Additionally, most apparatuses neglect thermal contact resistance at fiber-fiber and fiber-electrode interfaces, potentially compromising the accuracy of the results. The method developed by Piraux embodies the principles of commonly used guard heating method (ASTM C177) [63]. Similarly, the apparatus designed by Elkholy et al., also based on the guard heating technique, demonstrates high accuracy in measuring the thermal conductivity of solids and composites [64]. While this setup is unsuitable for measuring fiber tow thermal conductivity directly, a specialized apparatus can be developed following similar principles. Such an apparatus would need to address thermal contact resistance, convection, radiation and other factors to ensure accurate thermal conductivity measurements.

4.2 Apparatus Design Development

To design an apparatus for accurate and precise thermal characterization of coated and uncoated fibers, all three modes of heat transfer must be considered: conduction, convection, and radiation. The energy balance for the apparatus would then be as follows:

$$Q = Q_{conduction} + Q_{convection} + Q_{radiation}$$ *Equation 4-2*

where Q is the total heat flow going into the fiber, $Q_{conduction}$ is the heat flow by conduction through the fiber, $Q_{convection}$ and $Q_{radiation}$ is the heat flow from fiber to its surroundings. In typical steady-state techniques, heat is applied to the sample through Joule heating using a resistive element. When current flows through the resistive element, the heat generated via Joule heating is directly proportional to the product of the applied voltage and current, as shown in Equation 4-6. While the heat transferred to the sample via Joule heating predominantly occurs through conduction, it is important to note that unless the sample is in direct thermal contact with the resistive element, additional conductive pathways may exist. In such cases, heat can transfer indirectly to the sample through intermediary components and may also dissipate into surrounding components in thermal contact with both the sample and the resistive element. These additional pathways can introduce significant sources of error in the measurement. To account for these various heat transfer mechanisms, the total heat energy delivered to the sample is expressed as:

$$Q_{sample} = Q_{joule} + Q_{conduction} + Q_{convection} + Q_{radiation} \qquad \textit{Equation 4-3}$$

where Q_{sample} is the sample's heat flow, Q_{joule} is the heat flow from the heater, $Q_{conduction}$ is the heat flow by conduction through the sample, $Q_{convection}$ is the heat flow by convections from the sample to its surroundings and $Q_{radiation}$ is the heat flow by radiation from the sample to its surroundings.

4.2.1 Apparatus Design Principle

The proposed apparatus is based on the steady-state guarded-hot-plate technique (ASTM C177) and the apparatuses developed by Piraux and Elkholy. It consists of a primary hot block, secondary hot block, and cold block. The secondary hot block obstructs heat loss from the sides of the primary block, forcing heat to flow to the cold block, through the sample. This constant flow of heat creates a steady-state temperature gradient along the sample. The temperature difference between the blocks, along with the known heat input power, allows for the calculation of the sample's thermal resistance and conductivity. This setup ensures accurate thermal conductivity measurements by minimizing heat loss. Figure 4-3 illustrates the thermal network model of the apparatus, providing a visual representation of heat flow through the sample. The model highlights the influence of contact resistance, as well as convective and radiative resistances, on the overall thermal resistance measured between T_1 and T_2. The heater assembly consists of a primary heater enclosed by an insulating barrier, which is further surrounded by a secondary heater. This design reduces heat loss from four out of six sides of the primary heater, leaving only the top and front exposed. The front of the primary heater contacts the sample, while the top remains exposed due to design constraints in assembling the heater assembly. Both hot and cold sides will implement a clamping mechanism to ensure good contact with the sample and reduce contact resistance.

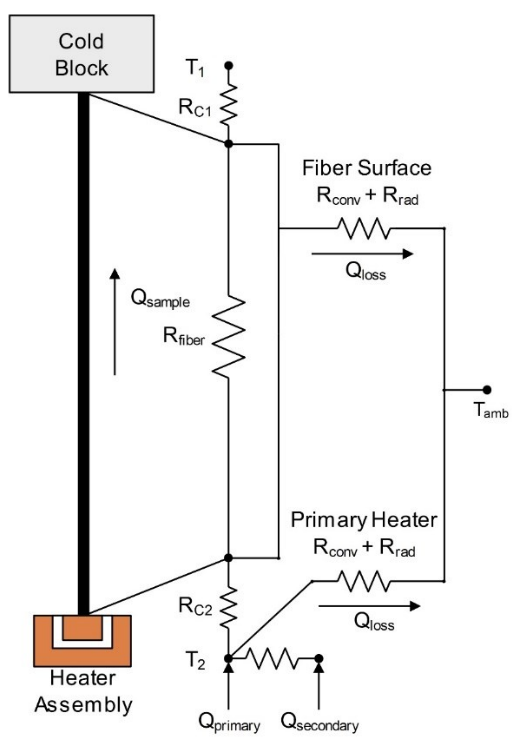

Figure 4-3: Thermal network model of the apparatus

The presence of microscopic irregularities and imperfections at the interface between two contacting materials creates microscopic pockets or air. Relative to the vast majority of materials, air's thermal conductivity is significantly lower [65], leading to significant thermal resistance between any two contacting materials. The measured thermal resistance encompasses both the bulk sample resistance and thermal contact resistance between the sample and apparatus. This relationship is mathematically described by Equation 4-4, where R_{meas} is the measured bulk thermal resistance, $R_{contact}$ is the bulk contact resistance, R_{sample} is the actual sample thermal resistance. The measured thermal resistance is calculated as shown Equation 4-5, where $T_2 - T_1$ is the temperature difference measured along the sample thickness and Q_{joule} is the heat applied to the sample through Joule heating and is calculated using the voltage and current supplied to the heating element as shown in Equation 4-6.

$$R_{meas} = R_{contact} + R_{sample}$$ *Equation 4-4*

$$R_{meas} = \frac{(T_2 - T_1)}{Q_{joule}}$$ *Equation 4-5*

$$Q_{joule} = V * I$$ *Equation 4-6*

$$R_{sample} = \frac{L}{k_{sample}\,A}$$ *Equation 4-7*

where R_{meas} is the sample's measured thermal resistance, $R_{contact}$ is the contact resistance between the sample and the hot/cold blocks, R_{sample} is the sample's thermal resistance without contact resistance, $T_2 - T_1$ is the temperature difference between the hot and cold blocks, Q_{joule} is the heater's heat flow, V is the voltage applied to the heater, I is the current applied to the heater, L is the sample length, k_{sample} is the sample's thermal conductivity, A is the sample's cross-sectional area.

With negligible contact resistance, R_{meas} would equal R_{sample}, and the sample thermal conductivity could be calculated using Equation 4-7. L represents the sample thickness (or more precisely, the distance between the two temperature sensors for $T_2 - T_1$. However, minimizing contact resistance requires extremely polished surfaces, which are costly to achieve and often impractical, especially for certain materials and fibers. One approach to bypass contact resistance is embedding temperature sensors directly within the sample at a distance L, though this is impractical for small samples like fibers. A more feasible solution is measuring thermal resistance at varying sample lengths and plotting thermal resistance versus length. In the absence of contact resistance, this plot would be linear and pass through the origin. However, when contact resistance exists, the plot shifts upward along the y-axis, resulting in a non-zero intercept. As shown in Equation 4-8 (derived from combining Equation 4-4 and Equation 4-7), the y-intercept corresponds to the total contact resistance $R_{contact}$, while the slope is $\frac{L}{k_{sample} A}$. By analyzing the slope and intercept, the material's thermal conductivity can be determined, even in the presence of contact resistance. It’s important to note that the contact resistance at both ends should be equal and consistent, and the greater the inconsistency in the contact resistance, the more inaccurate the measured thermal conductivity will be.

$$R_{meas} = \frac{L}{k_{sample} A} + R_{contact} \qquad \textit{Equation 4-8}$$

For Equation 4-5 to remain valid, $Q_{convection}$ and $Q_{radiation}$ must be zero or negligible. Any additional losses will cause the measured thermal resistance to deviate, either increasing or decreasing the slope in Equation 4-8, which directly impacts the calculated thermal conductivity and can lead to overestimation or underestimation. While accounting for convection and radiation is theoretically possible through calculations and simulations, the complexities involved often lead to long compute times and increased uncertainty, particularly given the system's geometry.

A common and effective solution to reduce the effects of convective heat transfer is through significantly evacuating air and bringing the testing environment to a high vacuum. Air acts as a fluid, enabling heat transfer through natural convection, where buoyancy drives warm air upward and cooler air downward due to gravity, or forced convection, where external forces such as fans move air to distribute heat. The lack of air, however, increases radiation which entirely depends on surface temperatures and emissivity. To further simplify, radiation can be reduced by employing a radiation shield. The design and effectiveness of radiation shielding is discussed in Section 4.5. With convection and radiation reduced to negligible amounts, contact resistance becomes the final problem. It is important to note that with a high vacuum, air is rarefied and as such the pockets between any two contacting materials is then closer to a vacuum, which has near zero thermal conductivity, further increasing the contact resistance. This can be remedied using Thermal Interface Materials (TIMS) to significantly reduce contact resistance and it’s important to choose specialized TIMs that are designed for use in high vacuum conditions, exhibiting low outgassing. Outgassing is the release of gases or vapors from materials in a vacuum environment, either by molecules diffusing through the vacuum chamber walls or desorbing molecules that were already adsorbed to the material surface before being exposed to a vacuum environment [66]. Additionally, vapor pressure affects the rate at which the more volatile components in the TIM will be outgassing since the boiling point of liquids are lower in high vacuum [67]. This contaminates the vacuum chamber and not only reduces the time taken to reach ultimate vacuum but also lowers it. Additionally, the TIM dries out much faster, which not only hardens and alters its thermal performance but also leads to inconsistent contact resistance across multiple tests. While specialized TIMs designed for high-vacuum environments exist, they are expensive and do not fully resolve the difficulty of cleaning between sample changes. Therefore, eliminating TIMs altogether is the preferred approach to ensure repeatable and consistent sample measurements.

The last step in the design development is to determine the appropriate range of sample sizes needed to accurately calculate thermal conductivity while accounting for TCR, as previously discussed. Since larger vacuum chambers are costly, keeping sample lengths small is preferable. Additionally, larger chambers require longer times to reach ultimate vacuum and may necessitate an expensive compensating vacuum pump. Moreover, the thermal resistance must be carefully balanced—if too high, other modes of heat transfer, such as convection and radiation, become more favorable, leading to higher heat leaks. Conversely, if too low, a high input power would be required to generate a sufficient temperature gradient. Based on the available lab equipment and instrumentation detailed later in Section 4.2.2, the chiller has a resolution of approximately 10 mK, and the power supply for the thermistor heater can output up to 20 mW. Additionally, the DAQ is capable of measuring with a resolution of 1 mK, making chiller stability the limiting factor. With a 10 mK temperature deviation and a 1 K temperature difference, the resulting error is remarkably low at just 1%. By incorporating the previously determined cross-sectional area of the fiber and considering the maximum output power of 20 mW at a 1 K temperature difference, Fourier's law of heat conduction can be rearranged to solve for the minimum acceptable sample length, L:

$$\mathrm{K} = \frac{QL}{A(T_2 - T_1)} \qquad \textit{Equation 4-9}$$

where K is thermal conductivity, Q is heat flow rate, L is thickness, A cross-sectional area, T_2 is hot side temperature, T_1 is cold side temperature.

The minimum acceptable length for the K13D2U fiber was determined to be 7 mm. The maximum length depends on the number of different sample lengths measured for the thermal resistance vs. length plot. While at least two lengths are required, measuring additional lengths improves accuracy by reducing uncertainty through curve fitting. The resolution of the length measurement device must also be considered. A simple millimeter ruler with 1 mm divisions introduces an uncertainty of ±0.5 mm when measured by eye, resulting in a 5% uncertainty for a 10 mm increment between two measurements. If five different lengths are measured, starting from 10 mm, the maximum length would be 60 mm, which would provide a large enough dataset for an accurate curve fit. Consequently, the adjustable distance between the cold and hot blocks should be approximately 70–80 mm, providing sufficient headroom for the 10–60 mm sample range.

4.2.1 Thermal Simulation of Guard Heating

Simulations are conducted to verify the effectiveness of the guard heating mechanism in ensuring one-dimensional heat flow during thermal conductivity measurements. By modeling the temperature distribution within the sample and surrounding blocks, the simulation assesses whether the applied guard heating sufficiently minimizes lateral heat losses. Due to the complexity of accurately modeling convection and radiation within the apparatus, these heat transfer modes are excluded, and only conductive heat transfer is considered. The primary objective is to confirm that the temperature profile remains uniform and one-dimensional, ensuring that all heat from the primary heater flows through the sample to the cold block without significant dissipation into the surroundings.

The apparatus was designed and analyzed in SolidWorks Flow Simulation, considering only internal conduction as the mode of heat transfer. Both wall conditions and initial conditions were set to a room temperature of 25 °C. The CAD model of the heater assembly along with the sample is shown in Figure 4-4. The assembly consisted of the primary hot block, primary hot block heater and temperature sensor, the guard hot block, guard block heater and temperature sensor, thermal breaks, two cylindrical pins, and the sample itself. The primary hot block was surrounded by thermal breaks to insulate and significantly reduce heat transfer on all sides except the contact surface with the sample. Additionally, the guard heater was designed to interrupt any heat leaks from the primary heater block by maintaining its temperature equal to that of the primary hot block. Since heat transfer requires a temperature differential, a near-zero temperature difference between the primary and guard heaters effectively eliminates heat transfer through the guarded sides. The thermal break clamp was used to press and hold the sample firmly against the primary block using a thumb screw, which is detailed later in the apparatus description. The two cylindrical pins represented a simplified model of the two screws used to mount the heater assembly to a platform. This platform was used to raise and lower the assembly at a set distance from the cold block according to the sample length. The platform was assumed to be at the same temperature as the vacuum chamber, potentially causing some heat leakage from the guard heater. This leakage could create nonuniformity within the guard block and, in turn, the primary hot block.

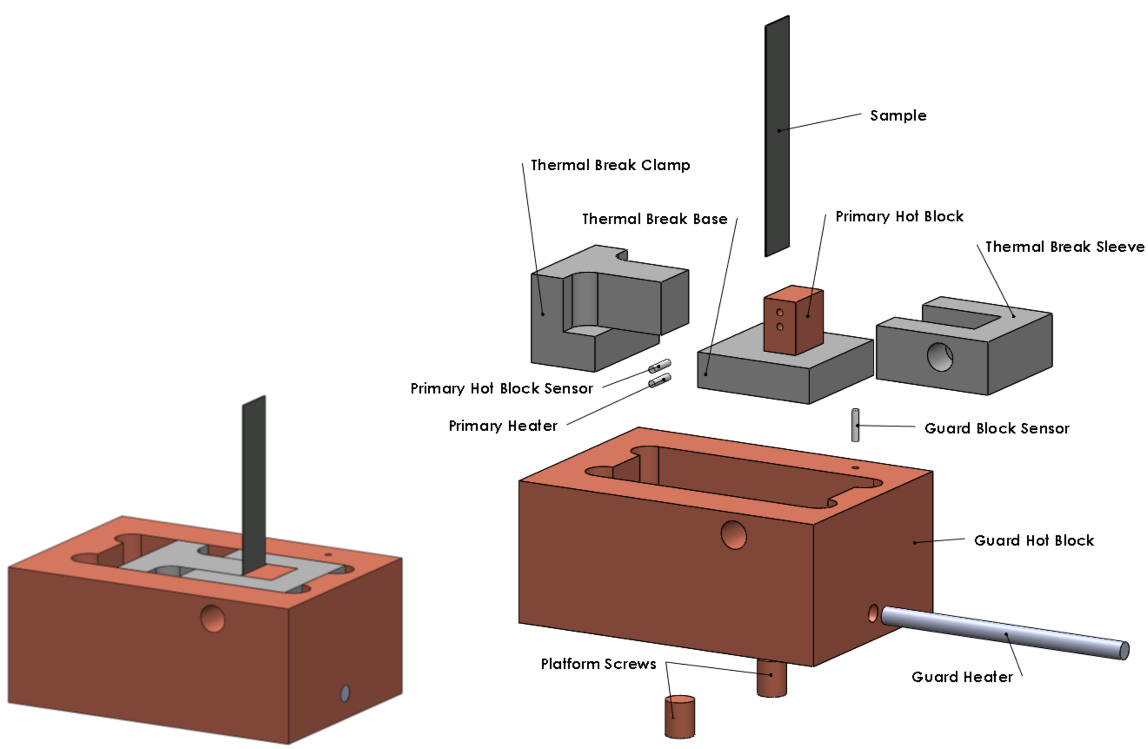

Figure 4-4: CAD model of heater assembly design and exploded view of all components used for simulation

Evaluating the thermal contact resistance (TCR) at the threaded interface between the guard heater and the mounting screws is challenging without experimental tests. Van Gils et al. studied the thermal contact conductance of aluminum alloy and stainless steel in vacuum under varying contact pressures and surface roughness [68]. Their research indicated that aluminum-to-stainless steel thermal resistance can range from 10^3 W/m^{2}K to 8x10^3 W/m^{2}K for a contact area of 50 mm^2 and a roughness of 0.4 μm, translating to a thermal contact resistance between 2.5 K/W and 20 K/W, with lower values occurring at higher contact pressures. This data was used to roughly estimate TCR between the screws and the platform. Given the small contact area of the screw and the added resistance from the threads, TCR between the screws and the guard heater block is probably even higher. A worst-case value of 10 K/W was used in the simulation. To simplify the simulation, TCR between the heater assembly and the sample, as well as within the assembly itself, is not considered since estimating it accurately is impractical. With a constant power input to both the primary and guard heaters, which are maintained at the same temperature, heat will predominantly flow through the sample as the path of least resistance. Though convective and radiative transfer will still have an effect, it is negligible everywhere except at the primary heater and sample. For the sample, the thermal resistance vs. sample length plot obtained experimentally will provide the required TCR to determine its thermal conductivity.

Since the cold block functions as a heat sink by maintaining a constant temperature, its inclusion in the simulation is unnecessary if its thermal mass is significantly larger than that of the sample. This ensures that with the heat being output by the primary heater, no significant temperature gradients can develop around the sample-to-cold block interface. Therefore, the end of the sample in contact with the cold block is assigned a boundary condition of 25 °C, the same as the bottom faces of the platform screws. All solids are initialized at 25 °C as well. Earlier, it was discussed that the K13D2U tow is naturally flat rather than cylindrical. To reflect this geometry while simplifying the model, the sample is represented as a rectangular cross-section. The width is maintained at approximately 2.5 mm, while the thickness is adjusted to match the total cross-sectional area of the tow. Modeling the individual microscale fibers would be computationally prohibitive, and this approach preserves the overall geometry while reducing complexity. The primary heater is set to deliver a constant heat output, calculated based on the sample length, cross-section, thermal conductivity, and a target temperature difference of 1 K. Initially, the guard heater is assigned the same power as the primary heater, and its output is iteratively adjusted to match the primary heater's temperature within a 5 mK tolerance. A mesh is generated with local refinements in smaller and critical regions of the geometry. Multiple simulations are conducted with different mesh sizes to ensure that the results are independent of mesh quality.

The results for a K13D2U sample length of 10 mm are shown below in Figure 4-5. The thermal conductivity calculated from the simulated temperature gradient was found to be 782 W/mK, approximately 2.2% lower than the expected 800 W/m·K.

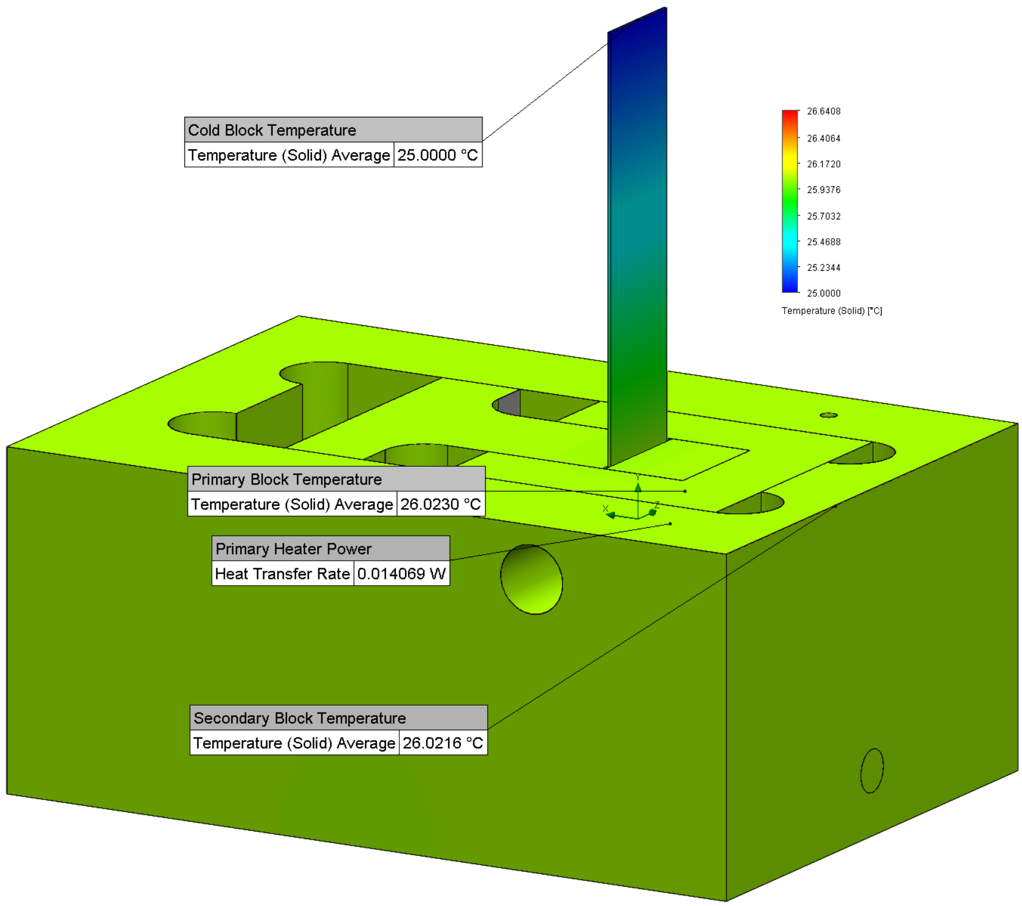

Figure 4-5: Simulation of guard heating apparatus with 10mm K13D2U sample

To investigate the discrepancy in the calculated thermal conductivity, a cut plot was generated, as shown in Figure 4-6. This cut plot provides a visual representation of the temperature gradient between the sample and the primary hot block's temperature sensor. However, due to the wide temperature range in the plot, small variations in temperature within the primary heater block are difficult to discern. To address this, a magnified view of the primary heater block was created with a custom temperature scale, as shown in Figure 4-7. Here it's clear that the temperature of the sample at exactly 10 mm from the cold block is about 25 mK lower than the temperature at primary block sensor. The only way to resolve this issue would be to either use a primary block with a much higher thermal conductivity than the sample to ensure a more uniform temperature within the block or to place the sensor at the 10 mm distance for a more accurate measurement. However, the resources required to implement these methods are not worth the 2% discrepency in measurement.

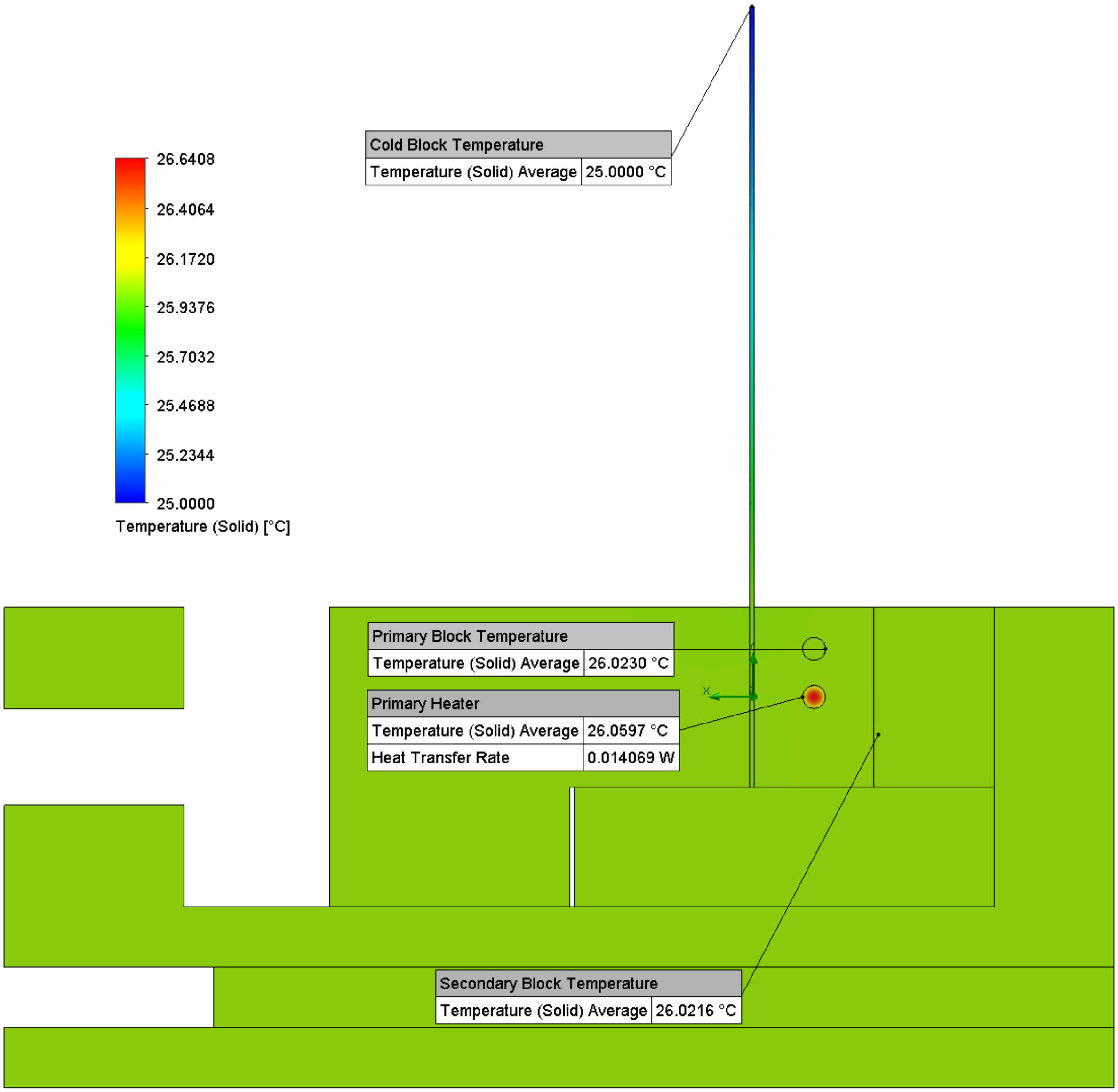

Figure 4-6: Midplane view of 10mm K13D2U sample simulation

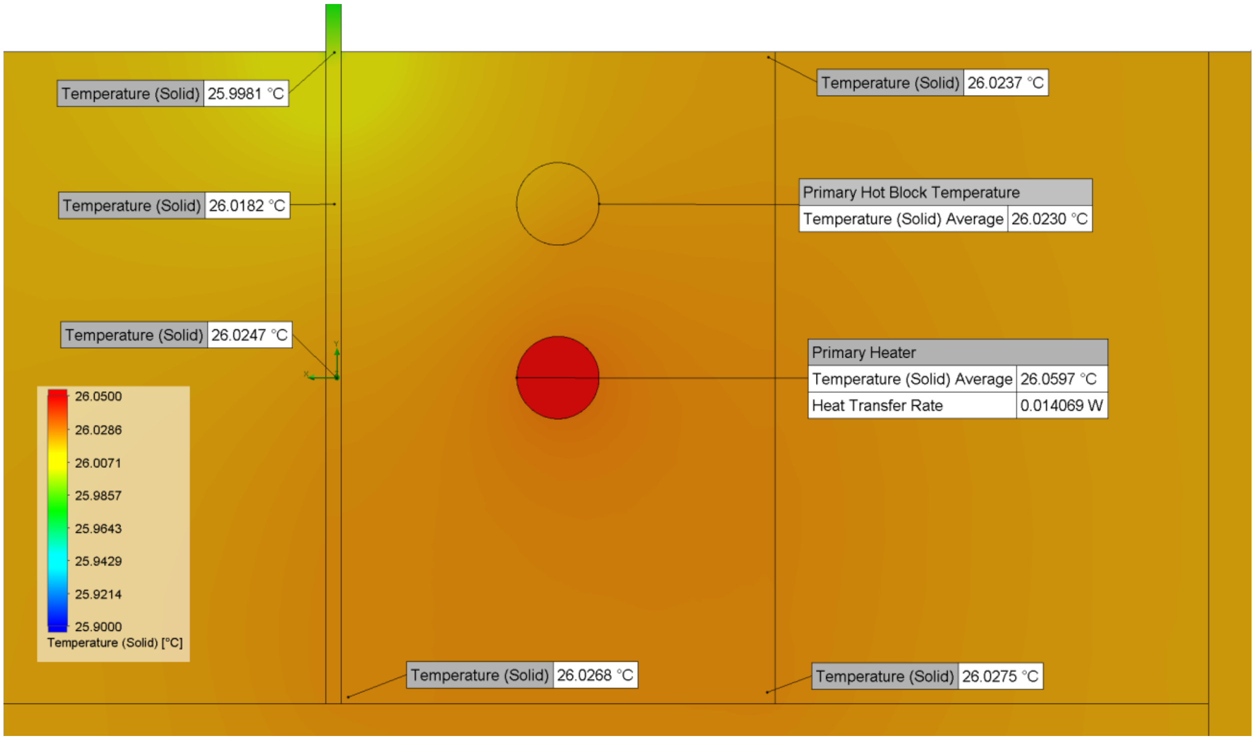

Figure 4-7: Magnified midplane temperature profile of 10mm K13D2U sample simulation

Simulations were performed for the entire range of sample lengths from 10-60 mm. The results as shown in Table 4-1, indicate that as the length of the sample increased, the error for the calculated thermal conductivity decreases. Starting at the 20 mm sample length, the calculated thermal conductivity is already within 0.8% of the actual thermal conductivity. This also suggests that the apparatus is going to be more accurate for materials with a higher thermal resistance. Based on these results, it would be best to test samples starting at a length of 20 mm to yield the most accurate thermal conductivity measurements overall. Though this is likely more circumstantial due to the sample's thermal resistance, where with a higher thermal resistance, a smaller sample length could give accurate measurements and so the limitation would then fall on the ability to precisely measure sample length.

Table 4-1: Simulation results and calculated thermal conductivity for K13D2U sample

Sample length (mm)	10	20	30	40	50	60
Primary heater power (W)	0.014069198	0.007035	0.00469	0.003517	0.002814	0.002345
Secondary heater power (W)	0.0168	0.0165	0.0165	0.0165	0.0165	0.0165
Primary block temperature (°C)	26.023	26.0079	26.005	26.0038	26.0033	26.003
Secondary block temperature (°C)	26.0216	26.0039	26.003	26.0028	26.0027	26.0026
Cold block temperature (°C)	25	25	25	25	25	25
Calculated Thermal Conductivity (W/mK)	782.0	793.7	796.0	797.0	797.4	797.6
Percent error	2.2%	0.8%	0.5%	0.4%	0.3%	0.3%

The simulations provide some verification for the core mechanics of guard heating but there are various other factors to consider such as TCR between the sample and primary heater block, the effect of a cylindrical geometry such as a PLA coated K13D2U tow, the internal TCR due to the fibers within the tow and the addition of PLA. These factors can't be simulated and require careful experimental testing and analysis. Additionally, experimental results can elucidate the effects of convection and radiation on measurements if experiments are done with known materials to validate against their recorded thermal conductivity values.

4.2.2 Instrumentation

The apparatus consists of several thermistors (TE Connectivity, GAG22K7MCD419), one of which is used as the primary heater in the heater assembly. An AC resistance bridge (LakeShore, 370 AC Resistance Bridge) is used to accurately measure thermistor resistance in a 4-wire configuration to eliminate lead wire resistance. The resistance bridge is adjusted to input very low excitation currents to the thermistors, significantly reducing error by self-heating. A 1mm RTD (Omega, 1PT100KN1510) is used as the secondary heater, powered by the resistance bridge's onboard current control functionality, which is used to precisely control the secondary heater power. A Sourcemeter (Keithley 2400) is used to precisely measure and control the primary heater power. All thermistors are calibrated using a platinum resistance thermometer (Fluke, 5606 PRT), as described in 4.4. The vacuum chamber is temperature-controlled using an external water chiller (Julabo F32-HE). A backing pump (Edwards E2M1.5) and turbomolecular pump (Edwards EXT70) are used inline to create a high vacuum environment within the chamber and negate convective losses. A Pirani gauge (Agilent PVG-500) and Penning gauge (Edwards AIM-S-NW25) are fitted to the vacuum chamber to measure internal pressure from atmosphere to 10^{-3} mbar and 10^{-2} mbar to 10^{-8} mbar, respectively. Voltage readings from the two gauges are measured and converted to mbar using an Arduino nano interfaced with MATLAB.

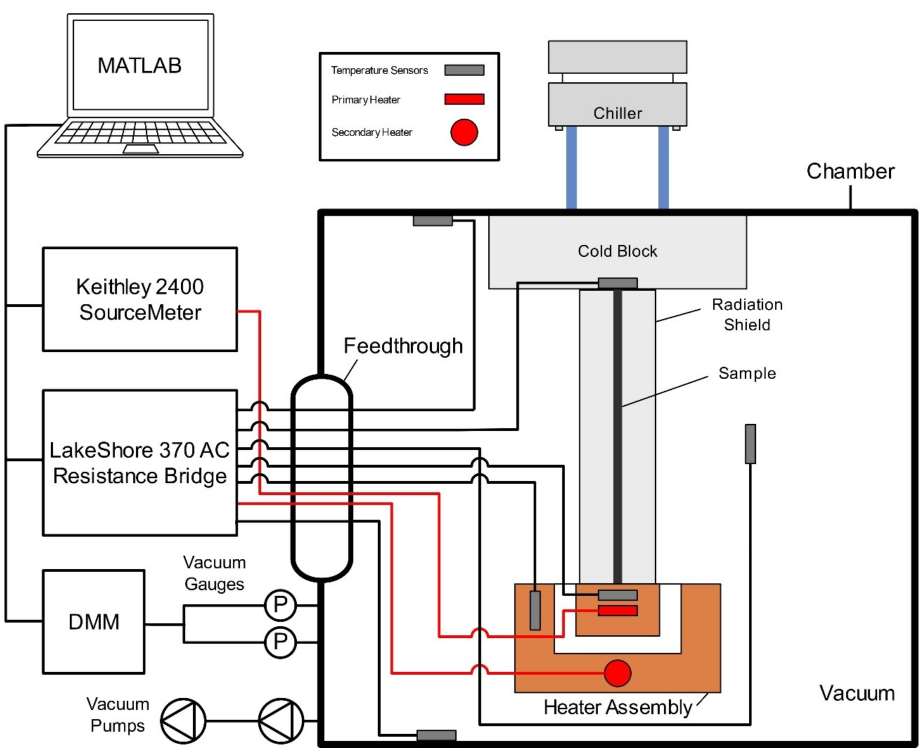

Figure 4-8: Instrumentation Schematic diagram of the apparatus

4.2.3 Apparatus Description

Experiments are conducted within a modular 6x6x6 inch 6061-T6 aluminum vacuum chamber purchased from IdealVacuum. It consists of a cubic frame with interchangeable side plates that come with a variety of features such as basic ports, internal face with a threaded breadboard layout for mounting components, thermal fixtures and other customizable options. For the apparatus, the vacuum chamber consists of a cubic frame, one blank plates, one hinged blank plate, one hinged plate with a window, one plate with a single large port, one plate with 4 ports, one plate with a thermal fixture, and various other utilities required to fit and assemble the vacuum chamber. As discussed previously, to account for contact resistance, measurements with varying sample length are required. To do this, a bottom and top frame were custom machined to house a threaded rod and smooth rod, supporting a custom machined platform for the heater assembly. The threaded rod and smooth rod are inserted into designated apertures in both the top and bottom frames, ensuring a fixed and predetermined separation distance as seen in Figure 4-9. Their placement restricts any vertical or lateral movement, permitting only rotational motion. This rotational motion, in turn, facilitates the upward and downward movement of the platform while maintaining alignment laterally. The heater assembly is fixed laterally on the platform using two positioning screws as seen in Figure 4-10. Both the top frame and heater assembly include a clamping mechanism shown in Figure 4-11. This allows the sample to be held in place with good thermal contact with the heater and top frame for heat transfer. The top frame is used as the cold block as it is mounted to the thermal fixture plate of the vacuum chamber. The thermal fixture can be connected to a water chiller to loop temperature-controlled water through it, keeping the top frame and clamp at a constant temperature while in contact with the sample. The platform can be adjusted as needed to allow for a maximum sample length of roughly 70 mm. Tension can be added to the sample by lowering the platform until the positioning screws are pulling the heater assembly while the sample is clamped. This allows samples such as fibers to be straightened to increase accuracy in length measurement.

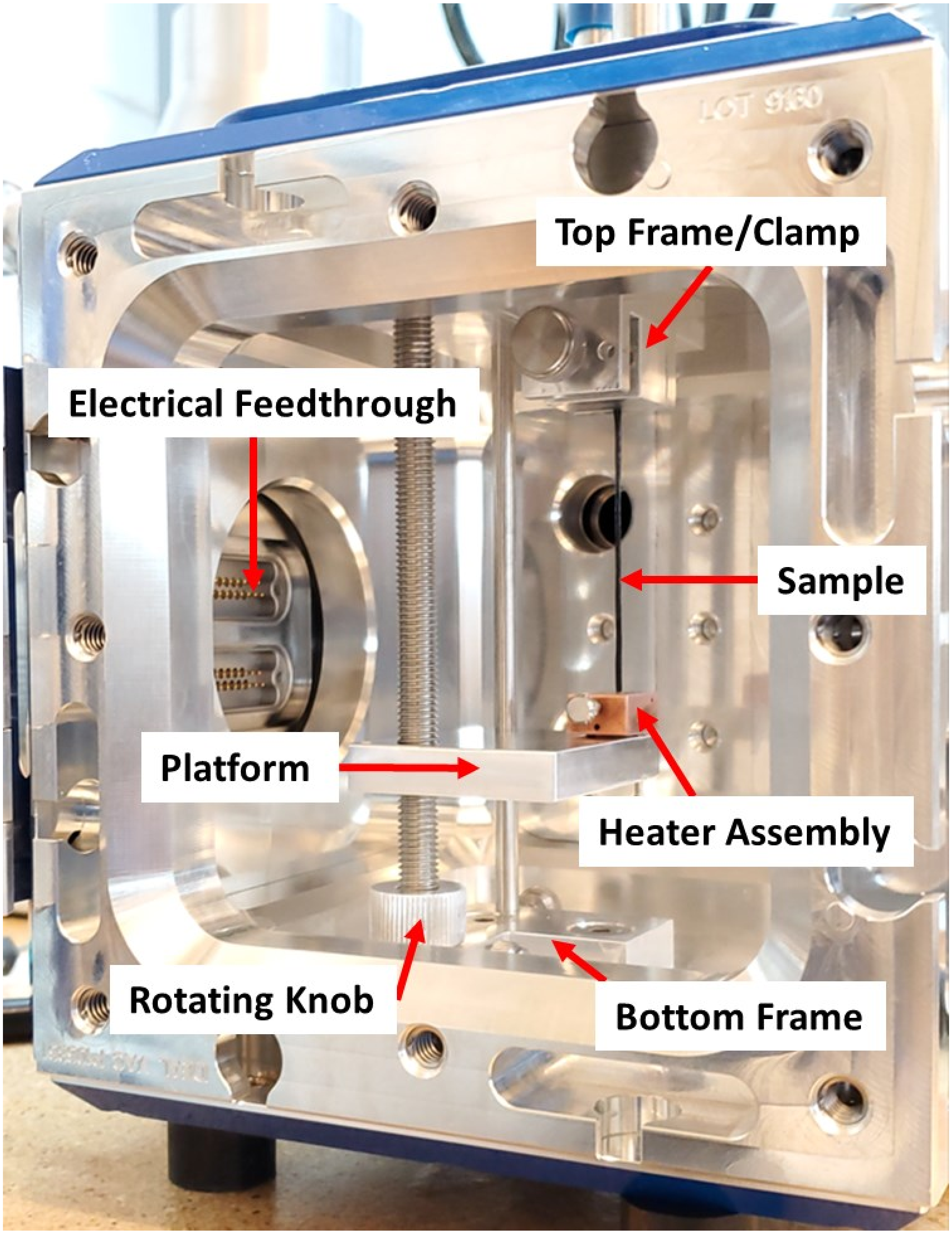

Figure 4-9: Vacuum chamber internal components, without heaters and sensors

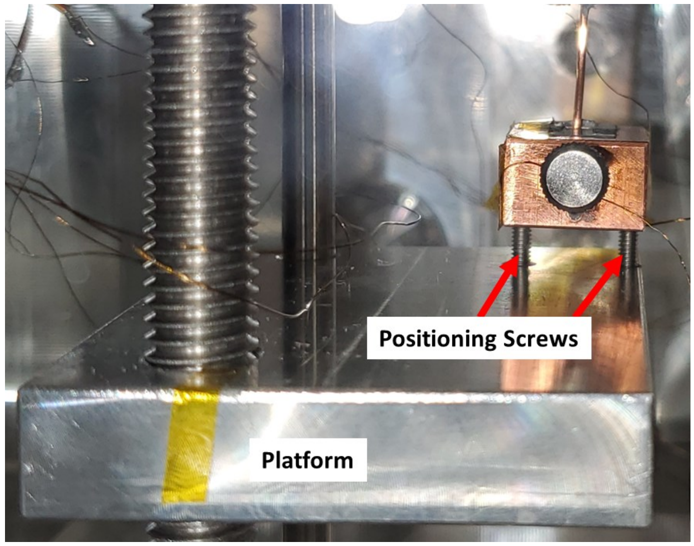

Figure 4-10: Heater assembly and platform

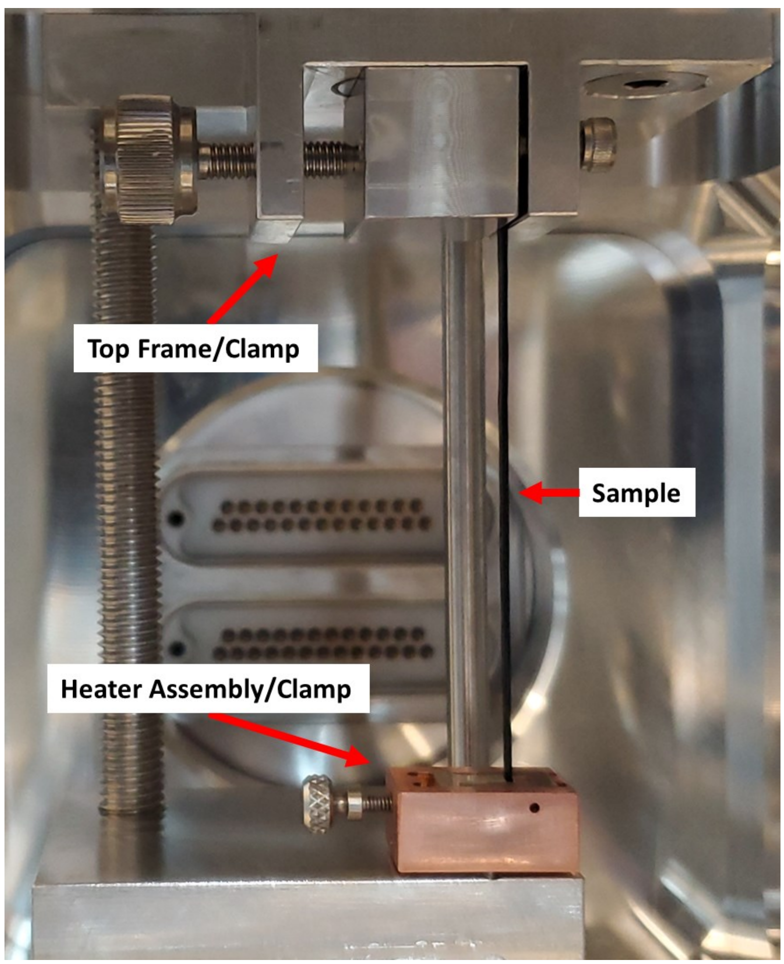

Figure 4-11: Side-view of the apparatus

To transmit temperature measurements and supply power to the heaters within the heater assembly, electrical connections were required between the vacuum chamber interior and the external DAQ system and power supply. This was achieved using an electrical feedthrough located at the back of the chamber, as shown in Figure 4-9. The feedthrough consists of a 2×25 pin D-Type connector mounted on a 4.50 CF flange, purchased from Accu-Glass Products. Since standard solder and wiring materials can introduce contamination through outgassing in a high-vacuum environment, specialized components were used. A 22 AWG Kapton-insulated, silver-plated copper solid-core wire from Accu-Glass was selected for its low outgassing properties. Silver solder was used to ensure reliable and vacuum-compatible electrical connections. Additionally, a high-vacuum D-Connector and gold-plated sockets, also sourced from Accu-Glass, were utilized to establish secure and low-resistance connections between the internal wiring and the external instrumentation. Once all wires were connected to the feedthrough, sensors were positioned throughout the system. Two thermistors were embedded in the primary heater block for heat output and temperature measurement, while a thermistor and RTD were placed in the guard heater block for temperature measurement and control. Additional thermistors were thermally coupled using copper tape to the inside of the vacuum chamber’s top and bottom surfaces, as well as to the cold block, to monitor the wall and sample cold temperatures.

Each experiment begins with the vacuum chamber open, and the vacuum pumps turned off. The heater assembly platform is adjusted based on the sample length. Samples are prepared by cleaning them with IPA to remove contaminants, cutting them to length using sharp razors, and, in specific cases, lightly sanding their surfaces to minimize TCR. The sample is first placed in the heater assembly and clamped securely with enough force to hold it in place without deforming it, while the opposite end is aligned vertically and clamped into the cold block with the same careful approach. The platform is then lowered until the positioning screws apply slight tension to the sample through the heater assembly, as shown in Figure 4-10. Samples with low emissivity do not require radiation shielding, but most tested samples have higher emissivity and require a radiation shield, as discussed in Section 4.5. The shield consists of multiple layers of aluminum foil formed into a tube concentric to the sample, with identical construction across all tests but varying lengths to accommodate different sample sizes. Once the sample is secured and the radiation shield is positioned, the sample is clamped to the cold block with minimal line-of-sight exposure to surrounding components, and the platform is lowered to ensure proper tension. After measuring the sample length—defined as the distance from the top of the heater assembly to the bottom of the cold block—the vacuum chamber is sealed, and the pumps activated. The chiller maintains a constant temperature of 25 °C while the chamber reaches a pressure of approximately 2×10^{-5} mbar. The experiment is controlled via MATLAB, interfaced with a DAQ and power supplies, where the heater output is set based on the sample length and a target temperature difference of 1 K. The test runs until steady state is achieved for the hot block, guard heater, and cold block temperatures. The procedure is repeated by cutting down the same sample and measuring its thermal conductivity for multiple lengths to accumulate thermal resistance vs length data. The data is then processed to generate a thermal resistance vs. length plot. Each iteration of tests is done after visual inspection of the heater assembly and both the clamps used to hold the sample in place, checking if contacting surfaces are smooth and contaminant free to ensure consistency.

4.3 Temperature Sensor Calibration

The accuracy and precision of thermal resistance measurements are directly tied to the sensors incorporated into the apparatus. Voltage and current measurements are obtained through accurate Data Acquisition Systems (DAQs), with each system detailing its accuracy in the accompanying datasheet. Temperature measurements utilize a 0.38mm 22 kΩ NTC thermistors, exhibiting a nonlinear relationship between thermistor resistance and temperature, where the resistance decreases with an increase in temperature. In the case of multiple thermistors, it is crucial to calibrate each thermistor to a reference probe. This calibration ensures that all thermistors converge to the same temperature when held at a specific temperature, minimizing errors and enhancing measurement consistency.

The thermistors were calibrated using a high-accuracy Platinum Resistance Thermometer (5606 Full Immersion PRT, Fluke) as the reference probe. For precision, all thermistors were closely grouped together and affixed with thermal paste directly to the reference probe, ensuring optimal thermal contact and accuracy in temperature measurements. Subsequently, the reference probe was fixed to the vacuum chamber cold plate. The Julabo chiller was then employed to set the cold plate to temperature setpoints ranging from 15°C to 35°C in 1°C increments, while simultaneously recording resistance measurements from all sensors at steady state.

A study by Liu et al [69] compared nine different calibration equations within a temperature range of 278.15-328.15 K to determine the equation with the lowest standard deviation. The Steinhart-Hart equation was found to have a deviation of about 5.93 mK, whereas the Hoge-2, Hoge-3, and fifth-order equations demonstrated deviations of 0.23 mK, 0.22 mK, and 0.21 mK, respectively. Notably, the fitting quality of the Hoge equations only marginally improved beyond the third order, with a mere 0.01 mK decrease in error. Consequently, the Hoge-2 equation, with its simpler form, was selected as the optimal calibration equation for high-precision temperature measurements.

To validate Liu's results, the thermistors underwent calibration using the Steinhart-Hart, Hoge, and polynomial equations. The error, calculated as the temperature difference between the probe temperature and the calibrated thermistor temperature, revealed that the third-order polynomial equation and the Steinhart-Hart equation exhibited the largest error. Surprisingly, both the fourth and fifth-order polynomials showed slightly lower error compared to the Hoge equations. However, increasing the order of both the Hoge and polynomial equations beyond the fifth-order had negligible change while also having similar error. Consequently, the fifth-order polynomial equation was chosen as the calibration equation due to its simplicity compared to the Hoge equations.

Steinhart—Hart equation:

$$\frac{1}{T} = A_0 + A_1\, ln(\, R_T) + A_3(ln(R_T))^3$$ *Equation 4-10*

Hoge-2 equation:

$$\frac{1}{T} = A_0 + A_1\, ln(R_T) + A_2(ln(R_T))^2 + A_3(ln(R_T))^3$$ *Equation 4-11*

Hoge-3 equation:

$$\frac{1}{T} = A_0 + A_1\, ln(R_T) + A_2(ln(R_T))^2 + A_3(ln(R_T))^3 + A_4(ln(R_T))^4$$ *Equation 4-12*

Fifth-order equation:

$$\frac{1}{T} = A_0 + A_1\, ln(R_T) + A_2(ln(R_T))^2 + A_3(ln(R_T))^3 + A_4(ln(R_T))^4 + A_5(ln(R_T))^5$$ *Equation 4-13*

Polynomial equation:

$$T = A_0 + A_1 R_T + \ldots\ldots\ldots + A_{n-1}(R_T)^{n-1} + A_n(R_T)^n$$ *Equation 4-14*

where T is temperature, A_i are coefficients, R_T is the thermistor resistance.

Table 4-2: Error calculated using selected calibration equations for thermistors

Calibration Equation	ΔT_{error} (mK)
Steinhart—Hart	13.1
Hoge-2	9.3
Hoge-3	7.8
Fifth-order	9.6
Third-order polynomial	38.5
Fourth-order polynomial	9.8
Fifth-order polynomial	6.7

4.4 Heat Loss Calibration

Analyzing the thermal network model in Figure 4-8, there are two primary sources of heat losses that need to be mitigated or considered. The first source is the exposed surface of the primary heater, as depicted in Figure 4-12. The second source is the surface of the fiber. Both surfaces are not subject to any conductive losses, except for the essential one-dimensional conduction through the fiber. However, convection and radiation effects come into play for the two surfaces. Convective losses are assumed to be very low and negligible due to high-vacuum conditions, leaving radiation as the dominant mode of heat transfer. The radiative loss from the fiber is quantified in the next section.

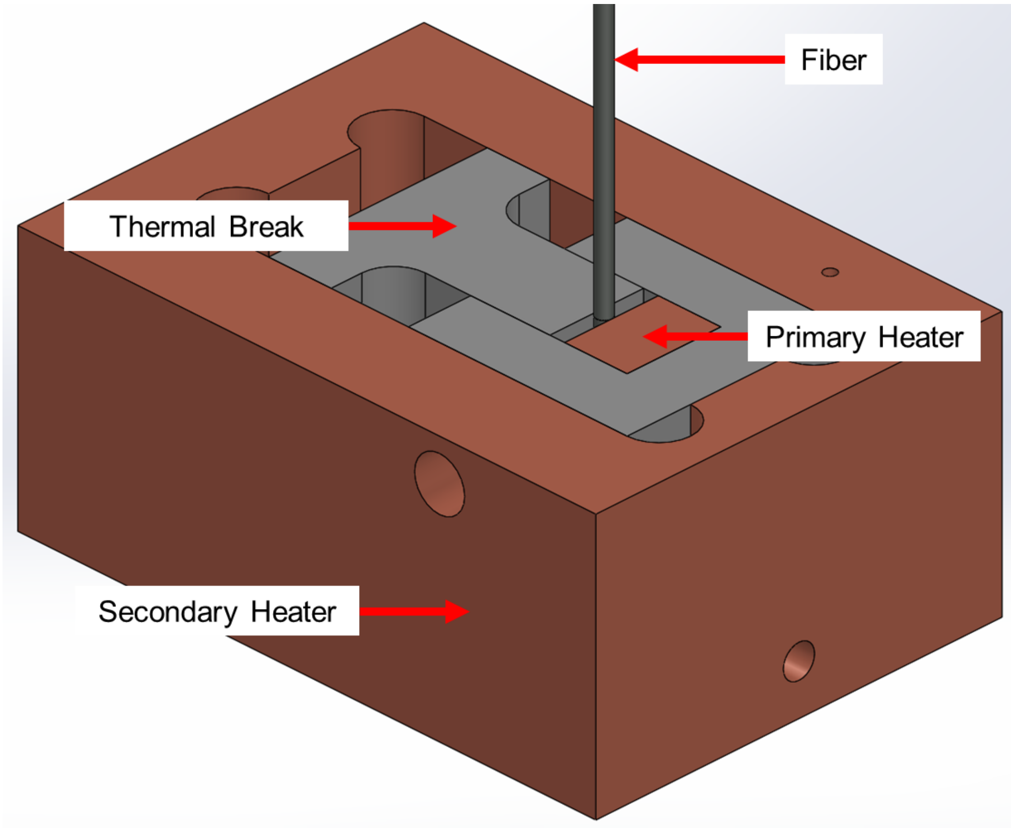

Figure 4-12: CAD model of the heater assembly

To quantify the heat lost from the primary heater, the secondary heater is used to simulate a range of temperature gradients similar to those experienced during sample testing. By adjusting the input power to the secondary heater, the temperature of the heater assembly is controlled. As a result of heat losses, the secondary heater block generally attains a higher temperature than the primary heater block. Maintaining thermal equilibrium between the two blocks necessitates a constant input of power to the primary heater, which directly corresponds to the heat lost from the primary heater block under the temperature gradient conditions between the heater assembly, chamber, and cold block during sample testing. By repeating this process for at least three different temperature gradients, a plot can be generated, as shown in Figure 4-13, illustrating the relationship between the heat lost from the primary heater block and the temperature difference between the heater assembly and the cold block. The equation derived from this curve can then be used to estimate the heat lost from the primary heater for any given temperature gradient during sample testing.

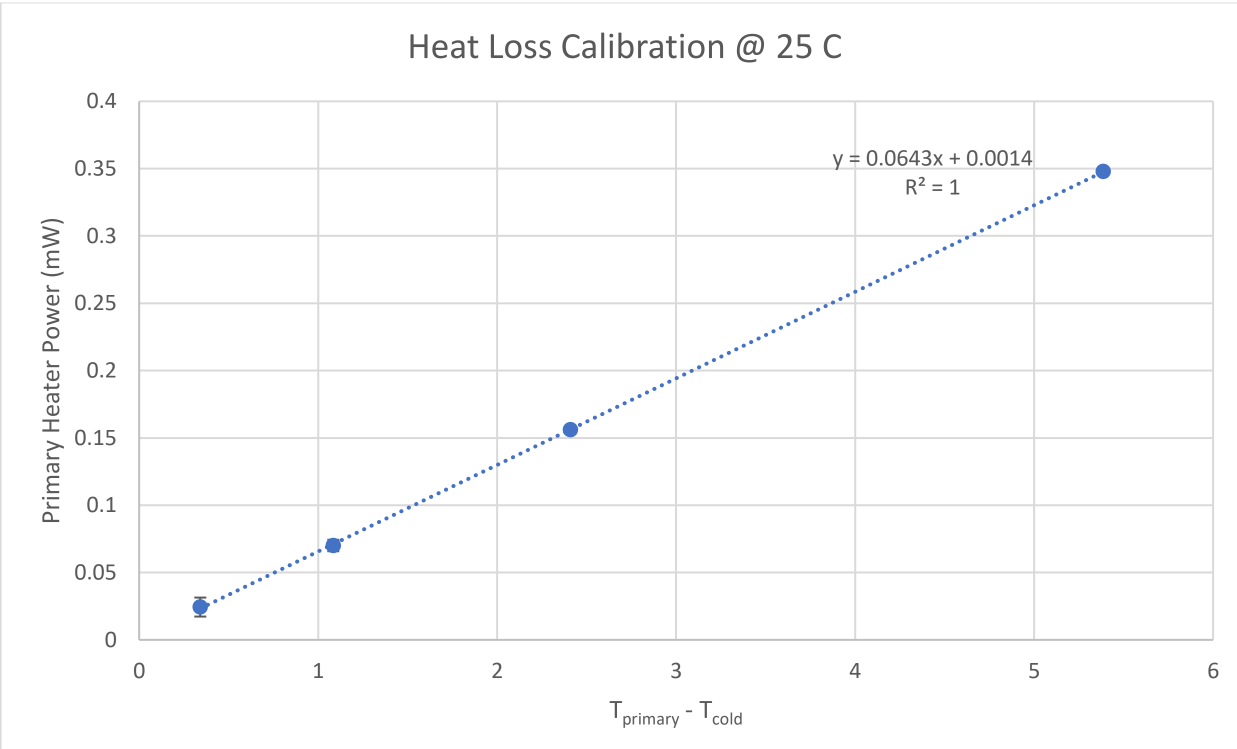

Figure 4-13: Experimental heat loss calibration curve.

Emphasizing the importance of achieving accurate estimates for heat loss from the primary heater, the calibration process is meticulously conducted under conditions that closely mirror those encountered during typical sample testing. This involves external insulation of the vacuum chamber to minimize temperature gradients within the chamber and a radiation shield suspended between the heater assembly and the cold block. The radiation shield is strategically positioned to avoid contact with either the heater assembly or the cold block, thereby eliminating any heat loss introduced through conduction within the shield. Utilizing the equation derived from the heat loss calibration, the primary heater input power can be appropriately corrected to account for heat loss from the primary heater itself.

4.5 Sample Radiative Heat Transfer

Olcun's attempt to quantify combined effects of radiation and convection, using a heat loss calibration similar to the one described in Section 4.4, suggested that radiation had minimal influence on the measurements. By applying the Stefan-Boltzmann law, he estimated that lateral radiation from the samples accounted for less than 1% of the total heat transfer due to their small surface area. To validate this assumption, he compared the thermal conductivity of regular and black spray-painted copper wires, where the latter had an increased emissivity. Since both wires produced similar thermal conductivity results, it was concluded that radiative heat loss was negligible. However, applying this to CPCF tows raises several concerns. Unlike a single cylindrical copper wire, CPCF tow has a macroscopic rectangular cross-section composed of hundreds of microscopic fibers circular in shape. Additionally, the emissivity of a painted copper wire may not accurately represent that of CPCF tow materials, particularly when considering variations in fiber coatings and surface conditions. Furthermore, uncertainties arise from various experimental factors such as surrounding temperatures, sample temperature differences, and potential heat transfer interactions that were not accounted for in Olcun's study. While characteristics such as the microscale fiber structure, cannot be precisely modeled, simplifications can be used to calculate an estimated radiative heat loss. If the estimate suggests that radiation is non-negligible, mitigation strategies would be required to ensure accurate thermal conductivity measurements.

The first step was to reevaluate the Stefan-Boltzmann law specifically for CPCF tows. Assuming a grey body, and the surrounding surface area is much larger than the surface area of the fiber tow, the equation for radiation is then:

$$Q_{rad} = \epsilon\sigma A(T_{surface}^4 - T_{surroundings}^4) \quad \textit{Equation 4-15}$$

Where Q_{rad} is the heat flow by radiation, ϵ is the emissivity of the fiber tow, σ is the Stefan-Boltzmann constant, A is the estimated surface area of the fiber tow and $T_{surface}$ and $T_{surroundings}$ are the surface temperature of the fiber tow and surrounding temperature, respectively. The surface temperature can be determined using the Fourier's law of conduction, but the emissivity of the fibers needs to be determined, along with the approximate surface area of the tow.

FTIR spectroscopy was used to measure the emissivity of household aluminum foil and K13D2U fibers. The spectrometer employs an integrating sphere to measure the directional-hemispherical reflectance of the sample. The reflectance data is then processed in MATLAB using a Gaussian-weighted averaging method to minimize noise in the measurements. The spectrometer measures within a spectral range of 2–25 μm, which covers approximately 83% of the total blackbody spectral emissive power at 25 °C. Beyond this range, the reflectance data exhibited linearity at longer wavelengths, enabling extrapolation to approximate the reflectance outside of the spectrometer range. The filtered and extrapolated reflectance data is then used to compute the total hemispherical emittance of each material. The emissivity of the aluminum foil was found to be approximately 0.03, while K13D2U fibers had an emissivity of 0.81. To ensure accuracy, a dense bundle of K13D2U fibers were used, with care taken to eliminate visible gaps between fibers. Measurements were performed both with and without aluminum foil backing the fiber stack to confirm that gaps between fibers were not large enough to affect the reflectance.

The simplest way to approximate the fiber tow surface area is by assuming it has a rectangular geometry. The assumption is based on the arrangement the fibers come in from the manufacturer as seen in Figure 3-1, where the fibers are packed and shaped into a thin rectangular cross-section. While the fiber tow visually looks rectangular in shape, it is composed of hundreds of micro-scaled cylindrical fibers, which increases the surface area of the fiber tow. Only the fibers that are exposed to the surroundings are to be considered for the surface area, which can largely vary due to the fibers being loosely held together. An assumption can be made on the number of fibers exposed on each side by taking the measurement of the fiber tow width, which was found to be around 2.5 mm. With the cross-sectional area and width of the fiber known, the thickness can be determined. The thickness and width can then be used to estimate the number of fibers that are on each side on average using the average fiber diameter determined in Section 3.2.1. Assuming an ideally packed fiber tow, the exposed fibers would be perfectly vertical and next to each other with no gaps. In this arrangement, all the outer fibers have approximately half their surface area exposed to the surroundings, which can be used to estimate the total surface area of the fiber tow.

Since the fiber tow has a varying temperature across its length, the equation for radiation can still be used if the fiber tow is cut into several sections, each with its own temperature. The sum of the calculated radiative heat loss from each section would then give the estimated total radiative heat loss for the entire length of the fiber tow. For a 60 mm long fiber tow with a 1 K temperature difference, the radiative heat loss was 1.2 mW, which is about 51% of the heat going into the fiber tow. While this calculation is a rough estimate for the effect of radiation on the fiber tow, it is nonetheless a clear indication that radiation is non-negligible. One approach to reduce radiation is to lower the temperature difference, however, radiation can be seen to behave linearly when the sample temperature is very close to the surrounding temperature. This means that at a certain temperature difference and below, the decrease in radiation will suffer from diminishing returns as radiation acts more linearly, the same as conduction. This relationship can be seen in the graph below, which shows that at a temperature difference of less than 100 K, the difference between the radiant heat lost from the sample vs the heat going into the sample by conduction remains the same. Thus, decreasing the temperature difference between the sample and the surroundings will have no effect other than decreasing the measurement accuracy due to temperature measurement resolution.

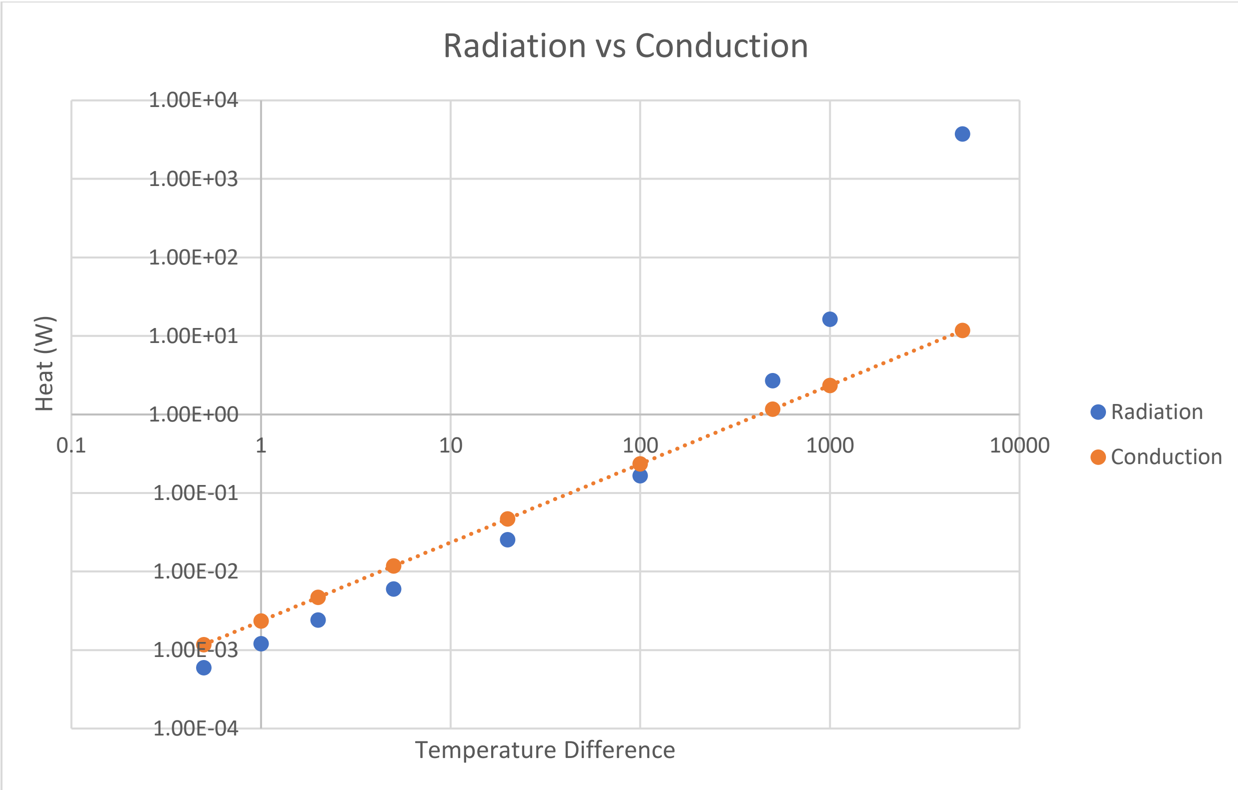

Figure 4-14: Linearity of radiation at temperatures close to surrounding

Another approach for mitigating radiative heat transfer is to implement a radiation shield, which is designed to reflect the heat emitting off the sample back to itself. The book Radiative Heat Transfer by Modest [70] goes over the design and principles of radiation shields using highly reflective materials such as thin metallic foils. As such, household aluminum foil was measured for reflectance earlier along with the K13D2U sample, resulting in a very low emissivity of 0.03. Given its high reflectance, low cost and commercial availability, aluminum foil makes for an effective material for radiation shielding. Radiation shielding typically has an arrangement of several layers of reflective foils that are all parallel and closely spaced, with more layers further reducing radiation. Chapter 5.5 of the book highlights an equation used to determine the number of shields required to limit the radiant heat flux from a cylindrical surface surrounded by concentrically placed, parallel shields. Though this scenario doesn't apply to the rectangular shaped fiber tows, it can still be used to get a starting point for the number of shields potentially required. Using the surface area of the 60 mm fiber tow determined earlier and using an aluminum radiation shield with a diameter of 5 mm, it would require at least 4 layers of aluminum foil to reduce radiation down to 0.5 % of the heat applied to the fiber tow by conduction. Due to aluminum's high thermal conductivity, each layer of foil needs to be separated by a thermally resistive barrier to reduce conductive heat transfer. To achieve sufficient thermal resistance between each layer, while maintaining reusability and structural integrity, each shield is constructed using a 3 mm wide strip of double-sided tape at the top and bottom of the foil. This configuration allows successive layers of foil to be rolled over each other, adhering together to form a tube-shaped radiation shield. A 5 mm wooden dowel pin is used to construct each shield, keeping the diameter and circular shape consistent. A total of five radiation shields were fabricated, ranging from 20 – 60 mm to cover the different sample lengths to be tested.

4.6 Uncertainty Analysis

Uncertainty analysis is a critical component of any experimental study, providing a quantitative assessment of potential errors in measured and calculated values. The development of an accurate apparatus requires careful uncertainty analysis. Uncertainty analysis can be used to evaluate the impact of measurement limitations, material variability, and various experimental conditions that influences the overall accuracy of the reported values. Understanding uncertainties is essential for interpreting results, comparing them to existing data, and refining experimental techniques to minimize errors in future studies. This section outlines the sources of uncertainties, the methods used to quantify and propagate them, and the strategies employed to minimize their impact on the results.

When calculating sample thermal resistance, Equation 4-5 relies on measured temperature, as well as the voltage and current supplied to the primary heater to calculate the heat output. The Keithley 2400 Sourcemeter manual specifies measurement accuracies for voltage and current across specific ranges, as detailed in Table 4-3. The standard deviation for resistance to temperature conversion determined during thermistor calibration in Section 4.3, was 6.7 mK. The chiller was set to a constant temperature over a 30-minute period, and temperature measurements were recorded to assess deviations due to the chiller, resulting in a measured cold block temperature deviation of up to ±10 mK. The sample length was measured using a small ruler with 1 millimeter resolution. For a ruler with millimeter resolution, as per the Guide to the Expression of Uncertainty in Measurement (GUM), the uncertainty is half the smallest division which is ±0.5 mm [71]. Lastly, the cross-sectional area was calculated using density, mass and length of the fiber with the method discussed in Section 3.2.2.

Table 4-3: Measurement uncertainties in apparatus

Parameter	**Uncertainty**	
Voltage, V	Measurement Range	± (% of reading + volts)
	200 mV 2 V 20 V 200 V	0.012% + 300 μV 0.012% + 300 μV 0.015% + 1.5 mV 0.015% + 10 mV
Current, A	Source Range	± (% of reading + amps)
	1 μA 10 μA 100 μA 1 mA 10 mA 100 mA 1 A	0.035% + 600 pA 0.033% + 2 nA 0.031% + 20 nA 0.034% + 200 nA 0.045% + 2 μA 0.066% + 20 μA 0.27% + 900 μA
Sample thickness (length), L	0.5 mm	
Sample density, ρ	3000 $\frac{g}{m^3}$	

Sample mass, m	0.3 mg
Sample length (for cross-sectional area), L	0.02 mm
Temperature difference, dT	0.0141 K

Thermal resistance for each sample is calculated through measurements using Equation 4-5. Using the equation from the heat loss calibration curve, the measured heater power is corrected for heat loss before being used to calculate the thermal resistance of the samples. Further, the thermal resistance vs sample length is used to determine the slope of the trend and in turn the thermal conductivity by rearranging Equation 4-8. The uncertainties involved with the individual variables within each equation was propagated using the method developed by Kline and McClintock [72]. However, the uncertainty from the slope and intercept from both the heat loss calibration curve and thermal resistance vs length plot require a different approach to propagate. The built-in features offered by Excel's LINEST function were used to determine the standard deviation and confidence interval for both the slope and intercept of any trends. The methods and details behind Excel's LINEST function is discussed by Morrision [73]. A combination of error propagation by Kline and the standard deviation from Excel's LINEST was used to determine the estimated reliability of the final thermal conductivity value of the samples with a confidence interval of 95%.

4.7 Results and Discussion

In the theoretical analysis and simulations discussed above, a temperature difference of 1 K was chosen between the hot and cold sides of the sample. However, real-world experiments can deviate from simulated results due to factors such as contact resistance, non-uniform heating, or environmental heat losses, potentially leading to unreliable or inaccurate measurements. To verify the reliability of the experimental results, a thermal conductivity vs. temperature difference experiment was conducted to confirm that the calculated thermal conductivity remains consistent and is not affected by changes in the imposed temperature gradient. Silver wire and K13D2U were both tested with a varying temperature difference ranging from near 0 - 2 K at room temperature. The results shown in the graphs below indicate that both the silver wire and K13D2U tow have almost no effect on measured thermal conductivity when the temperature difference is at least 0.5 K. Thus, all tests are conducted with a temperature difference of 1 K to minimize measurement uncertainty.

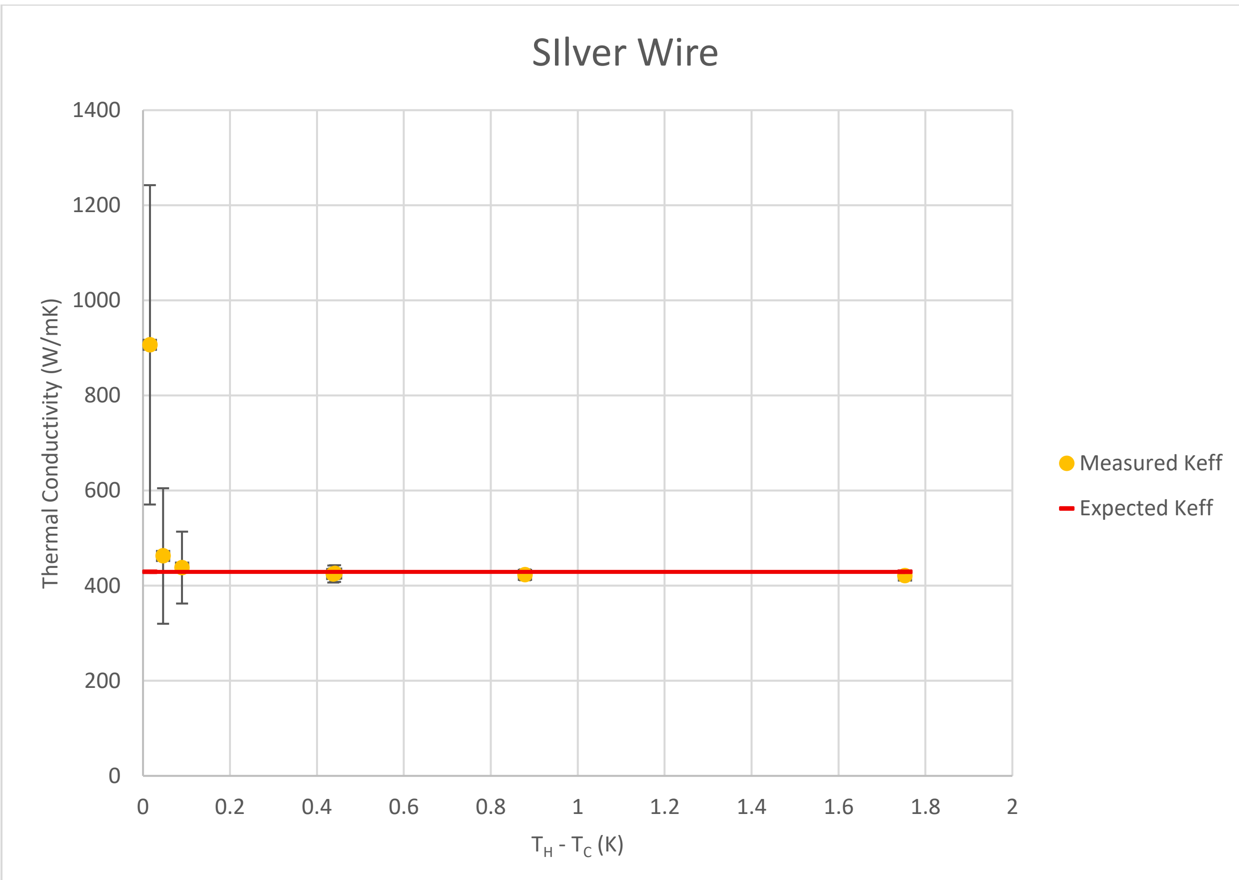

Figure 4-15: Silver wire thermal conductivity vs temperature plot with experimental results

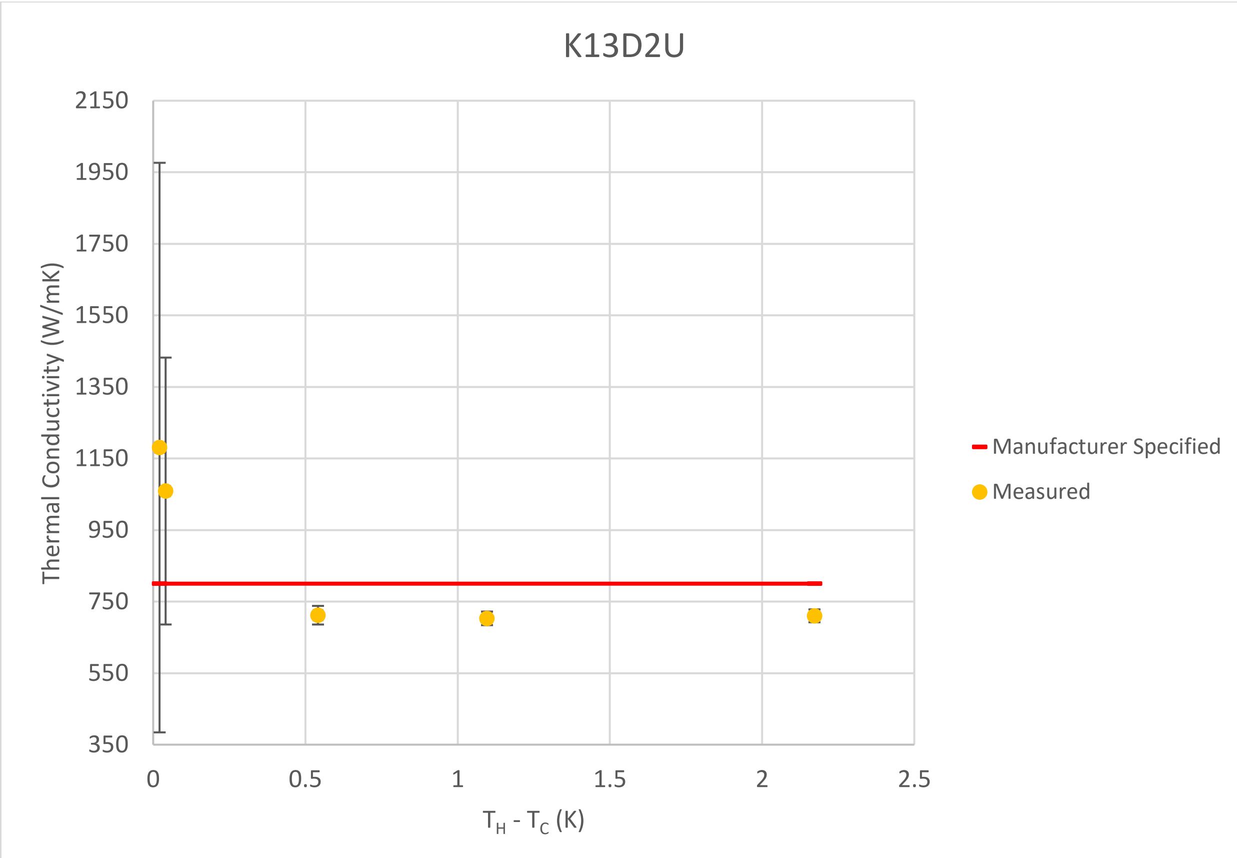

Figure 4-16: K13D2U tow thermal conductivity vs temperature plot with experimental results

The next challenge was to validate the apparatus using materials with known thermal properties and to quantify its accuracy. This was achieved using two different diameters of metal wire: one with a much higher thermal resistance to test the apparatus's limitations along with somewhat mimicking the individual fiber filament within the K13D2U tow and another with a similar thermal resistance to the K13D2U tow. The measurement process remained the same for both metal wire and fiber tow, where the cross-sectional area was determined through volume, mass and density using Equation 3-2. The results were processed to generate a thermal resistance vs. length plot. Silver wire was selected due to its high thermal conductivity and practicality for apparatus validation. While a material with thermal conductivity nearly identical to that of K13D2U would offer the most accurate validation, such a material is difficult to find—especially one that is well-documented, readily available, and cost-effective. Despite the geometric differences between metal wire and the flat K13D2U fiber tow, silver wire was the most feasible option. Two silver wires were selected: one with a thermal resistance comparable to the fiber tow, and another with a higher thermal resistance to assess the apparatus's ability to measure more resistive samples for potential future applications. The silver wires were purchased from Surepure Chemetals with a 99.99% (4N) purity. Additionally, C110 copper wires were also purchased due to its high thermal conductivity after silver and cost effectiveness.

The measurements using the high-vacuum apparatus are listed in Table 4-4. The thermal resistance vs length plots for the silver wires are shown in figures Figure 4-17 and Figure 4-18. The tests, performed with radiation shielding, show a linear trend between the thermal resistance and length, indicating a consistent contact resistance between each length of wire measured. The 0.81 mm silver wire exhibited significantly lower error compared to the 0.21 mm wire. The increased error in the 0.21 mm wire can be attributed to its higher thermal resistance and greater susceptibility to contact resistance due to its smaller diameter. Given silver's high malleability, it is likely that the clamps deform the ends of the thinner wire during installation, increasing thermal contact resistance and introducing variability in the measurements. Microscopically, the smaller surface area of the 0.21 mm wire and surface roughness of the hot block leads to much higher and inconsistent contact resistance.

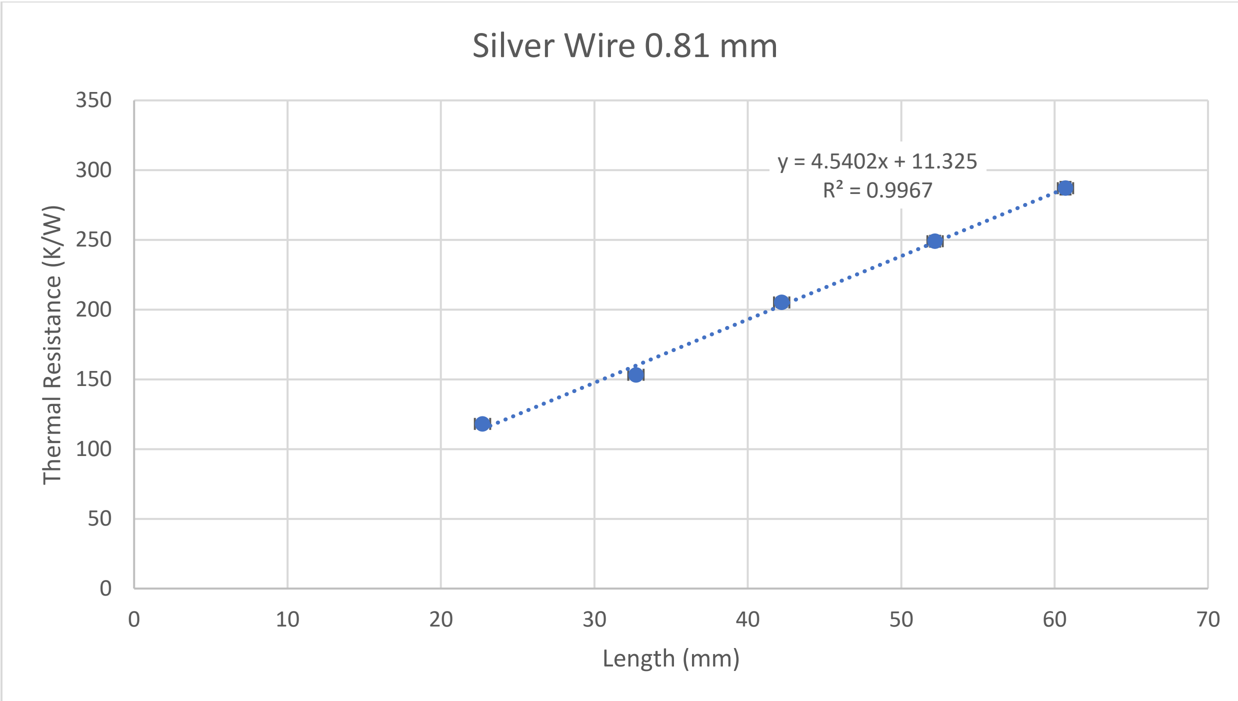

Figure 4-17: Measured thermal resistance vs length for 0.81 mm diameter silver wire

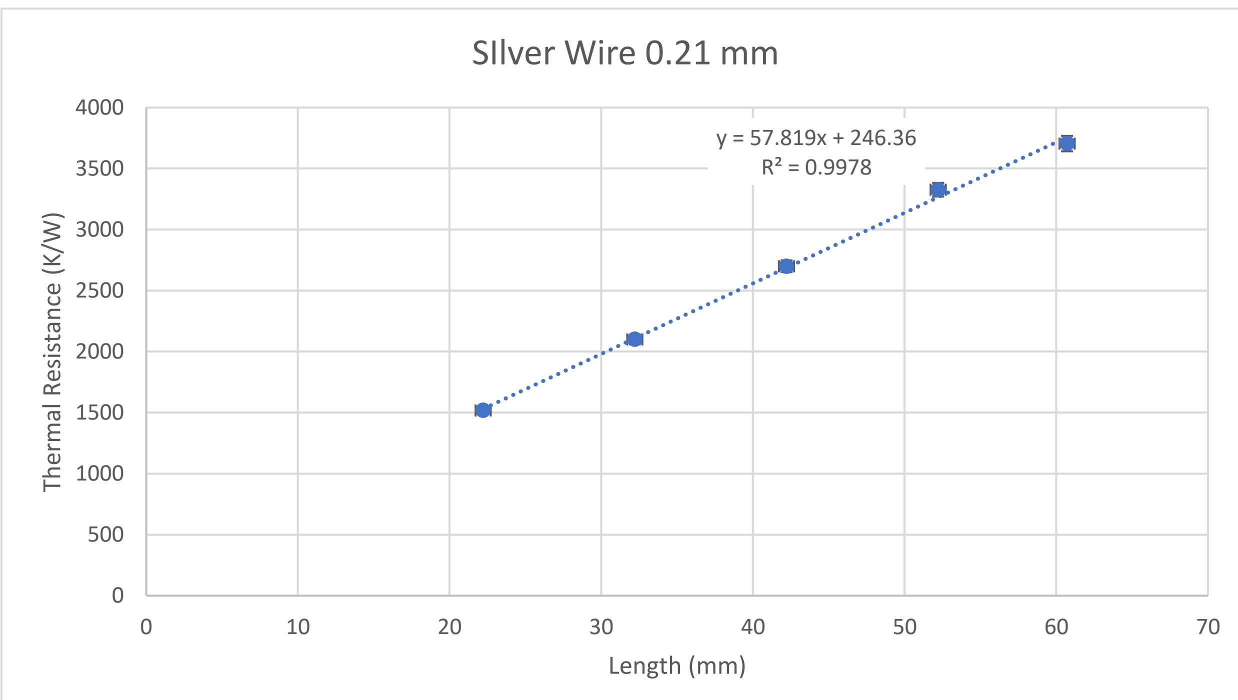

Figure 4-18: Measured thermal resistance vs length for 0.21 mm diameter silver wire

When measuring the K13D2U tow, the fiber tows were handled carefully to prevent fiber breakage and misalignment within the tow. The measurement process was the same as before, where the tow cross-sectional area was first determined through mass, length and density. The calculated cross-sectional area between at least 10 different lengths of fiber tows remained consistently within a 3% margin of each other. The cold block temperature was kept steady at 25 C and the test is run until steady state. A single fiber tow of roughly 70 mm length was cut from the spool and clamped as is, with a rectangular cross-section. The radiation shields served as a guide for the specific length of fiber tow to be left exposed and later measured with a ruler. The same fiber tow is used for the set of tests ranging from 20 – 60 mm.

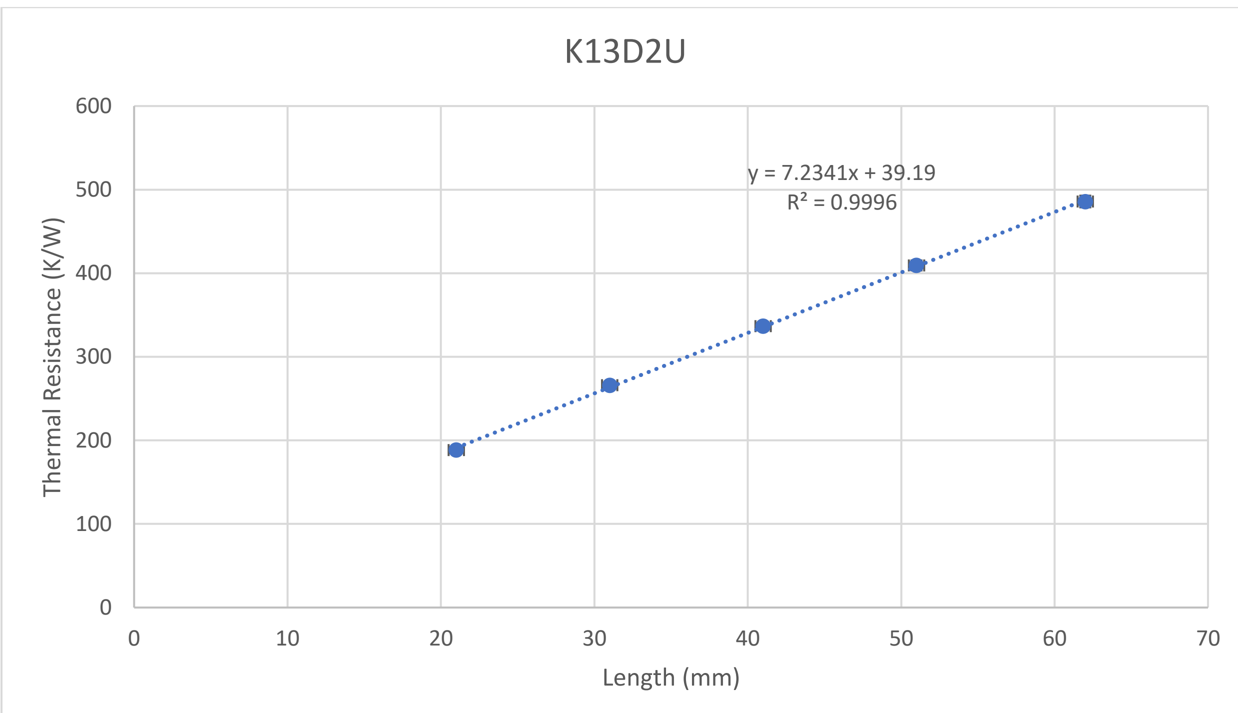

Figure 4-19: Measured thermal resistance vs length of uncoated K13D2U tow

The results are show in Figure 4-19, indicating a linear relationship between thermal resistance and length of the fiber tows. Several tests were performed, refining the measurement process to achieve this linear relationship, ensuring accurate measurements. Three tests were chosen, and the results are listed in Table 4-4, where the thermal conductivity of the K13D2U fiber tow is at worst measured at 768 ± 111 W/mK and at best measured at 792 ± 86 W/mK. This is in good agreement with the manufacturer specified 800 W/mK and will serve as a baseline for any new measurement conducted with PLA coating, 3D printed rasters and composites, to help indicate which process causes the most fiber breakage. Additionally, as seen in simulations, the measured thermal conductivity is expected to be slightly lower due to the primary heater block's thermal conductivity being much lower than K13D2U. However, given the manufacturer specified thermal conductivity has no uncertainty, it's possible the fiber tow could have a higher or lower than expected thermal conductivity. Based on the validation tests, the measured thermal conductivity also tends to overestimate when the sample is thinner due to contact resistance. Additional tests and improvements to the apparatus in the future could lead to a lower uncertainty and higher accuracy.

Table 4-4: Measured thermal conductivity of metal wires and K13D2U fiber

Material	Expected Thermal Conductivity (W/mK)	Measured Thermal Conductivity (W/mK)	Uncertainty (W/mK)	Error (%)
Copper with Kapton	388 – 400 (0.81 mm)	418	38	4.5 - 7.7
Silver Wire	430 (0.81 mm)	427	51	0.47
	430 (0.21 mm)	481	59	12.2
K13D2U	800	768	111	4.03
		792	86	1.04
		775	79	3.14

Chapter 5 Continuous Fiber 3D Printing Process Improvement

The third research objective is to develop methods for mitigating fiber breakage during both the coating and printing processes. The chapter includes methods developed by Olcun and new methods developed in this research, both of which are compared. With the CPCF tow thermal characterization apparatus established and the thermal conductivity of the K13D2U tow measured, Olcun's CPCF coating method was re-evaluated. Due to the limitations in Olcun's apparatus, careful retesting of coated and uncoated fibers was required to reliably reassess fiber breakage during the coating process. In Olcun's tests, the PLA coating on fiber ends was melted off to minimize thermal contact resistance between the heating clamp and fiber, as PLA's low thermal conductivity significantly increases contact resistance. High contact resistance, relative to the sample's thermal resistance, can distort measurements by disproportionately affecting the slope of the total thermal resistance vs. length plot. Moreover, PLA's inconsistent contribution to contact resistance across different sample lengths introduces non-linearity, complicating the extrapolation of thermal resistance and leading to high uncertainty and inaccurate thermal conductivity measurements. This effect is evident in the plot shown in Figure 5-1, where multiple measurements were performed, resulting in a highly non-linear thermal resistance versus length relationship and significantly varying slopes between trials.

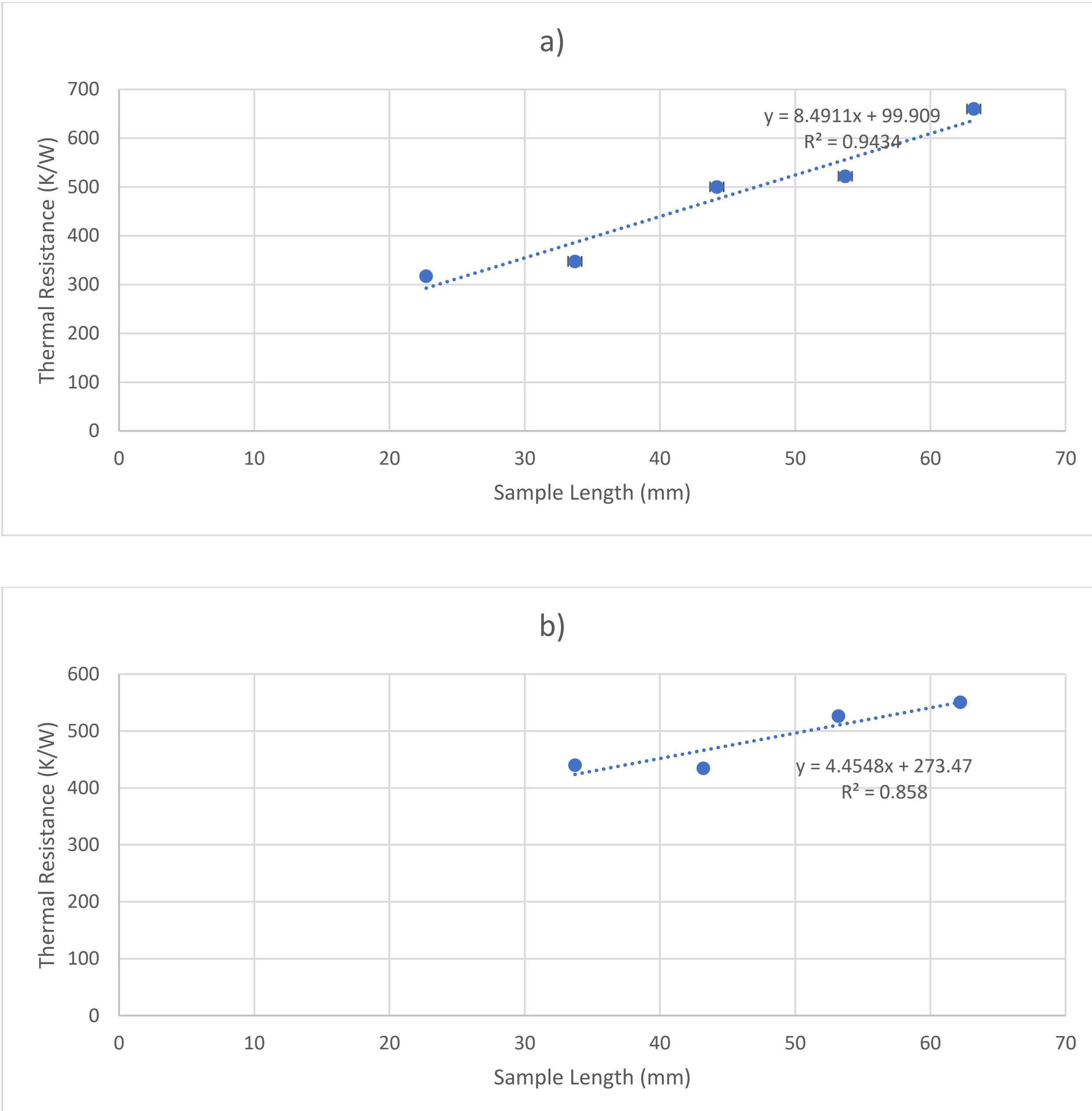

Figure 5-1: Measured thermal resistance versus length plot for Olcun's PLA-coated K13D2U tows: (a) Trial one with PLA coating melted off the ends; (b) Trial two with the same process as trial one.

The significant discrepancies in thermal resistance measurements can also be attributed to fiber breakage during the PLA melting and removal process. PLA was melted off the coated CPCF using a soldering iron with a knife tip, modified to be smooth with its edge rounded to minimize damage while scraping away the molten PLA. The coated fibers were laid on a thin stainless-steel sheet to prevent the PLA from adhering and to allow the fibers to be gently peeled away. However, uneven heating of the PLA during the melting process could result in microscopic regions within the PLA melt remaining colder and harder. These cooler regions could cling more tightly to the fibers, pulling away bits of individual strands when the melted PLA is removed, further contributing to inaccuracies in the subsequent thermal resistance measurements. Additionally, it is impossible to remove all molten PLA from the coated CPCF, specifically between the individual fibers within the tow. This is important since it contributes to significant and inconsistent contact resistance when measuring each length of coated CPCF.

5.1 Fiber Coating

The previous coating method by Olcun oversaturates the CPCF tows with PLA, leading to difficulty in thermal conductivity measurement and overcrowding fibers during composite printing. A new coating method was developed to ensure that the coated CPCF tows are compact with a consistent diameter. A custom nozzle was designed, with a steep 10° throat shown in Figure 5. The steep angle is expected to prevent fiber buckling within the nozzle as they are pulled through molten PLA within the hot end and nozzle. With typical throat angles found in most commercially available 3D printer nozzles, the throat angle and surface roughness often lead to fiber buckling, especially when the tow is first inserted into the nozzle. Additionally, with enough pressure built up within the nozzle, the excess molten PLA in the throat of the nozzle also leads to fiber splitting and buckling.

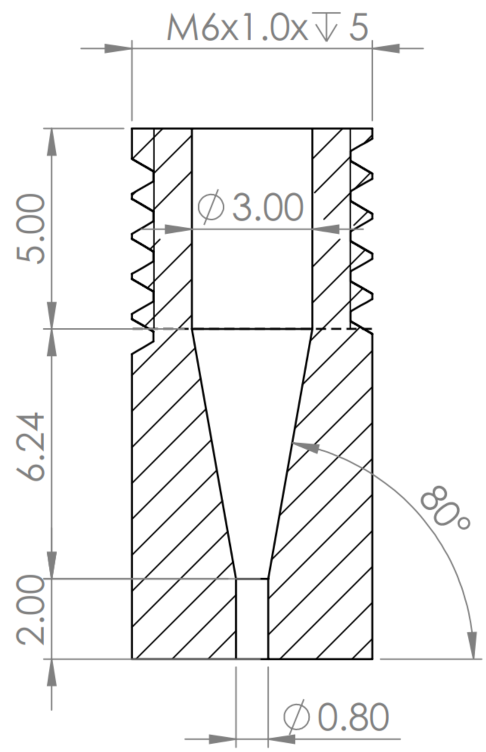

Figure 5-2: CPCF coating nozzle cross-section

With this new nozzle design, a custom hot end was also developed to coat CPCF tows with 1.75 mm PLA filament rather than pellets or other means. Given the commercial availability and cost of filament rolls, this method allows for a much easier transition into testing with other materials used in 3D printing in the future. The custom hot end design is like a typical hot end found in most 3D printers, aside from the internal design of the hot end, nozzle and fiber guides used to funnel the CPCF tows through without breakage. The fiber guides, as shown in Figure 5-2, are composed of a 1.6 mm internal diameter stainless-steel dispenser needle and a custom-machined brass funnel with a 30° angle. The brass funnel is inserted into the dispenser needle to help guide the CPCF tow into the dispenser, which is inserted into the hot end, sitting partially within the nozzle. As the CPCF tow is fed through the guides and nozzle, molten PLA surrounds the CPCF tow in a small section of the nozzle just before the exit. This encases the CPCF tow in a thin layer of PLA, resulting in a rigid 0.8 mm diameter filament of PLA-coated

CPCF tow. The heatsink/fan and heat break are used to prevent the PLA filament from becoming soft before reaching the hot end and causing a blockage due to heat creep. Due to the thin layer of PLA and the high thermal conductivity of the K13D2U CPCF tow, cooling is not required at the exit of the nozzle, as the composite filament cools quite fast by itself. Initial insertion of the CPCF tow was challenging, as the dry fibers tend to separate and fray. To address this, the tow was wetted with water, which helped keep the fibers bundled together through capillary adhesion between adjacent filaments. Additionally, the end of the tow was tightly bundled using a 35 µm copper wire to provide rigidity, to help facilitate the initial insertion through the fiber guide and nozzle.

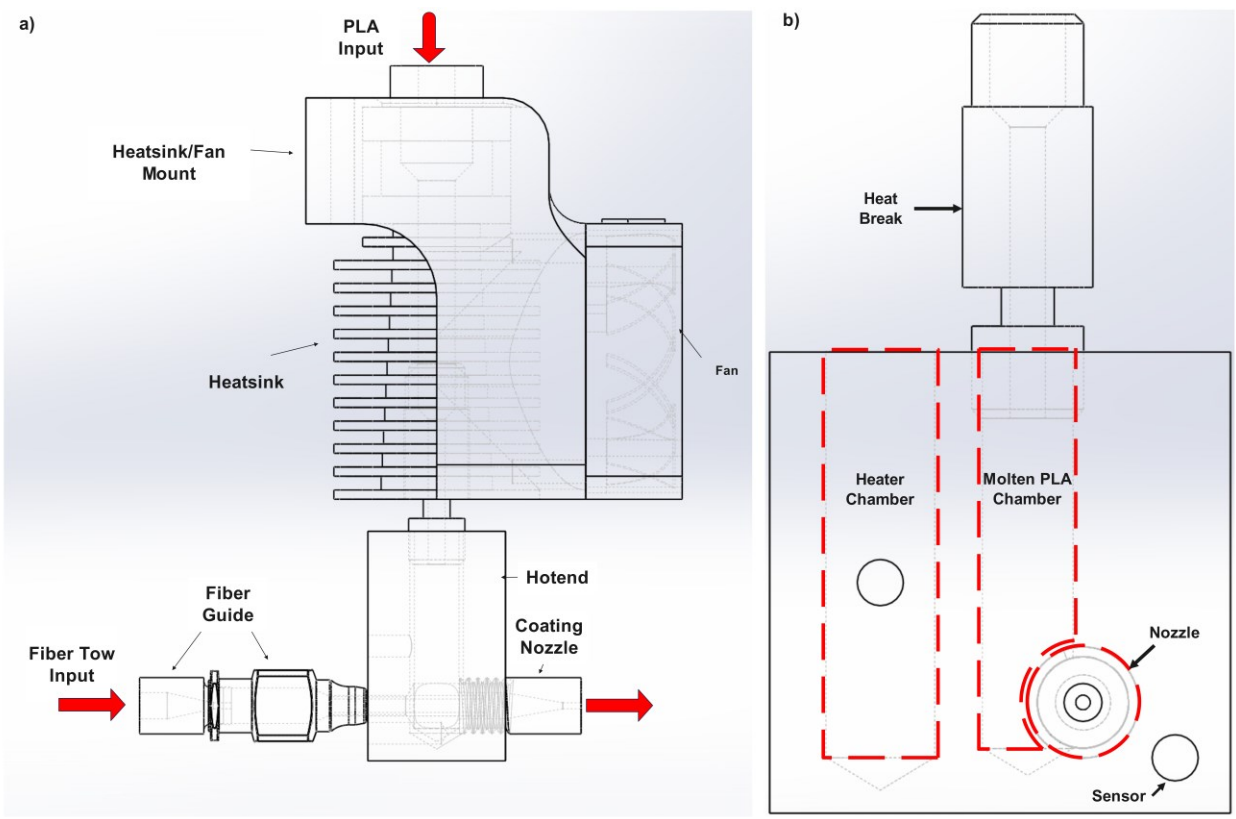

Figure 5-2: CPCF coating apparatus: full assembly side view (a) and hot end front view (b)

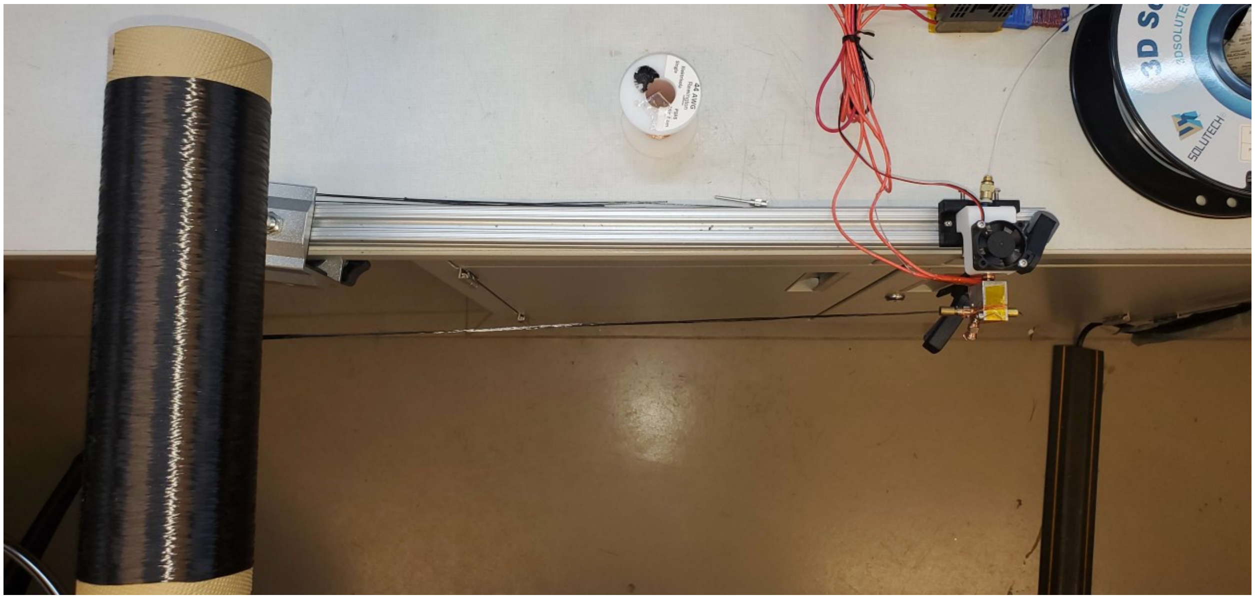

Figure 5-3: Top-down view of fiber coating apparatus

Several filaments of coated CPCF were produced at lengths of approximately one meter. Due to the inherent brittleness of CPCF and the added rigidity from the PLA coating, spooling these filaments proved impractical. The most effective method for handling coated CPCF filaments was to store and print them in a straight configuration, minimizing the risk of fiber breakage and preserving continuity. During the coating process, it became evident that while K13D2U fiber spools are mostly continuous, they contain occasional discontinuities. To assist in feeding the fibers through the hot end, water was used to wet the fibers, as previously described. However, these random discontinuities introduce variation in the coated CPCF filaments, leading to localized sections of lower-than-expected thermal conductivity.

When measuring the thermal conductivity of coated CPCF, the cross-sectional area of the uncoated K13D2U tow previously measured in Section 3.2.2 was used. A single 80 mm long coated CPCF filament was prepared and incrementally cut down to obtain measurements at multiple lengths. Initially, the ends of each sample were melted flat to reduce contact resistance. However, this approach reduced fiber integrity, proven by a nonlinear thermal resistance vs. length relationship. In contrast, measurements taken without melting the ends resulted in a highly linear thermal resistance vs. length plot, indicating consistent contact resistance. This consistency can be attributed to the new method of coating, which encapsulates the CPCF tow rather than mixing with the fibers. While the extrusion of CPCF through molten PLA was done by manually pulling by hand, it resulted in a consistent diameter with a thin layer of PLA over the CPCF tow. The results will likely differ when a larger range of sample length is measured since there are greater chances of variability in PLA coating thickness due to the manual process.

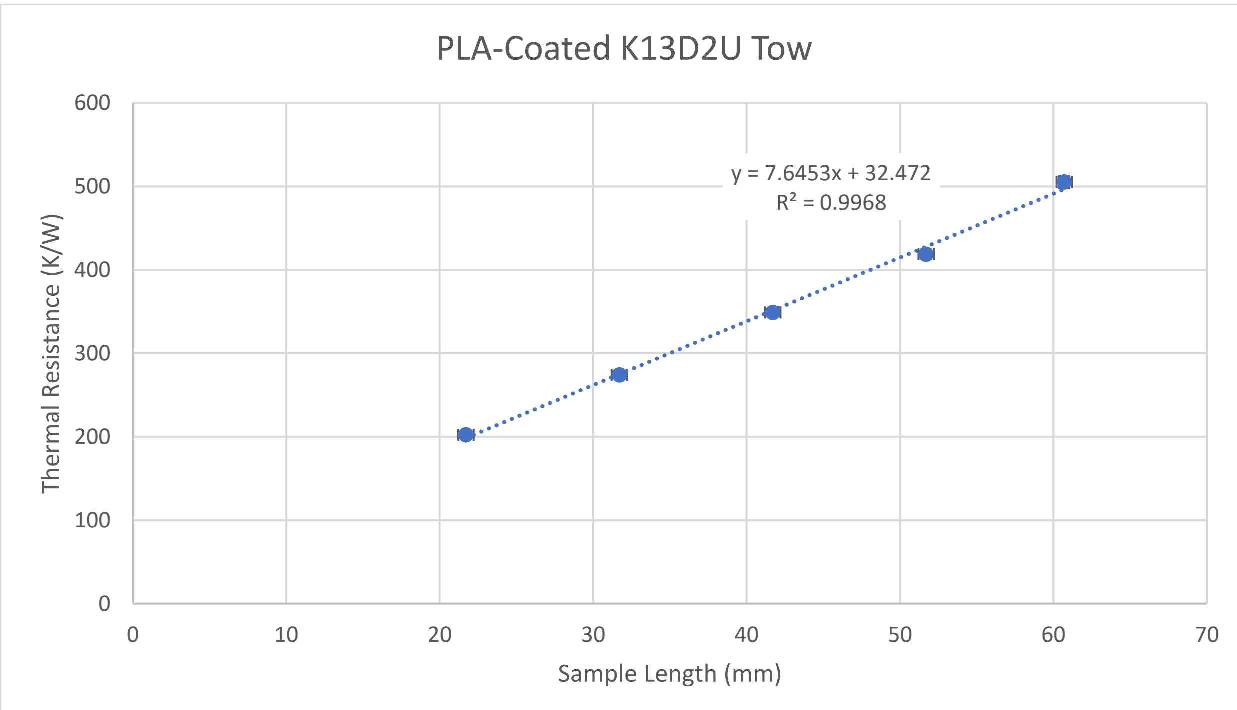

Figure 5-4: Measured thermal resistance vs length for K13D2U coated with PLA using a new process

The measurements conducted for both the new coating method and Olcun's coated tows are listed below in Table 5-1. The results indicate a clear discrepancy between the two methods, largely due to excess PLA and the need to melt the ends when measuring Olcun's coated tows. It remains unclear whether Olcun's coating method causes significant fiber breakage, as there is no consistent way to prepare or measure those coated tows. However, the new coating method shows good agreement with the expected thermal conductivity, particularly with the measured thermal conductivity of the uncoated K13D2U tow. Additionally, the new coating method maintains a consistent and small diameter for the coated tow, which could significantly improve the printing process in later stages of the research. Although the new coating method is effective, it is currently labor-intensive and would benefit greatly from automation to improve filament consistency and efficiency. Automating the process would also help ensure uniform PLA thickness along the length of the CPCF tows. While this uniformity may not significantly affect thermal conductivity measurements, it may be beneficial for maintaining tight tolerances when 3D printing.

Table 5-1: Measured thermal conductivity of Olcun's PLA coated K13D2U tow and the new method of coating

Sample	**Expected Thermal Conductivity (W/mK)**	**Measured Thermal Conductivity (W/mK)**		**Uncertainty (W/mK)**	**Error (%)**
PLA coated K13D2U (Olcun)	800	Trial 1	660	223	17.5
		Trial 2	1258	860	57.3
PLA coated K13D2U (new method)	800	Trial 1	713	108	10.9
		Trial 2	733	105	8.35

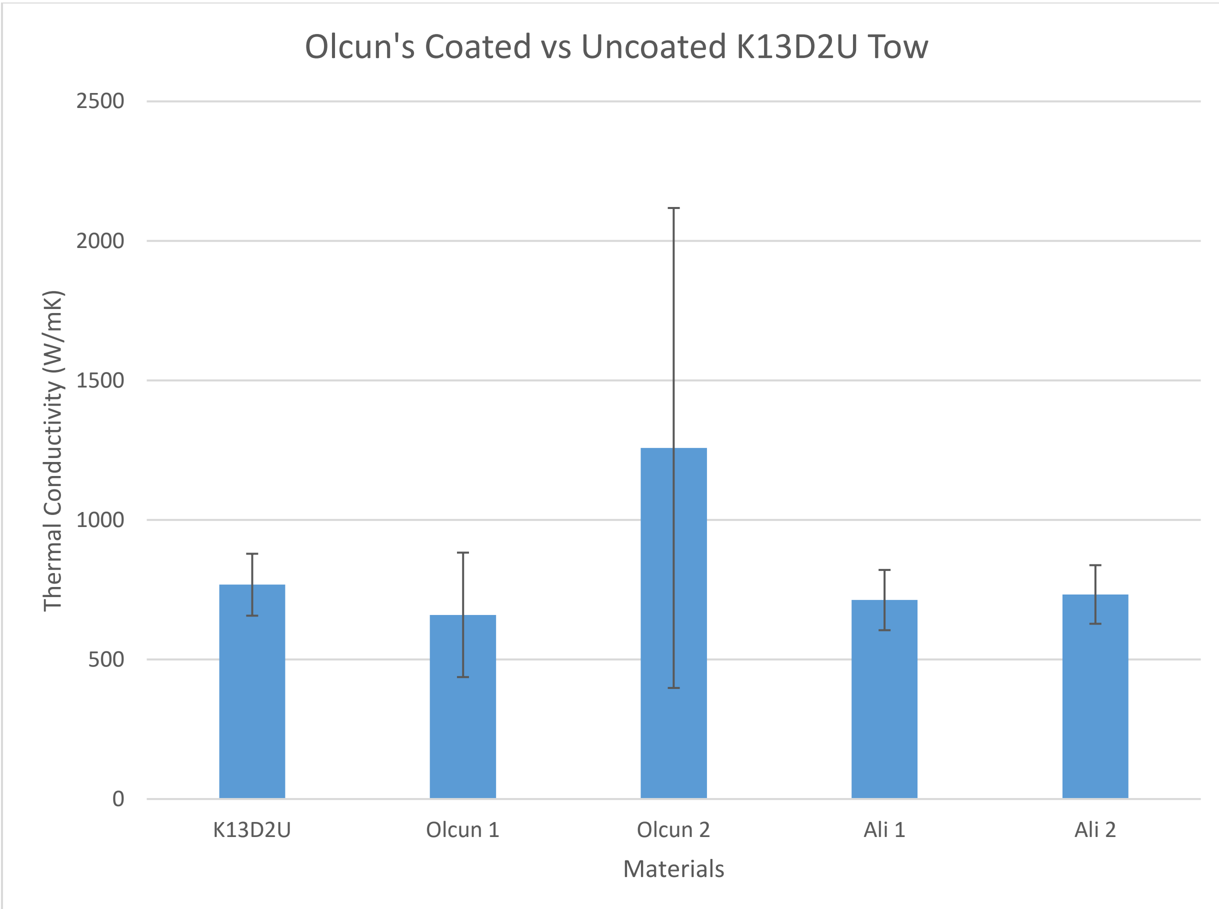

Figure 5-5: Measured thermal conductivity of K13D2U, two tested samples of coated K13D2U tows by Olcun and two tested samples of coated K13D2U tows using the new coating process (Ali 1 and 2)

5.2 Extruder Design

The extruder is one of the most critical components of any 3D printer, allowing precision filament control and deposition. Generally, commercial 3D printers consist of a drive system, hot end, and cooling system. The drive system typically includes a stepper motor, drive gear, idler, and filament guide to precisely control the feed rate of the filament through the hot end. The hot end is usually made of a thermally conductive metal, such as copper or aluminum, and is designed to house a heater cartridge and temperature sensor for accurate temperature control. It also includes a nozzle for filament output and a heat break that connects to the heat sink and drive system, providing a controlled pathway for the filament. Finally, the heat sink dissipates heat from the upper section of the extruder, preventing heat creep and ensuring the filament remains solid until it reaches the melting zone in the hot end. The stepper motor, heater temperature, and the position of the extruder/nozzle are all controlled by a controller board. The filament feed rate, the XYZ position of the extruder/nozzle, and print speed are sequentially managed by the controller board through a slicer, which generates the necessary G-code commands in a G-code file. This allows the ability to 3D print various geometries using various materials. However, when it comes to certain materials such as custom PLA coated CPCFs which don’t follow the same structural integrity of typical 3D printer filaments, a design change is required to be able to print with.

In his research, Olcun designed a custom extruder capable of printing with both PLA filaments and coated CPCF filaments simultaneously. The extruder and its components are highlighted in Figure 5-6. A single hot end block was extended to include a secondary nozzle at a 45° angle, along with a secondary heat sink and a secondary drive system, enabling the deposition of coated CPCF alongside PLA to create a composite. The 45° angle was crucial to the design—without it, the coated CPCF was prone to bending or buckling at perpendicular or steeper angles, which significantly reduced the thermal conductivity of the 3D-printed composite. Due to design limitations, Olcun was initially unable to achieve printing angles shallower than 45°, which would have further reduced CPCF fiber breakage. Later in his research, he transitioned to using a robotic arm and a redesigned extruder to enable printing at angles as shallow as 30° from the build plate. However, this extruder was not capable of printing with PLA and CPCF filaments simultaneously. When comparing the measured thermal conductivity of the coated CPCF at different printing angles, the thermal conductivity improved by about 24% going from a 45° printing angle to a 30° printing angle. This demonstrates a clear dependence of thermal conductivity on the printing angle of the coated CPCF.

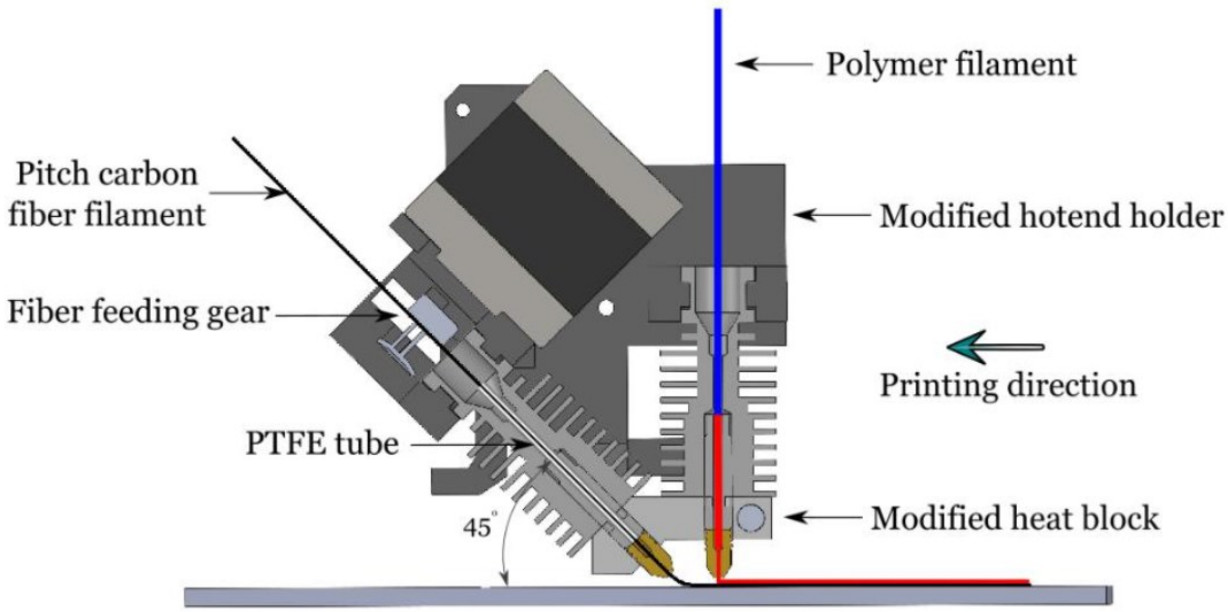

Figure 5-6: Diagram by Olcun of his custom extruder for 3D printing composites using the Prusa I3 MK2

To improve the results achieved by Olcun with printed CPCF filaments, the extruder was redesigned to enable shallower printing angles and incorporate a different deposition method, aimed at reducing fiber breakage. Upon assessing Olcun's design, it became evident that, beyond the limited printing angles, the nozzle geometry likely contributed significantly to fiber damage. In his setup, the coated CPCF filaments were required to rest just before the nozzle tip to prevent premature melting. Deposition was achieved by pressing the coated CPCF with the nozzle itself, melting the PLA coating upon contact and causing it to adhere to the build plate or a layer of PLA/CPCF. This method likely induced excessive mechanical stress on the filament, contributing to fiber breakage and reduced thermal performance. Additionally, a poor surface quality of the nozzle inner walls might also have led to fibers buckling as they are deposited. The cutting mechanism was described as a "whipsaw" motion, where the nozzle rapidly moves against the printing direction and then towards it, causing the brittle fibers to snap. While this method appeared effective for the brittle K13D2U, it posed a risk: if some fiber strands within the filament did not break cleanly, they could be pulled instead, potentially dragging adjacent fibers with them. This could disrupt the continuity of the deposited CPCF filament, compromising both structural integrity and thermal performance. Olcun also mentions the method to be ineffective for the lesser brittle K1392U and K1352U samples, as the fibers occasionally do not break cleanly. Thus, it is likely that the best approach to printing with CPCFs is to employ a cutting mechanism for optimal results.

To keep the extruder design simple yet effective, the new setup followed a similar structure to the base Prusa i3 MK2 3D printer extruder and utilized the same dual extrusion controls that Olcun had implemented. The Prusa i3 MK2 can control up to four stepper motors through a stepper multiplexing board developed by Prusa. However, while this board supports four separate stepper motors, it cannot drive them simultaneously. As a result, it was not possible to extrude both CPCF and PLA filaments at the same time. This limitation was not critical for the current research, though the ability to co-extrude CPCF and PLA could offer opportunities for customization in printing. Additionally, the printer's control board supported only a single hot end, which constrained the extruder design to a singular hot end shared by both filaments. Although these limitations could be overcome by upgrading to a different control board, the primary objective of reducing fiber breakage by improving the printing process, was achieved using the current system. The two most significant modifications made were to the CPCF nozzle and the CPCF extruder stepper motor, which enabled extremely shallow printing angles down to 10°, as well as the integration of a pressing and cutting mechanism for CPCF deposition.

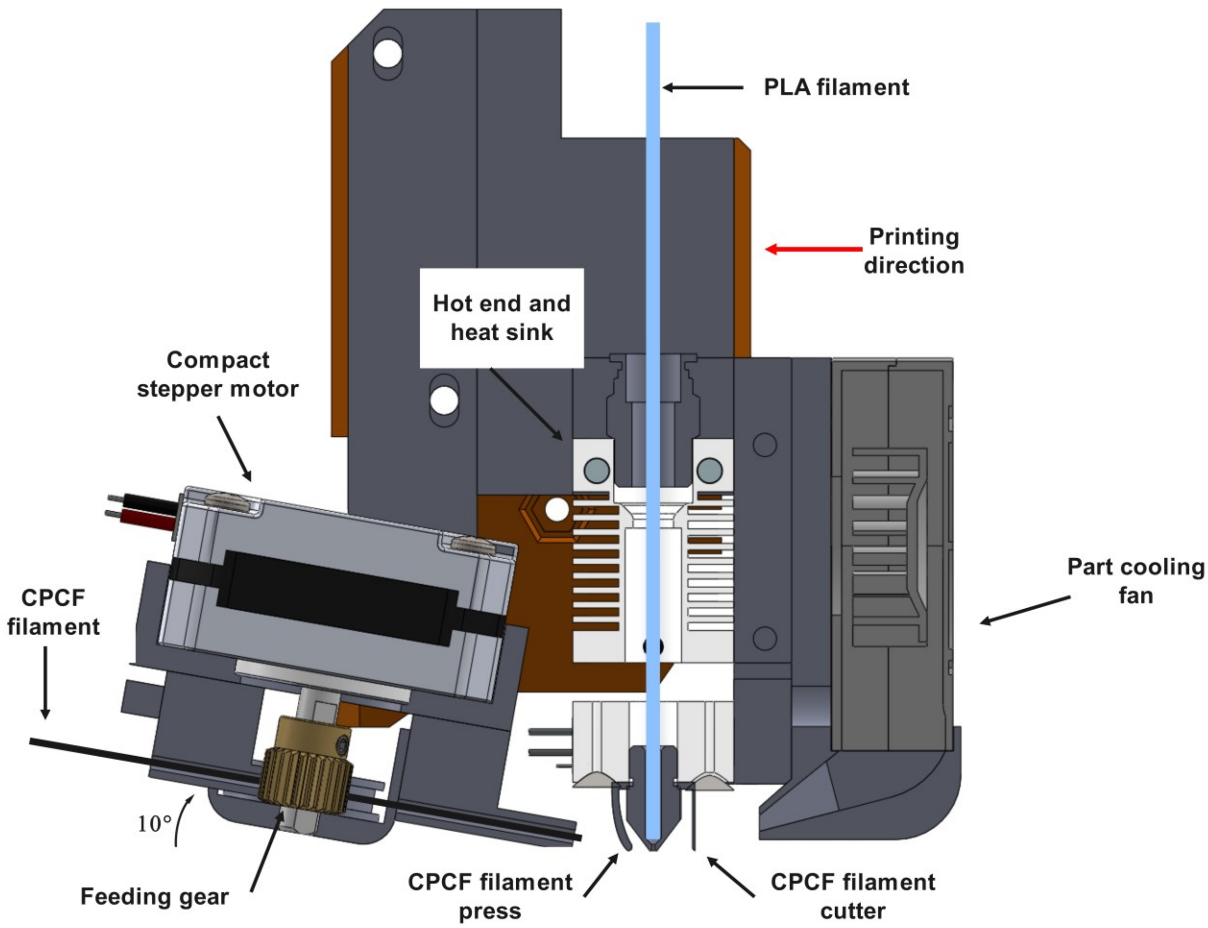

Figure 5-7: New extruder design for CPCF composite printing

The new extruder design, as shown in Figure 5-7, incorporated a low-profile pancake stepper motor to extrude the CPCF filament. This compact motor allowed the extruder to be positioned much closer to the hot end and heat sink assembly, enabling a wider range of printing angles. In contrast, Olcun's design was constrained by a bulkier stepper motor and a secondary heat sink, leaving little to no space to achieve shallower printing angles. Furthermore, his setup would require a custom hot end to be redesigned and manufactured for each desired printing angle. The new configuration utilizes a single, commercially available hot end with a slight modification: a shaped copper strip was used as an addon to the nozzle, serving as both a hot press and a cutting tool for the extruded CPCF filament. Additionally, a part cooling fan was integrated into the system, to allow for faster print speeds by rapidly cooling the molten PLA and CPCF material after deposition.

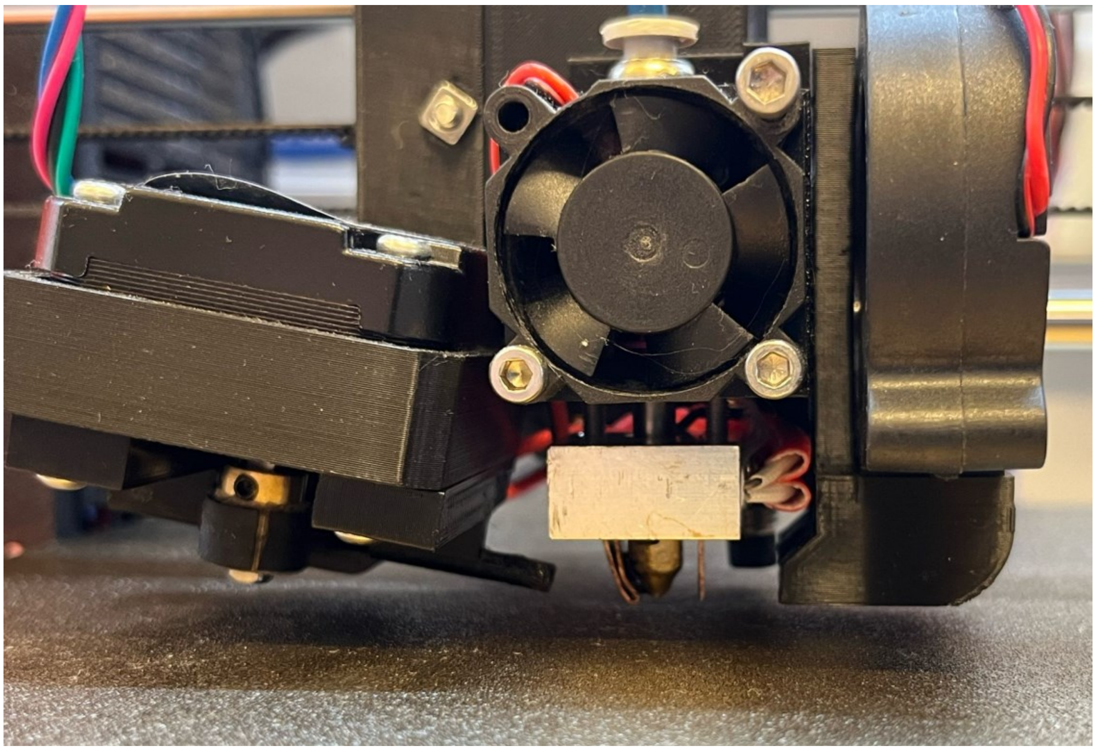

Figure 5-8: Image of the new extruder setup for CPCF 3D printing

The printing angle of the new extruder design could have been made modular, though this was deemed unnecessary, as an angle of 10° proved sufficient to eliminate nearly all fiber breakage when using the hot press and cutting mechanism. One of the primary challenges with the new setup was the precise placement of the cutter to ensure clean cuts during printing. Considerable time was spent adjusting the cutter’s height to prevent it from scraping the CPCF filament. The final solution was to position the cutter approximately 0.2 mm higher than the nozzle tip, which effectively prevented unwanted contact with the filament. At this height, the cutter cannot sever the CPCF filament unless there is a base layer of PLA at least 0.2 mm thick. This allows the nozzle to travel an additional 0.2 mm without crashing into the build plate, enabling the cutter to function properly. An additional challenge arose later with the hot press. The hot press would occasionally drag over the deposited CPCF filaments and unintentionally pull it during subsequent passes due to its width. These issues could be addressed in future iterations through a more calibrated design with tighter tolerances or potentially by redesigning the system to include a motorized cutter and a custom hot press specifically engineered to work together with the nozzle. Given the nature and complexity of the interactions between the CPCF, PLA, heat and other aspects of the extruder, there are numerous alterations possible to achieve smoother printing.

5.3 CPCF 3D Printed Rasters

Thermal conductivity tests were performed on single 3D-printed CPCF rasters using the developed extruder for the Prusa i3. A printing speed of 800 mm/min was selected as the baseline for these tests, informed by the work of Olcun, who reported that for K13D2U fibers, measured thermal conductivity declined significantly when printing speeds exceeded approximately 2500 mm/min. In his study, the temperature profile of the deposited CPCF filament showed a reduction of approximately 40 °C within three seconds after deposition, with microscopy revealing consistent fiber breakage occurring at a location approximately 60 mm along the raster length. No additional visible fiber breakage was observed when comparing samples printed at 800 mm/min and 3000 mm/min, though it was suggested that longer raster lengths may be necessary to determine the cumulative effects of extended printing on fiber integrity. Based on these findings, a conservative printing speed of 800 mm/min was adopted to minimize the risk of breakage while maintaining process stability.

Initial attempts to print continuous CPCF rasters with the new extruder were unsuccessful due to a fundamental geometric constraint: the elevated position of the integrated cutter. The cutter had been deliberately positioned high to avoid interference with the build surface, which consequently prevented the proper severing of the CPCF filament at the completion of each printing pass. As a direct result, the separation of deposited CPCF segments had to be performed manually, a process that introduced both additional handling time and the potential for mechanical disturbance of the newly deposited filament.

To effectively address this limitation, a base structure consisting of several layers of PLA rasters was first deposited onto the build plate prior to beginning the CPCF printing process. This initial PLA structure successfully elevated the deposition plane sufficiently to allow the cutter to be safely lowered into an effective operational range, thus enabling it to cleanly sever the CPCF filament without making contact with the underlying build plate. With this adjustment, K13D2U rasters were successfully printed and subsequently tested for thermal conductivity. The resultant comparative data is presented in Table 5-2 , which contrasts K13D2U rasters printed using Olcun's original extruder design and the newly developed design. However, it is important to note that Olcun's coating method produced filaments with inconsistent and significantly larger diameters; therefore, it was not possible to print those specific K13D2U rasters using the newly developed extruder. While the measured thermal conductivity for Olcun's K13D2U rasters appears consistent despite this issue, the uncertainty of the measurement is high due to the presence of excess PLA.

As previously noted during the measurement of coated K13D2U filaments, this residual polymer results in inconsistent thermal contact resistance across the measured length of the sample. This specific trend proved to be repeatable across several K13D2U rasters and coated filaments. The initial 3D-printed raster using the new method also presented a similar level of uncertainty, but it was later attributed to intrinsic inconsistency within the K13D2U tow itself, specifically where certain sections were already broken. Further testing conducted with intact sections of the tow ultimately showed a lower and more acceptable uncertainty that is fully consistent with the values measured for both the uncoated and coated K13D2U tow.

Table 5-2: Measured thermal conductivity of 3D printed K13D2U rasters using Olcun's and the newly developed extruder

Sample	Expected Thermal Conductivity (W/mK)	Measured Thermal Conductivity (W/mK)		Uncertainty (W/mK)	Error (%)
PLA coated K13D2U raster (Olcun)	800	Trial 1	802	190	0.27
		Trial 2	799	171	0.09
PLA coated K13D2U raster (new method)	800	Trial 1	848	184	5.94
		Trial 2	787	102	1.64

Ultimately, given the similarity in the measured thermal conductivities, conducting several measurements might show a better picture of whether there is a noticeable difference in the two methods. The samples printed using Olcun's 3D printer design were limited due to a challenge encountered when printing. Olcun used an altered brass nozzle specifically for 3D printing K13D2U composites. There was only one of these nozzles fabricated by Olcun since his work later shifted to robotic arm 3D printing and a newly developed nozzle fitted for that robotic arm specifically. The alterations to the nozzle were also not documented, thus making it impossible to replicate the nozzle. The altered nozzle was also deteriorating from its previous uses by Olcun, which would cause significant clogging and failed prints. Other components of the extruder design were starting to fail, and so only a few samples were printed. During thermal conductivity measurements, initial few samples were used as process improvement to ensure measurement were consistent and repeatable. The same applied to the rasters printed using the new method, and so the first trial had higher uncertainties. After process improvement, the second trial shows the lowest uncertainty in measurement using the new method.

5.4 Summary

In this chapter, a new CPCF coating apparatus was developed, along with a new 3D printer extruder designed for printing coated CPCF. The coating process was manual, requiring the fiber tow and PLA to be fed into the hotend while the coated fiber was pulled from the nozzle at a consistent speed to achieve a thin and uniform coating. Additionally, the feed rate of the PLA was critical, as lower rates resulted in insufficient coating, while higher rates caused PLA to overflow from both the fiber entry point and the nozzle, leading to clogging and fiber breakage. Automating this process in the future would lead to a faster and more consistent coated fiber tow. The coated fibers produced using Olcun's method and the newly developed method were compared through thermal conductivity measurements. The results showed that the oversaturated PLA coating in Olcun's fiber tows led to inconsistent measurements with high uncertainty. In contrast, the new coating process produced fiber tows with a thinner, more uniform PLA layer and improved compaction, resulting in thermal conductivity values that closely matched the expected values.

Olcun's extruder design was limited to a 45° printing angle. In contrast, the newly developed extruder incorporates a compact motor, enabling CPCF printing at angles as low as 10° relative to the build plate, which represents the shallowest achievable angle to help prevent fiber breakage during deposition. Additionally, Olcun's design lacked a mechanism to cut the fiber during direct nozzle deposition, resulting in inconsistent fiber placement and increased breakage. To address this limitation, a combined hot press and cutting mechanism was implemented, in which the PLA coating is locally melted to bond the deposited fiber to the underlying layer while simultaneously cutting the unmelted coated fiber tow. This enables controlled separation of the fiber and allows for more consistent deposition of subsequent layers of PLA and fiber tow. The extruder also incorporates a print cooling fan to rapidly solidify the deposited PLA and coated CPCF, which helps maintain dimensional stability, prevents sagging, and ensures the fibers remain fixed in place during cutting.

To validate the new print angle and hot press/cutter mechanism, several rasters were 3D printed using both the newly designed extruder and Olcun's extruder. Due to deterioration of the custom brass nozzle in Olcun's design, only a limited number of rasters could be produced. Each raster sample was tested by cutting it to a specified length, removing the PLA through melting, and repeating the measurement on the same raster at multiple lengths. The results indicated that, on paper, Olcun's rasters exhibited higher thermal conductivity values; however, given the limited number of trials, it is difficult to draw definitive conclusions regarding performance improvements. It is possible that the tested rasters represent outliers with minimal fiber breakage. Notably, the second trial of the raster produced using the new extruder design demonstrated reduced measurement uncertainty, suggesting improved consistency. Therefore, future work involving a larger sample size is necessary to provide a more reliable assessment of the printing improvements.

Chapter 6 Macroscopic Composites Fabrication and Testing

With an improved and tested fiber coating and printing process, the final objective of this research was to 3D print a full-size composite for comparison with the parallel model. However, the Prusa i3 MK2 3D printer currently lacks the capability of autonomously printing with coated CPCF without a more advanced mainboard. Additionally, the added wide hot press on the nozzle frequently interferes with previously deposited CPCF rasters while the cutting mechanism dulls rapidly due to the abrasive fibers, making prints unreliable. These limitations demonstrate the necessity of a specially designed extruder for successful, full-scale CPCF composite printing. Designing such an extruder is currently outside the scope of this research due to limited time and resources available. Consequently, the focus of the research was pivoted towards manually fabricating K13D2U composites of varying volume fractions and testing them against the parallel model for thermal conductivity, using the newly developed coating process.

6.1 Thermal Characterization

To measure the thermal conductivity of a macro-scaled K13D2U composite, a steady-state guarded-hot-plate technique was used. The apparatus was developed based on the design principles of Elkholy's apparatus (Chapter 4), but several modifications were made to improve repeatability and ease of use for testing multiple samples. The apparatus consists of a primary hot block encapsulated by a secondary, or guard, hot block. The secondary block is temperature-controlled to match the primary block, which minimizes lateral heat loss and ensures a one-dimensional heat flow through the sample.

The sample is positioned between the primary hot block and a primary cold block, as shown in Figure 6-1. The primary cold block is then maintained at a constant temperature using a chiller. Several 1 mm RTD sensors are used to measure the temperature of the hot blocks and cold blocks. Additionally, two RTDs are inserted into 1 mm holes drilled directly into the sample at a distance apart. This technique provides a direct temperature measurement across the sample, bypassing the thermal contact resistance at the sample-block interfaces and significantly reducing thermal conductivity measurement error. The primary hot/cold blocks have a 40 mm by 40 mm cross-section, as such the sample is also required have the same dimensions for accurate results. Ideally, the sample height should be larger than 10 mm, since two 1 mm holes are required for temperature sensors along with sufficient distance between the two holes for lower uncertainties when calculating thermal conductivity.

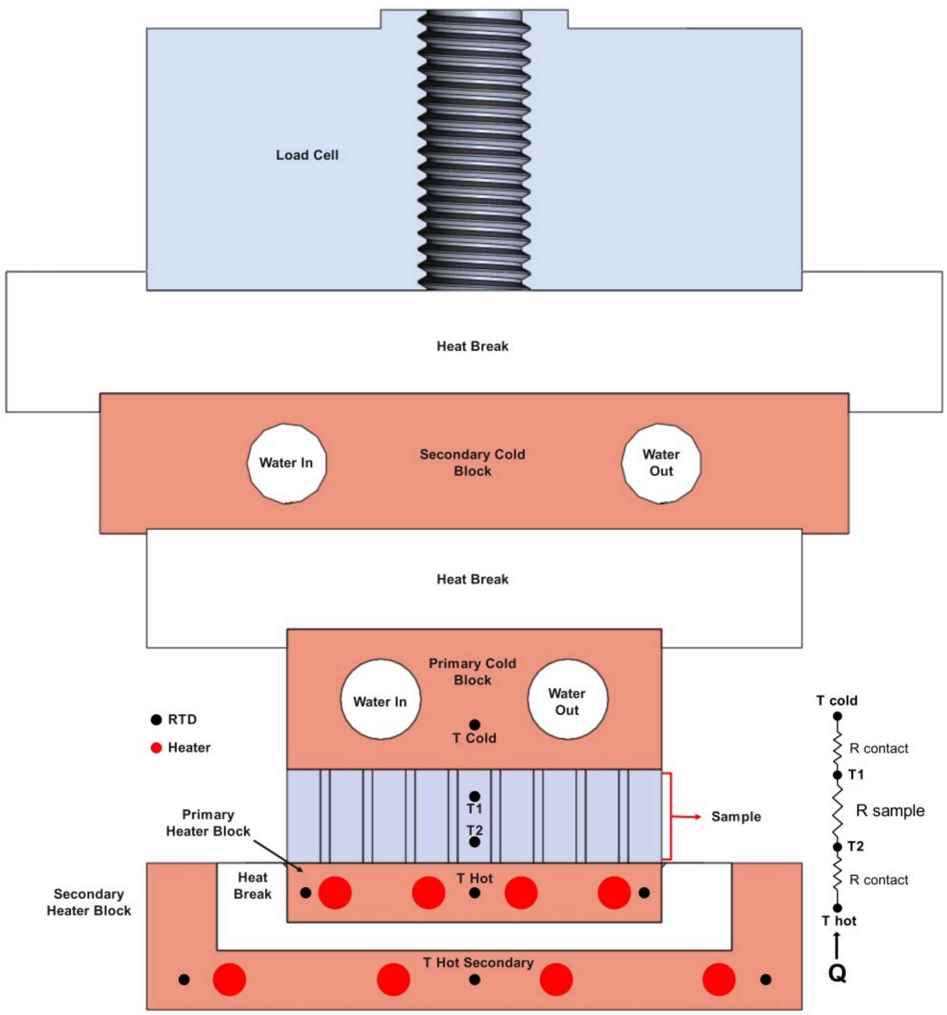

Figure 6-1: Macro thermal conductivity apparatus schematic diagram

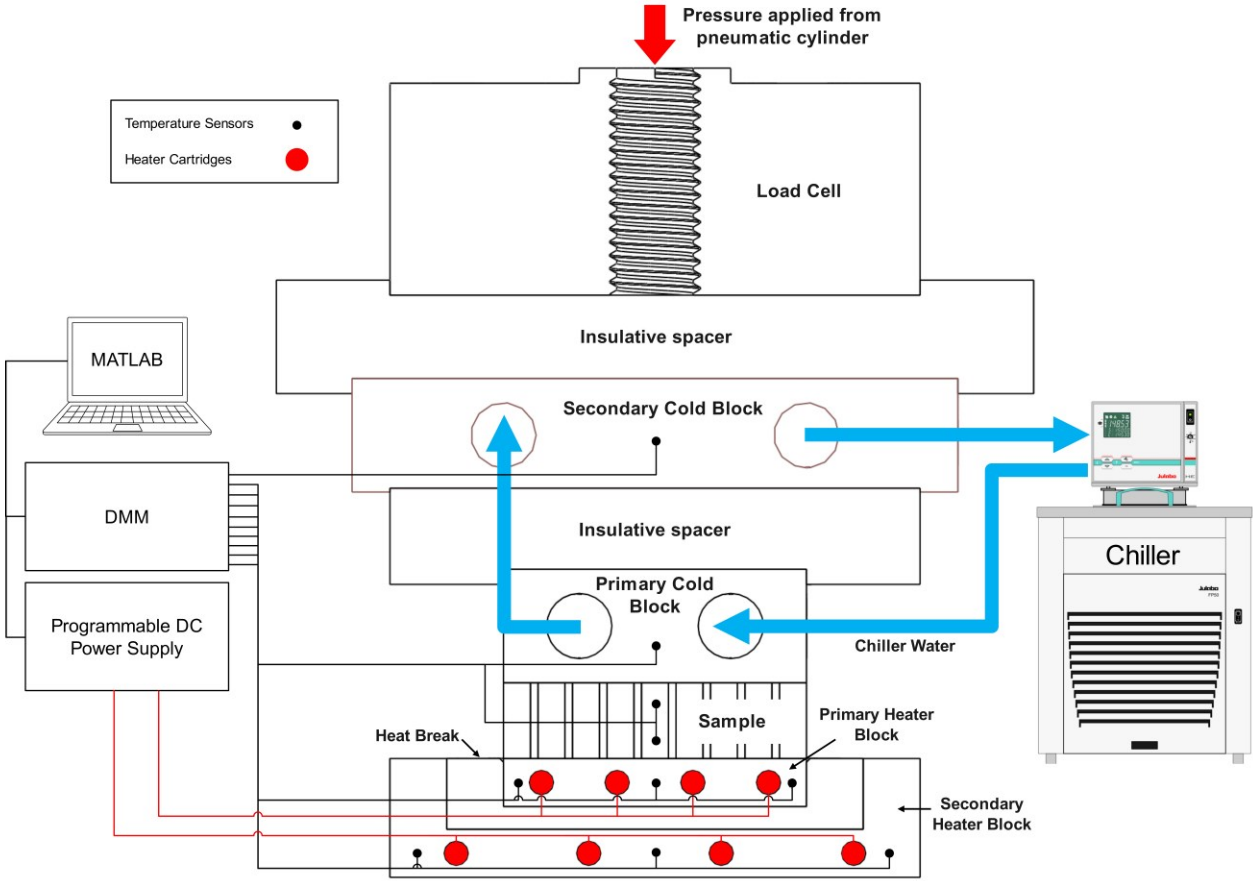

Figure 6-2: Macro thermal conductivity apparatus instrumentations diagram

To minimize thermal contact resistance, the sample must be firmly compressed between the hot and cold blocks. This is accomplished using a pneumatic cylinder (Figure 6-3), which applies constant pressure by pressing the cold block onto the sample against the hot block. The apparatus is equipped with a pressure regulator, a pressure gauge, and a load cell to precisely adjust and measure the applied force. This method ensures high consistency and accuracy across multiple tests by significantly reducing variations in contact resistance among samples. Additionally, two aligners are used to center the sample with the cold and primary hot blocks. The pneumatic cylinder connects to the cold block assembly via a clevis coupling, which provides several degrees of freedom to accommodate sample surfaces that are not perfectly parallel. Nevertheless, smooth and flat sample surfaces are crucial for ensuring optimal thermal contact. Once the sample is prepared and installed, the experiment is controlled and monitored using MATLAB, which manages the chiller and heaters while a Data Acquisition (DAQ) system logs the data. The test concludes once the primary and secondary heater blocks reach a steady-state thermal condition. The data from the test is then used to calculate the thermal conductivity of the sample using the Fourier's law equation:

$$k_{sample} = \frac{QL}{A(T_2 - T_1)}$$ *Equation 6-1*

where, Q is the heater power in watts, L is the distance between the sample RTD sensors in meters, A is the sample cross-sectional area in meters squared T_1 is the temperature of the cold side and T_2 is the temperature of the hot side in Kelvin.

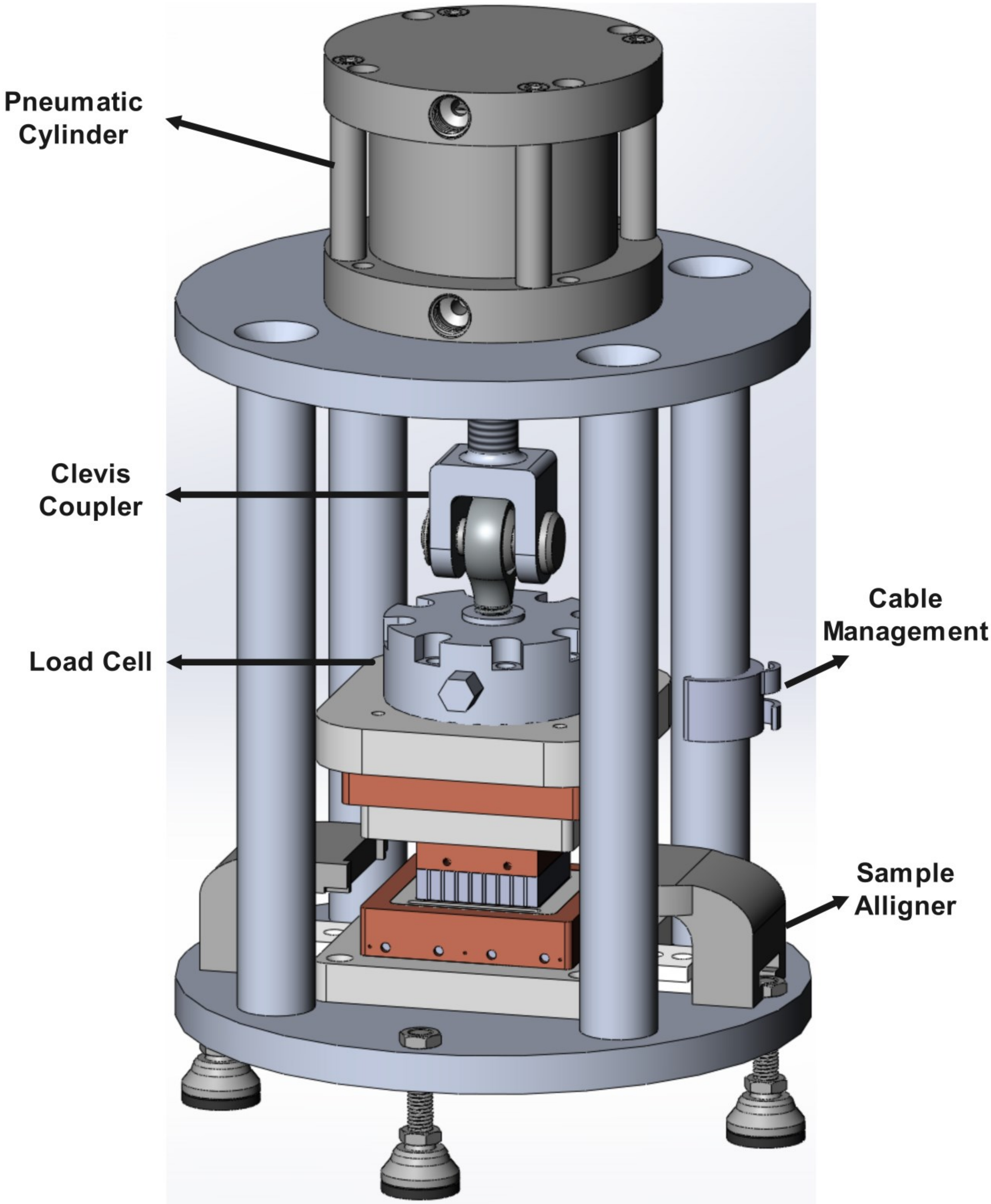

Figure 6-3: Macro thermal conductivity apparatus full-scale CAD model

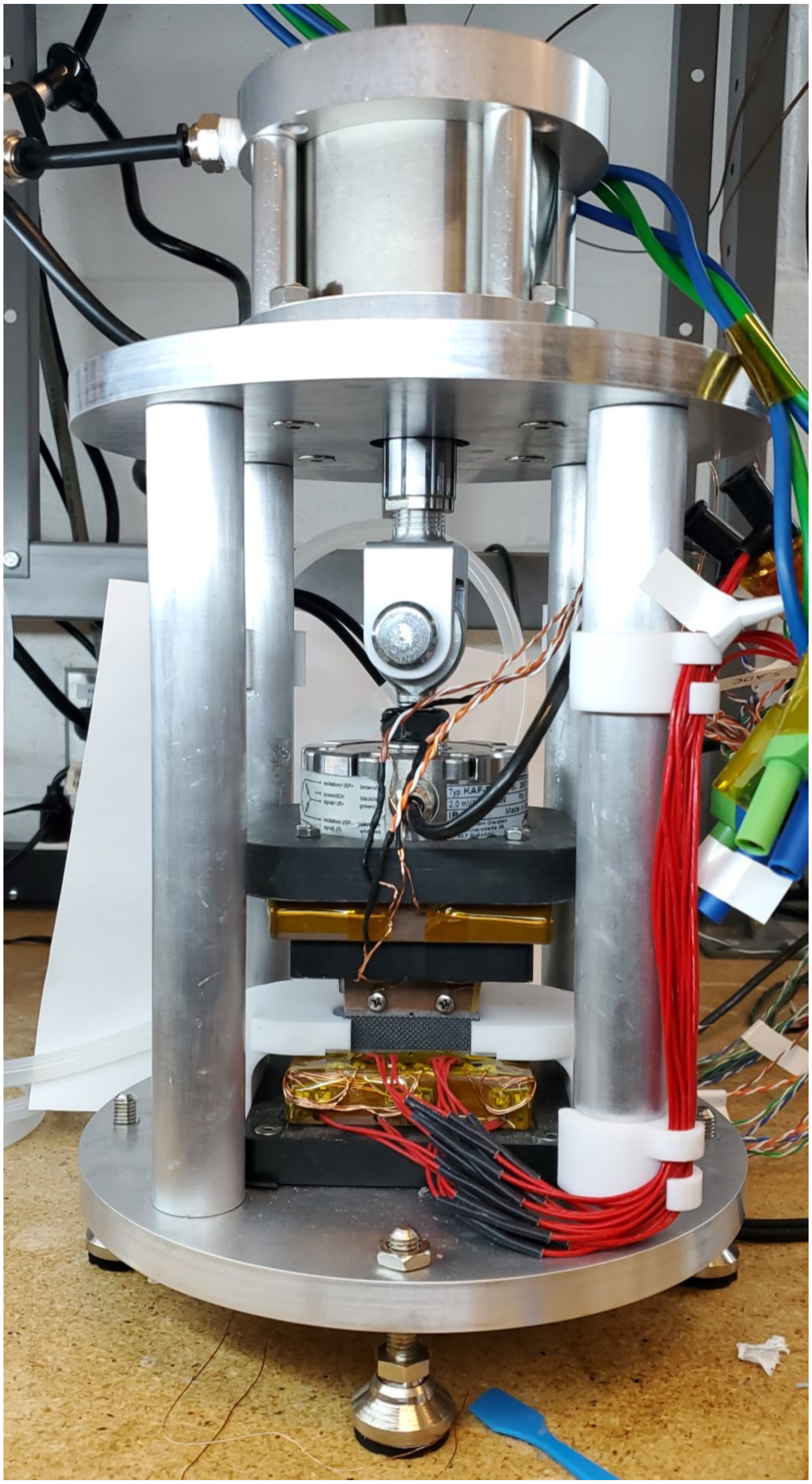

Figure 6-4: Macro thermal conductivity apparatus full-scale image

6.2 Sample Design and Fabrication

The composite was purposely designed to ensure that the CPCF tows were uniformly distributed across the 40 mm by 40 mm cross-section. Uniformity is crucial because the significant difference in the thermal conductivity of K13D2U and PLA would otherwise skew the temperature profile across the composite and result in a lower thermal conductivity measurement. Ibrahim had previously fabricated a K13D2U composite using a "hand-layup" method, as discussed earlier in Chapter 1.1. This was a quick and crude way to check the validity of high thermal conductivity composites using CPCF, and while the results were promising, they indicated a large gap between the predicted thermal conductivity of the composite using the parallel model.

The current method of K13D2U composite fabrication utilizes an in-situ fiber embedding process, where coated K13D2U fibers are manually placed by hand on certain print layers. This is achieved by designing a CAD model of a 40 mm by 40 mm by 11 mm rectangular prism with uniformly distributed square holes across the 40 mm by 40 mm cross-section. These square holes measure 0.8 mm by 0.8 mm, and their total quantity is changed according to the desired fiber volume fraction. For the denser volume fraction configuration, a gap is left in the centerline of the composite to ensure that a 1 mm hole can be drilled later for testing thermal conductivity using the developed apparatus. The CAD model is then sliced in PrusaSlicer, making use of the pause feature readily available in the settings. The print orientation is critical and is shown in Figure 6-5, as printing in this specific orientation keeps the PLA rasters parallel to the fibers, which simplifies the printing process and prevents any PLA overlap with the designed holes during the print.

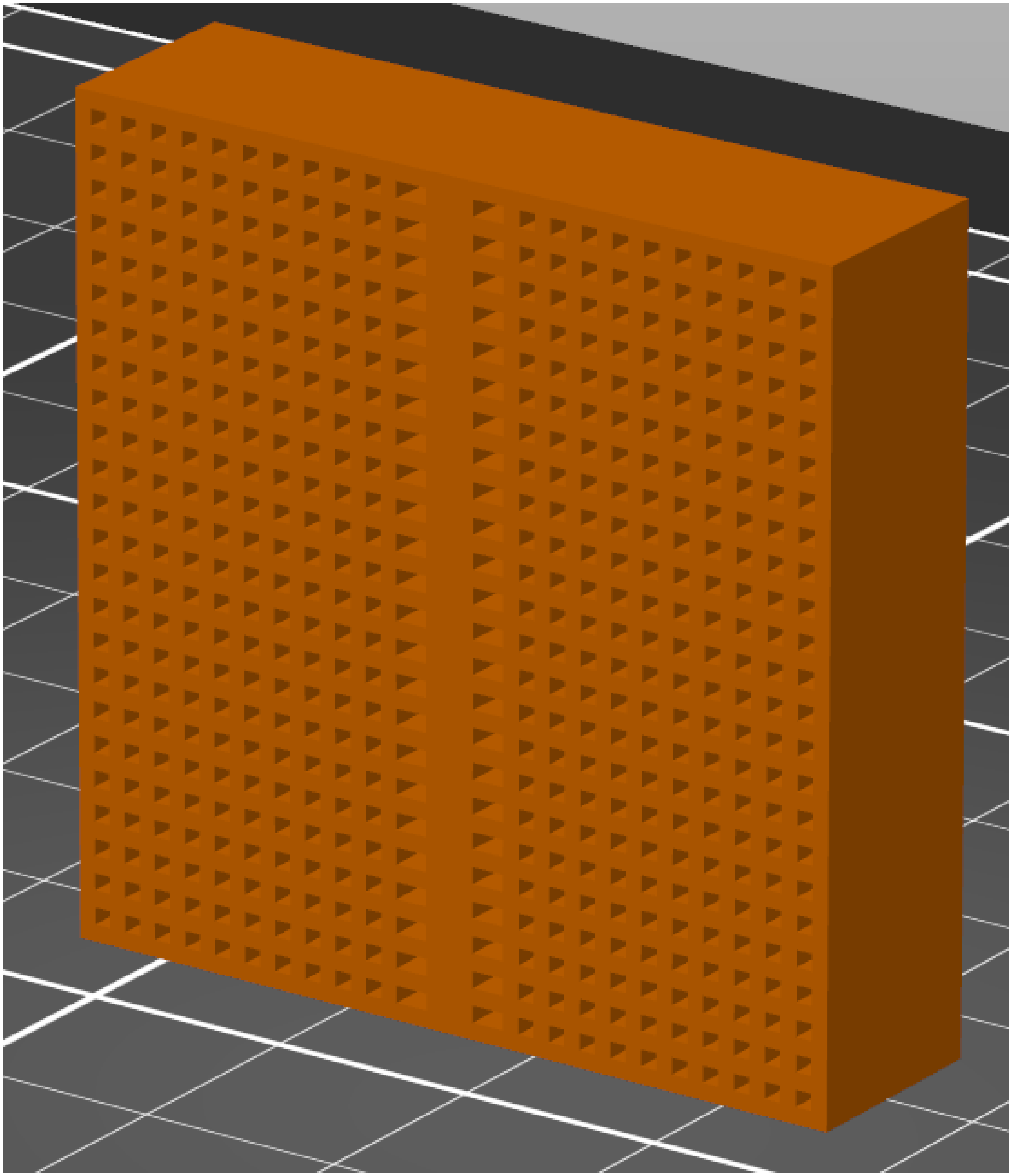

Figure 6-5: CAD model of composite design in PrusaSlicer

Pauses are added just before the top layer of the 0.8 mm square holes, as seen in Figure 6-6, at which point the coated K13D2U fibers are then carefully added by hand before resuming the print. This process is repeated for every layer where coated fibers are to be embedded into the composite.

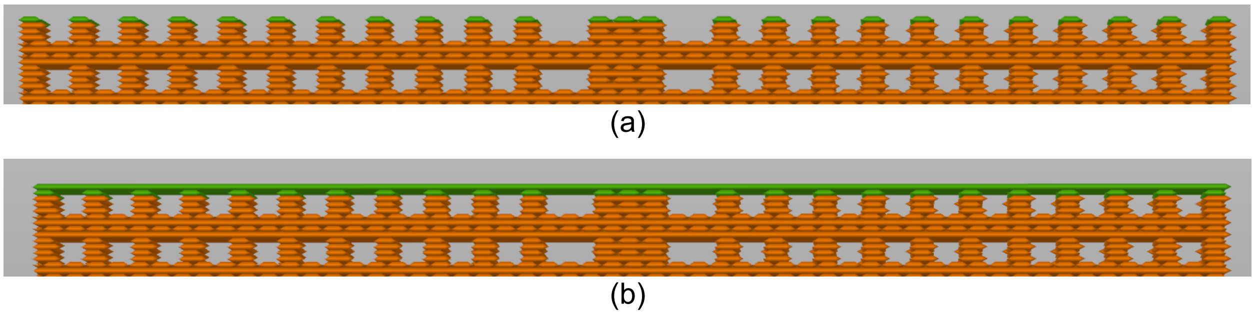

Figure 6-6: (a) Layer at which a pause is added in the print and (b) layer after coated fibers are added to the composite

Three samples were printed at an approximate fiber volume fraction of 0.71%, 2.85%, and 6.42%. The fiber volume fraction is approximated by calculating the fraction of the total fiber cross-sectional area over the total cross-sectional area of the composite.

$$v_f \approx A_f = \frac{A_{fiber}}{A_{total}} \qquad \text{Equation 6-2}$$

Measuring the precise fiber volume fraction of the composite is a bit complex since the exact volume of the voids, PLA and fibers are required for the equation:

$$v_f = \frac{V_f}{V_f + V_m + V_v} \qquad \text{Equation 6-3}$$

where V_f is the fiber volume, V_m is the matrix volume and V_v is the void volume. However, the difference between the precise and approximate calculations is likely to be insignificant and something to be tested in future research. Once the printing process was completed, the samples were carefully prepared for thermal conductivity testing. The sample surfaces were polished to create a smooth and flat finish. This step was essential to minimize contact resistance and ensure the fibers had improved thermal contact with the thermal conductivity apparatus' hot block and cold block. Lastly, two small holes were drilled into the composite for taking temperature measurements during thermal conductivity testing, without interfering with any embedded fibers.

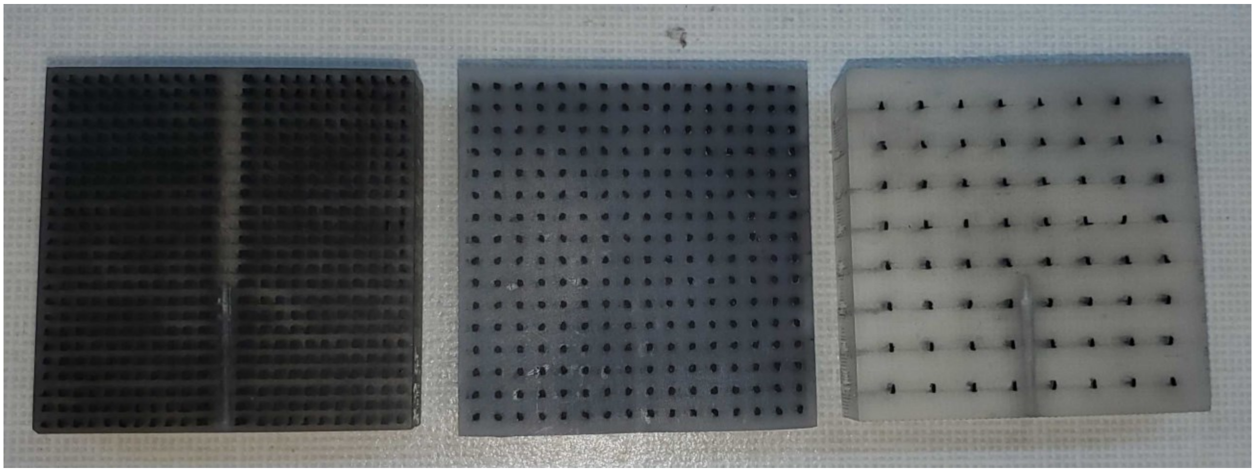

Figure 6-7: Hand-laid K13D2U composites with varying volume fractions

6.3 Results and Discussions

The thermal conductivity measurements for the three 3D-printed composites fabricated in this study are shown in Figure 6-8, alongside the results from the parallel model and Olcun's 3D-printed K13D2U composites. The parallel model predicts a linear trend between fiber volume fraction and thermal conductivity, representing the expected performance of an ideally fabricated K13D2U composite. Comparatively, Olcun's measurements for his 3D-printed K13D2U composites show a highly inconsistent trend across various volume fractions; on average, Olcun's composites exhibited a reduction in thermal conductivity exceeding 60% compared to the parallel model. Conversely, the hand-laid composites fabricated in this research demonstrate a K13D2U thermal conductivity versus volume fraction trend that is linear and, on average, shows a 30% lower thermal conductivity than the parallel model. While a 30% reduction is still significant, this figure represents thermal performance twice as high as that achieved by Olcun's samples and indicates that the 3D printing process developed by Olcun can be significantly improved. It may also be possible to further enhance the thermal conductivity of the hand-laid composite samples through optimization of the coating method. However, a major limiting factor was identified: the K13D2U tow itself tends to exhibit discontinuities at various points along its length as it is unwound during the coating process. It is currently unclear whether this issue is attributable to material quality control, handling during shipping, or another factor. Thus, regardless of process improvements, it is highly unlikely that K13D2U composites will ever achieve the expected thermal conductivity predicted by the parallel model. Further investigation of the shipped K13D2U fiber rolls is required to understand the origin of these discontinuities and their impact on composite performance.

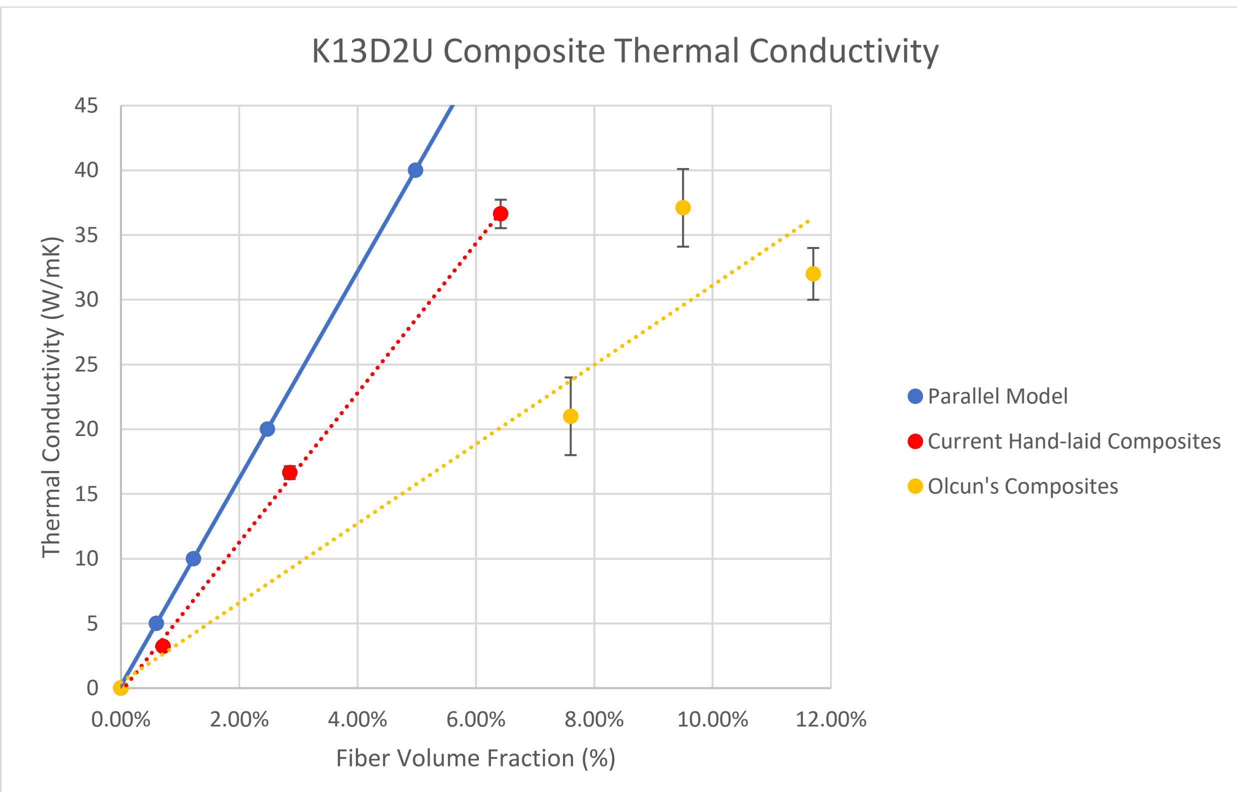

Figure 6-8: Thermal conductivity comparison between the parallel model, current hand-laid composites measurements and Olcun's 3D printed composites measurements for different volume fractions of K13D2U

While it may not be possible to achieve the expected thermal conductivities from the K13D2U composites, it is clear the K13D2U composites can still achieve a significantly high thermal conductivity. A thermal conductivity of 36.63 ± 1 W/mK was achieved at only a 6.42%

volume fraction, which is near the practical ceiling of what is achievable through the hand-laid method. This limitation is due to the sheer density of the fibers, where it becomes cumbersome and difficult, if not impossible, to manually embed more K13D2U tows in each layer without encountering issues such as PLA-to-fiber interference or user error. It is possible to push this ceiling through 3D printing, but even with automation, achieving substantially higher volume fractions may not be viable and thus may not yield significantly higher thermal conductivities. With higher fiber volume fractions, fiber breakage is likely to occur due to cramming. At these higher fiber volume fractions, it becomes crucial to use smaller printer nozzles than the standard 0.4 mm. This will allow printing thinner walls and layers to make space for additional fiber layers at the cost of longer print times. Currently, the hand-laid samples show a common linear trend in thermal conductivity with the parallel model, thus confirming the possibility of a 3D printed composite using the newly coated K13D2U fibers with a well-developed 3D printing process.

Chapter 7 Summary and Conclusions

This thesis presents CPCF as a highly favorable material for thermal management composites due to their weight to thermal conductivity ratio over commonly used metals. The challenges and discrepancies found when fabricating CPCF composites in previous research by Ibrahim and Olcun were investigated. To address the challenges and discrepancies faced in CPCF composite fabrication, several research objectives were proposed: accurately characterizing fiber geometry, developing improved thermal characterization techniques, mitigating fiber breakage in the coating and printing processes, and implementing process improvements for a full-scale 3D-printed CPCF composite.

Accurate fiber geometry characterization is essential for precise thermal conductivity measurements, as most analytical models rely on the fiber cross-sectional area. Given the micro-scale nature of the fibers, accurate measurement of cross-sectional area is a complex process, particularly because the material consists of a tow containing approximately 2,000 individual filaments. Initial characterization attempts using optical microscopy and (SEM) to count fibers via ImageJ revealed significant inconsistencies, with the fiber count varying by more than one hundred filaments between two different rolls of K13D2U. Similarly, the fiber diameter exhibited a large variance and required extensive image processing in ImageJ to determine a statistical average. While the results from these two imaging methods were close to the specifications provided by Mitsubishi Chemicals for K13D2U, they were ultimately insufficient as standalone measurements due to large uncertainties. Pycnometry was then used to measure CPCF tow density, which, in conjunction with mass measurements from a high-sensitivity scale, allowed for the calculation of the cross-sectional area based on the density equation. This method was found to be highly consistent, accurate, and efficient for measuring multiple tows from each K13D2U roll while maintaining uncertainties below 1%. Additionally, subsequent cross-sectional area measurements of the CPCF tow showed negligible variance within the same tow and between different rolls of K13D2U.

With an accurate methodology established for the measurement of CPCF tow cross-sectional area, a high-precision apparatus was required to characterize its thermal conductivity. Various transient methodologies were reviewed, including the transient hot-wire, TLS, TPS or hot disk, LFA, and 3ω methods. However, these techniques are typically applied to individual fiber filaments rather than tows and often require complex, costly instrumentation to achieve accurate results. Consequently, the steady-state guarded hot plate method was reviewed and determined to be best suited for CPCF tows, particularly since Olcun's apparatus utilized a similar approach. Olcun's design however, contained several limitations that contributed to significant uncertainties in thermal conductivity measurements. Specifically, the glass bell jar presented a large view factor between the CPCF tow and the external surroundings; since measurements were conducted within a vacuum, radiative losses were magnified and should have been considered. Additionally, the primary heater was unguarded and exposed to both convective and radiative losses. While Olcun presented a heat loss calibration for convective losses, radiative heat loss was assumed to be negligible, and the precise methodology for these corrections were unclear. The newly developed apparatus addresses these deficiencies by employing a guarded hot plate configuration, in which the primary heater is enclosed within a secondary guard heater. By matching their temperatures, the heat generated by the primary heater is forced to conduct entirely through the sample. Furthermore, a comprehensive heat loss calibration was performed alongside an implementation of radiation shielding for the sample to minimize heat loss. Finally, an uncertainty analysis was conducted to quantify the error associated with the measurements, and the apparatus was validated against known metal wires prior to characterizing the CPCF thermal conductivity. The results indicated good agreement with known metals, and the measurements had uncertainties of less than 15%. The

K13D2U measurements showed that the thermal conductivity of the tow was, on average, 778 W/mK.

With a baseline thermal conductivity established for the K13D2U tow, Chapter 5 focuses on refining the fiber coating process. Olcun's original methodology was found to be inconsistent, producing PLA coated K13D2U tows with significant diameter variations. This oversaturation of the PLA coating directly impacted the thermal conductivity measurements. The thermal resistance data illustrated in Figure 5-1 exhibited higher variance and a lower R^2 value than expected. This variance, in turn, amplified the uncertainty of the measured thermal conductivity. The newly developed coating method outlined in Chapter 5 successfully addresses the issue of PLA oversaturation, resulting in highly uniform K13D2U tows. The subsequent measurements align with the expected thermal conductivity for K13D2U while significantly reducing measurement uncertainty. Finally, K13D2U rasters printed using both Olcun's extruder setup and the newly developed extruder design were both tested. While the results indicated little difference in measured thermal conductivity between the two, Olcun's setup was unable to consistently produce rasters for testing due to a heavily worn, customized nozzle, along with other failing components. These issues led to inconsistent prints, suggesting that the initial successful measurements may have been outliers.

The final stage of this research aimed to fabricate and measure the thermal conductivity of a full-size 3D-printed K13D2U composite. However, the 3D printer requires an extensive overhaul to enable automated CPCF printing. While the hot press design was effective for producing CPCF rasters, its size interfered with full-scale printing. Furthermore, the printer requires an upgraded motherboard and a redesigned extruder-cutter assembly capable of sequential fiber deposition and cutting. Due to constraints in time and resources, a complete hardware overhaul was deemed out of scope, leading to an alternative goal. This involved manually fabricating the composite by utilizing the PrusaSlicer's "pause at layer" function. A

CAD model was designed with specific grooves, allowing the coated K13D2U tows to be hand-placed at designated layer heights during each pause during the print. Three composites with varying fiber volume fractions were produced using this method, and their thermal conductivities were measured. The results were compared against both Olcun's measurements and the theoretical parallel model. The findings indicated a substantial improvement in thermal conductivity, where the measured thermal conductivities were 30% lower than the theoretical prediction as opposed to the 60% error reported by Olcun. At a 6.42% fiber volume fraction, the composite achieved a measured thermal conductivity of 36.63 W/mK, representing the highest performance recorded to date using K13D2U fibers.

7.1 Future Work

Various advances were made in the 3D printing process of CPCF fibers, yet additional work is required to achieve a fully automated printer capable of producing CPCF composites. With the newly developed apparatus for measuring fiber thermal conductivity, it is important to test a larger sample size to better account for variability. There is also room for improvement in the current apparatus to enable easier and faster measurements, which would support higher testing throughput. Additionally, in the future the polymer sizing can be investigated for its affect on measurements by potentially melting it off.

The coating apparatus currently requires significant time and effort to produce coated tows. During the process, issues such as inconsistent pressure within the molten chamber were observed, occasionally causing PLA to overflow from the fiber entry orifice. This leads to fiber buckling and fraying, resulting in intermittent breakage and requiring cleanup and reset. An automated setup that uses controlled extrusion to feed PLA into the chamber while simultaneously pulling the fiber tow through could significantly improve consistency, reduce breakage, and increase processing speed.

Lastly, either a new 3D printer or a custom mainboard is required to enable simultaneous control of multiple extruders, which is necessary to implement a fiber feeding and cutting mechanism for fully automated CPCF printing. This would require a well-designed system capable of printing at shallow angles while maintaining precise control over filament placement. Additionally, a more efficient method for handling and loading long coated CPCF tows during printing could reduce the required workspace and enable automated reloading. Due to their brittleness, coated CPCF tows cannot be bent or spooled like conventional filaments, which presents a handling challenge. Exploring alternative CPCF materials, potentially with improved flexibility or handling characteristics, may help address this limitation, making it worthwhile to evaluate a range of different CPCFs. Experimenting with other coating materials such as nylon, TPU and TPE can also potentially address this issue, though their mechanical properties must also be considered.

References

[1] Z. He, Y. Yan, and Z. Zhang, “Thermal management and temperature uniformity enhancement of electronic devices by micro heat sinks: A review,” *Energy*, vol. 216, p. 119223, Feb. 2021, doi: 10.1016/j.energy.2020.119223.

[2] S. Anandan and V. Ramalingam, “Thermal management of electronics: A review of literature,” *Therm sci*, vol. 12, no. 2, pp. 5–26, 2008, doi: 10.2298/TSCI0802005A.

[3] G. Zilio, D. G. Borges, M. V. V. Mortean, J. L. G. Oliveira, G. B. Dutra, and K. V. Paiva, “Characterization of compact heat exchangers manufactured by laser powder bed fusion technology,” *J Braz. Soc. Mech. Sci. Eng.*, vol. 45, no. 8, p. 393, Aug. 2023, doi: 10.1007/s40430-023-04311-w.

[4] R. R. J. Sélo, S. Catchpole-Smith, I. Maskery, I. Ashcroft, and C. Tuck, “On the thermal conductivity of AlSi10Mg and lattice structures made by laser powder bed fusion,” *Additive Manufacturing*, vol. 34, p. 101214, Aug. 2020, doi: 10.1016/j.addma.2020.101214.

[5] A. Elkholy, “CHARACTERIZATION OF HEAT EXCHANGE FOR ADDITIVELY MANUFACTURED COMPONENTS,” 2021.

[6] A. J. Robinson, J. Colenbrander, T. Deaville, J. Durfee, and R. Kempers, “A wicked heat pipe fabricated using metal additive manufacturing,” *International Journal of Thermofluids*, vol. 12, p. 100117, Nov. 2021, doi: 10.1016/j.ijft.2021.100117.

[7] Y. Wang *et al.*, “Epoxy Composites with High Thermal Conductivity by Constructing Three-Dimensional Carbon Fiber/Carbon/Nickel Networks Using an Electroplating Method,” *ACS Omega*, vol. 6, no. 29, pp. 19238–19251, July 2021, doi: 10.1021/acsomega.1c02694.

[8] R. Li *et al.*, “Review on polymer composites with high thermal conductivity and low dielectric properties for electronic packaging,” *Materials Today Physics*, vol. 22, p. 100594, Jan. 2022, doi: 10.1016/j.mtphys.2021.100594.

[9] Y. Ibrahim, A. Elkholy, J. S. Schofield, G. W. Melenka, and R. Kempers, “Effective thermal conductivity of 3D-printed continuous fiber polymer composites,” *Advanced Manufacturing: Polymer & Composites Science*, vol. 6, no. 1, pp. 17–28, Jan. 2020, doi: 10.1080/20550340.2019.1710023.

[10] “Carbon Fiber Tow (Continuous fiber),” Mitsubishi Chemical Carbon Fiber & Carbon Fiber Reinforced Plastics Special Site. Accessed: Jan. 01, 2024. [Online]. Available: https://www.m-chemical.co.jp/carbon-fiber/en/product/tow/

[11] S. Olcun, “DEVELOPMENT OF CHARACTERIZATION OF 3D-PRINTED CONTINUOUS PITCH CARBON FIBER COMPOSITES,” 2022.

[12] A. K. Sharma, R. Bhandari, A. Aherwar, and R. Rimašauskienė, “Matrix materials used in composites: A comprehensive study,” *Materials Today: Proceedings*, vol. 21, pp. 1559–1562, 2020, doi: 10.1016/j.matpr.2019.11.086.

[13] Y. Yao, J. Sun, X. Zeng, R. Sun, J. Xu, and C. Wong, “Construction of 3D Skeleton for Polymer Composites Achieving a High Thermal Conductivity,” *Small*, vol. 14, no. 13, p. 1704044, Mar. 2018, doi: 10.1002/smll.201704044.

[14] A. F. Ahmed and S. V. Hoa, “Thermal insulation by heat resistant polymers for solid rocket motor insulation,” *Journal of Composite Materials*, vol. 46, no. 13, pp. 1549–1559, June 2012, doi: 10.1177/0021998311418850.

[15] V. Vahedy, “Polymer insulated high voltage cables,” *IEEE Electr. Insul. Mag.*, vol. 22, no. 3, pp. 13–18, May 2006, doi: 10.1109/MEI.2006.1639025.

[16] X. Tian *et al.*, “3D Printing of Continuous Fiber Reinforced Polymer Composites: Development, Application, and Prospective,” *Chinese Journal of Mechanical Engineering: Additive Manufacturing Frontiers*, vol. 1, no. 1, p. 100016, Mar. 2022, doi: 10.1016/j.cjmeam.2022.100016.

[17] I. A. Tsekmes, R. Kochetov, P. H. F. Morshuis, and J. J. Smit, “Thermal conductivity of polymeric composites: A review,” in *2013 IEEE International Conference on Solid Dielectrics (ICSD)*, Bologna, Italy: IEEE, June 2013, pp. 678–681. doi: 10.1109/ICSD.2013.6619698.
[18] M. R. Shaeri and R. Bonner, “ADVANCES IN LIGHTWEIGHT HEAT SINKS,” in *Proceeding of 4th Thermal and Fluids Engineering Conference*, Las Vegas, NV, USA: Begellhouse, 2019, pp. 839–842. doi: 10.1615/TFEC2019.fip.027643.
[19] C. T’Joen, Y. Park, Q. Wang, A. Sommers, X. Han, and A. Jacobi, “A review on polymer heat exchangers for HVAC&R applications,” *International Journal of Refrigeration*, vol. 32, no. 5, pp. 763–779, Aug. 2009, doi: 10.1016/j.ijrefrig.2008.11.008.
[20] T. R. Vijaybabu *et al.*, “High Thermal Conductivity Polymer Composites Fabrication through Conventional and 3D Printing Processes: State-of-the-Art and Future Trends,” *Macro Materials & Eng*, vol. 308, no. 7, p. 2300001, July 2023, doi: 10.1002/mame.202300001.
[21] S. Park and M.-K. Seo, *Interface science and composites*, 1st ed. in Interface science and technology, no. v. 18. Amsterdam : Boston: Elsevier ; Academic Press, 2011.
[22] S. Choi and J. Kim, “Thermal conductivity of epoxy composites with a binary-particle system of aluminum oxide and aluminum nitride fillers,” *Composites Part B: Engineering*, vol. 51, pp. 140–147, Aug. 2013, doi: 10.1016/j.compositesb.2013.03.002.
[23] C. Shemelya *et al.*, “Anisotropy of thermal conductivity in 3D printed polymer matrix composites for space based cube satellites,” *Additive Manufacturing*, vol. 16, pp. 186–196, Aug. 2017, doi: 10.1016/j.addma.2017.05.012.
[24] A. Boudenne, L. Ibos, M. Fois, J. C. Majesté, and E. Géhin, “Electrical and thermal behavior of polypropylene filled with copper particles,” *Composites Part A: Applied Science and Manufacturing*, vol. 36, no. 11, pp. 1545–1554, Nov. 2005, doi: 10.1016/j.compositesa.2005.02.005.
[25] Y.-X. Fu, Z.-X. He, D.-C. Mo, and S.-S. Lu, “Thermal conductivity enhancement with different fillers for epoxy resin adhesives,” *Applied Thermal Engineering*, vol. 66, no. 1–2, pp. 493–498, May 2014, doi: 10.1016/j.applthermaleng.2014.02.044.
[26] X. Wang, Q. Jiang, W. Xu, W. Cai, Y. Inoue, and Y. Zhu, “Effect of carbon nanotube length on thermal, electrical and mechanical properties of CNT/bismaleimide composites,” *Carbon*, vol. 53, pp. 145–152, Mar. 2013, doi: 10.1016/j.carbon.2012.10.041.
[27] C. Fu *et al.*, “Improving thermal conductivity of polymer composites by reducing interfacial thermal resistance between boron nitride nanotubes,” *Composites Science and Technology*, vol. 165, pp. 322–330, Sept. 2018, doi: 10.1016/j.compscitech.2018.07.010.
[28] M.-S. Jeng, R. Yang, D. Song, and G. Chen, “Modeling the Thermal Conductivity and Phonon Transport in Nanoparticle Composites Using Monte Carlo Simulation,” *Journal of Heat Transfer*, vol. 130, no. 4, p. 042410, Apr. 2008, doi: 10.1115/1.2818765.
[29] H. Chen *et al.*, “Thermal conductivity of polymer-based composites: Fundamentals and applications,” *Progress in Polymer Science*, vol. 59, pp. 41–85, Aug. 2016, doi: 10.1016/j.progpolymsci.2016.03.001.
[30] A. Abdulhameed, “Carbon Nanotube Alignment Methods,” in *Carbon Nanotubes - Recent Advances, New Perspectives and Potential Applications*, M. Muzibur Rahman, A. Mohammed Asiri, and M. Asaduzzaman Chowdhury, Eds., IntechOpen, 2023. doi: 10.5772/intechopen.108236.
[31] C. Ye *et al.*, “Microstructure of high thermal conductivity mesophase pitch-based carbon fibers,” *New Carbon Materials*, vol. 36, no. 5, pp. 980–985, Oct. 2021, doi: 10.1016/S1872-5805(21)60050-1.
[32] B.-K. Choi, W.-K. Choi, C.-S. Kang, H. Lee, J.-K. Ko, and M.-K. Seo, “Apparent thermal conductivity of PAN-based carbon fibre tow based on infrared thermography measurements,” *Materials Science and Engineering: B*, vol. 289, p. 116188, Mar. 2023, doi: 10.1016/j.mseb.2022.116188.

[33] D. Jang and S. Lee, “Correlating thermal conductivity of carbon fibers with mechanical and structural properties,” *Journal of Industrial and Engineering Chemistry*, vol. 89, pp. 115–118, Sept. 2020, doi: 10.1016/j.jiec.2020.06.026.
[34] V. Dhand, G. Mittal, K. Y. Rhee, S.-J. Park, and D. Hui, “A short review on basalt fiber reinforced polymer composites,” *Composites Part B: Engineering*, vol. 73, pp. 166–180, May 2015, doi: 10.1016/j.compositesb.2014.12.011.
[35] Y. Ibrahim, G. W. Melenka, and R. Kempers, “Fabrication and tensile testing of 3D printed continuous wire polymer composites,” *RPJ*, vol. 24, no. 7, pp. 1131–1141, Oct. 2018, doi: 10.1108/RPJ-11-2017-0222.
[36] P. M. Gore and B. Kandasubramanian, “Functionalized Aramid Fibers and Composites for Protective Applications: A Review,” *Ind. Eng. Chem. Res.*, vol. 57, no. 49, pp. 16537–16563, Dec. 2018, doi: 10.1021/acs.iecr.8b04903.
[37] T. Sathishkumar, S. Satheeshkumar, and J. Naveen, “Glass fiber-reinforced polymer composites – a review,” *Journal of Reinforced Plastics and Composites*, vol. 33, no. 13, pp. 1258–1275, July 2014, doi: 10.1177/0731684414530790.
[38] S. D. Nath and S. Nilufar, “An Overview of Additive Manufacturing of Polymers and Associated Composites,” *Polymers*, vol. 12, no. 11, p. 2719, Nov. 2020, doi: 10.3390/polym12112719.
[39] J. Griffey, *3-D printers for libraries*. Chicago, IL: ALA TechSource, 2014.
[40] M. A. Arie, D. M. Hymas, F. Singer, A. H. Shooshtari, and M. Ohadi, “An additively manufactured novel polymer composite heat exchanger for dry cooling applications,” *International Journal of Heat and Mass Transfer*, vol. 147, p. 118889, Feb. 2020, doi: 10.1016/j.ijheatmasstransfer.2019.118889.
[41] C. Yang, X. Tian, D. Li, Y. Cao, F. Zhao, and C. Shi, “Influence of thermal processing conditions in 3D printing on the crystallinity and mechanical properties of PEEK material,” *Journal of Materials Processing Technology*, vol. 248, pp. 1–7, Oct. 2017, doi: 10.1016/j.jmatprotec.2017.04.027.
[42] Markforged, “Desktop 3D Printer Series.” Accessed: Jan. 01, 2024. [Online]. Available: https://markforged.com/desktop-series
[43] ContinuousComposites, “CF3D® A Breakthrough in Composites.” Accessed: Jan. 01, 2024. [Online]. Available: https://www.continuouscomposites.com/technology
[44] C. Raman and P. Meneghetti, “Boron nitride finds new applications in thermoplastic compounds,” *Plastics, Additives and Compounding*, vol. 10, no. 3, pp. 26–31, May 2008, doi: 10.1016/S1464-391X(08)70092-8.
[45] H. Guo *et al.*, “Highly Thermally Conductive 3D Printed Graphene Filled Polymer Composites for Scalable Thermal Management Applications,” *ACS Nano*, vol. 15, no. 4, pp. 6917–6928, Apr. 2021, doi: 10.1021/acsnano.0c10768.
[46] R. Singh, G. Sandhu, R. Penna, and I. Farina, “Investigations for Thermal and Electrical Conductivity of ABS-Graphene Blended Prototypes,” *Materials*, vol. 10, no. 8, p. 881, July 2017, doi: 10.3390/ma10080881.
[47] Y. Ibrahim, “3D Printing of Continuous Wire Polymer Composite for Mechanical and Thermal Applications,” 2019.
[48] S. Olcun, Y. Ibrahim, C. Isaacs, M. Karam, A. Elkholy, and R. Kempers, “Thermal conductivity of 3D-printed continuous pitch carbon fiber composites,” *Additive Manufacturing Letters*, vol. 4, p. 100106, Feb. 2023, doi: 10.1016/j.addlet.2022.100106.
[49] Nippon Graphite Fiber Corporation, “High thermal conductivity.” Accessed: Jan. 01, 2024. [Online]. Available: https://www.ngfworld.com/en/fiber/high_thermal_conductivity.html
[50] K. Naito, Y. Tanaka, J. Yang, and Y. Kagawa, “Flexural Properties of PAN- and Pitch-Based Carbon Fibers,” *Journal of the American Ceramic Society*, vol. 92, no. 1, pp. 186–192, Jan. 2009, doi: 10.1111/j.1551-2916.2008.02868.x.
[51] “MKS Instruments Handbook - Semiconductor Devices and Process Technology”.

[52] R. C. Kerschbaumer *et al.*, “Comparison of steady-state and transient thermal conductivity testing methods using different industrial rubber compounds,” *Polymer Testing*, vol. 80, p. 106121, Dec. 2019, doi: 10.1016/j.polymertesting.2019.106121.
[53] A. J. Slifka, “Thermal-conductivity apparatus for steady-state, comparative measurement of ceramic coatings,” *J. Res. Natl. Inst. Stand. Technol.*, vol. 105, no. 4, p. 591, July 2000, doi: 10.6028/jres.105.050.
[54] C. Jensen, C. Xing, C. Folsom, H. Ban, and J. Phillips, “Design and Validation of a High-Temperature Comparative Thermal-Conductivity Measurement System,” *Int J Thermophys*, vol. 33, no. 2, pp. 311–329, Feb. 2012, doi: 10.1007/s10765-012-1161-9.
[55] A. Palacios, L. Cong, M. E. Navarro, Y. Ding, and C. Barreneche, “Thermal conductivity measurement techniques for characterizing thermal energy storage materials – A review,” *Renewable and Sustainable Energy Reviews*, vol. 108, pp. 32–52, July 2019, doi: 10.1016/j.rser.2019.03.020.
[56] M. Ruoho, K. Valset, T. Finstad, and I. Tittonen, “Measurement of thin film thermal conductivity using the laser flash method,” *Nanotechnology*, vol. 26, no. 19, p. 195706, May 2015, doi: 10.1088/0957-4484/26/19/195706.
[57] H. Wang and M. Sen, “Analysis of the 3-omega method for thermal conductivity measurement,” *International Journal of Heat and Mass Transfer*, vol. 52, no. 7–8, pp. 2102–2109, Mar. 2009, doi: 10.1016/j.ijheatmasstransfer.2008.10.020.
[58] X. Zhang, S. Fujiwara, and M. Fujii, “Measurements of Thermal Conductivity and Electrical Conductivity of a Single Carbon Fiber”.
[59] J. Moon *et al.*, “Note: Thermal conductivity measurement of individual poly(ether ketone)/carbon nanotube fibers using a steady-state dc thermal bridge method,” *Review of Scientific Instruments*, vol. 83, no. 1, p. 016103, Jan. 2012, doi: 10.1063/1.3676650.
[60] K. Mishra, B. Garnier, S. Le Corre, and N. Boyard, “Accurate measurement of the longitudinal thermal conductivity and volumetric heat capacity of single carbon fibers with the 3ω method,” *J Therm Anal Calorim*, vol. 139, no. 2, pp. 1037–1047, Jan. 2020, doi: 10.1007/s10973-019-08568-z.
[61] N. C. Gallego, D. D. Edie, B. Nysten, J. P. Issi, J. W. Treleaven, and G. V. Deshpande, “The thermal conductivity of ribbon-shaped carbon fibers,” *Carbon*, vol. 38, no. 7, pp. 1003–1010, 2000, doi: 10.1016/S0008-6223(99)00203-1.
[62] J. D. Craddock, J. J. Burgess, S. E. Edrington, and M. C. Weisenberger, “Method for Direct Measurement of On-Axis Carbon Fiber Thermal Diffusivity Using the Laser Flash Technique,” *Journal of Thermal Science and Engineering Applications*, vol. 9, no. 1, p. 014502, Mar. 2017, doi: 10.1115/1.4034853.
[63] *Standard Test Method for Steady-State Heat Flux Measurements and Thermal Transmission Properties by Means of the Guarded-Hot-Plate Apparatus*, ASTM C177-19, 2019. doi: 10.1520/C0177-19.
[64] A. Elkholy and R. Kempers, “An accurate steady-state approach for characterizing the thermal conductivity of Additively manufactured polymer composites,” *Case Studies in Thermal Engineering*, vol. 31, p. 101829, Mar. 2022, doi: 10.1016/j.csite.2022.101829.
[65] “Materials Thermal Properties Database,” Thermtest Instruments. Accessed: Jan. 01, 2024. [Online]. Available: https://thermtest.com/thermal-resources/materials-database
[66] K. Jousten, “Thermal outgassing,” 1999, doi: 10.5170/CERN-1999-005.111.
[67] J. G. Speight and N. A. Lange, Eds., *Lange’s handbook of chemistry*, 16t. ed., 70th anniversary ed. in McGraw-Hill standard handbooks. New York: McGraw-Hill, 2005.
[68] R. van Gils, R. Olieslagers, M. Mirsadeghi, and J. Oosterhuis, “Thermal Contact Conductance in Vacuum,” Mar. 2022.
[69] G. Liu, L. Guo, C. Liu, and Q. Wu, “Evaluation of different calibration equations for NTC thermistor applied to high-precision temperature measurement,” *Measurement*, vol. 120, pp. 21–27, May 2018, doi: 10.1016/j.measurement.2018.02.007.

[70] M. F. Modest and S. Mazumder, *Radiative heat transfer*, Fourth edition. London: Academic Press, 2022.
[71] *Guide to the Expression of Uncertainty in Measurement (GUM)*, Geneva, Switzerland., Nov. 2008.
[72] S. J. Kline, “Describing Uncertainties in Single-Sample Experiments,” vol. 75, pp. 3–8, 1953.
[73] F. A. Morrison, “Obtaining Uncertainty Measures on Slope and Intercept of a Least Squares Fit with Excel’s LINEST”.